The Dissertation Committee for Murat Ates
certifies that this is the approved version of the following dissertation:

Fuel Economy Predictions for Heavy-Duty Vehicles and Quasi-Dimensional DI Diesel Engine Numerical Modeling

Committee:

Ronald D. Matthews, Supervisor

Matthew J. Hall, Co-Supervisor

Janet L. Ellzey

Ofodike A. Ezekoye

George Biros

Charles E. Roberts Jr.

Fuel Economy Predictions for Heavy-Duty Vehicles and Quasi-Dimensional DI Diesel Engine Numerical Modeling

by

Murat Ates, B.S.M.E.; M.S.E.

Dissertation

Presented to the Faculty of the Graduate School of

The University of Texas at Austin

in Partial Fulfillment

of the Requirements

for the Degree of

Doctor of Philosophy

The University of Texas at Austin

May 2016

Dedication

This dissertation is dedicated to my family, to my love Esra, to my mentor and friend Orhan Yamanoğlu who could not see this dissertation completed, and to the founder of modern Republic of Turkey, Mustafa Kemal Atatürk.

Acknowledgements

Without the love and support of my family I would not have come this far in my educational life and made this very important step for my professional career.

I would like to express my gratitude and respect for my advisors Dr. Ron Matthews and Dr. Matthew J. Hall who gave great support to me and who listened to me carefully all the time.

Thanks to Don Lewis and Duncan Stewart of the Texas Department of Transportation for funding this project and their great personalities and support. Without your feedback and ideas this project would not be developed this much in a short amount of time.

Gracious thanks to Robert Harrison and Lisa D. Loftus-Otway from the UT Center for Transportation Research. Without your continued assistance, the project would not have been as detailed and the Fuel Economy Model software would not have been that user-friendly without your feedbacks.

And I would like to thank MJ Yan and Lu Yan of the Yan Engines for funding this projects, and HEB for supplying drivers and trucks for the coastdown tests.

Moreover, I would like to thank my colleagues in the Engines Research Group, especially Dr. Dimitrios Dardalis, for their great support and giving me a feeling of having a big resource to help me whenever I need.

I also would like to thank my dissertation committee members; Dr. Janet L. Ellzey, Dr. Ofodike A. Ezekoye, Dr. George Biros, and Dr. Charles E. Roberts Jr., for their valuable input to the development of the engine model.

Thanks to the staff of the University of Texas at Austin, Department of Mechanical Engineering being there whenever I need help. I would like to thank especially; Dena Wegner, Rosalie Foster, Jenny Kondo, Fred Rothhauser, Mark Phillips, and Lori Holloway.

I would also like to thank all of my close friends for their support.

Finally, I would like to express my gratitude for Dr. Philip Schmidt, Dr. Derek Baker, Dr. Ronald Panton, Dr. Tess J. Moon, Dr. David G. Bogard, and Dr. Thomas M. Kiehne.

Fuel Economy Predictions for Heavy-Duty Vehicles and Quasi-Dimensional DI Diesel Engine Numerical Modeling

Murat Ates, Ph.D.

The University of Texas at Austin, 2016

Supervisor: Ronald D. Matthews

Co-Supervisor: Matthew J. Hall

A research team developed the University of Texas Fuel Economy Model to estimate the fuel consumption of both light-duty and heavy-duty vehicles operated on Texas roads. One of the objectives of the model was to be as flexible as possible in order to be capable of simulating a variety of vehicles, payloads, and traffic conditions. For heavy-duty vehicles, there are no prescribed driving cycles, there are no coastdown coefficients available from the EPA, and we relied on experimental brake specific fuel consumption maps for a few heavy-duty diesel engines.

Heavy-duty vehicle drive cycles highly depend upon the vehicle load, the grade of the road, the engine size, and the traffic conditions. In order to capture real driving conditions 54 drive cycles with three different Class 8 trucks, three weight configurations, three traffic congestion levels, and two drivers are collected. Drive cycles obtained in this research include road grade and vehicle speed data with time.

Due to the lack of data from EPA for calculating the road load force for heavy-duty vehicles, coastdown tests were performed.

To generate generic fuel maps for the fuel economy model, a direct injection quasi-dimensional diesel engine model was developed based on in-cylinder images available in the literature. Sandia National Laboratory researchers obtained various images describing diesel spray evolution, spray mixing, premixed combustion, mixing controlled combustion, soot formation, and NOx formation via imaging technologies. Dec combined all of the available images to develop a conceptual diesel combustion model to describe diesel combustion from the start of injection up to the quasi-steady form of the jet. The end of injection behavior was left undescribed in this conceptual model because no clear image was available due to the chaotic behavior of diesel combustion. A conceptual end-of-injection diesel combustion behavior model was proposed to capture diesel combustion in its life span.

A full-cycle quasi-dimensional direct injection diesel engine model was developed that represents the physical models, utilizing the conceptual model developed from imaging experiments and available experiment-based spray models, of the in-cylinder processes. The compression, expansion, and gas exchange stages are modeled via zero-dimensional single zone calculations. A full cycle simulation is necessary in order to capture the initial conditions of the closed section of the cycle and predict the brake specific fuel consumption accurately.

Table of Contents

List of Tables

List of Figures

Chapter 1

Introduction

New technologies need to be developed for both gasoline and diesel internal combustion engine (ICE) equipped vehicles in order to cope with economic and environmental problems. Due to strict emissions regulations, engines need to be optimized over the entire range of engine operating conditions to deliver the best possible performance while meeting emissions standards and providing acceptable fuel efficiency. To this end, vehicle and engine simulation codes have been developed over the past 30 years, as aided by increasing computing power. Moreover, advancements in imaging technology have helped us understand combustion phenomena of ICEs in a deeper sense that enabled simulation codes based on the physics of combustion.

1.1 Research Objective

The primary objective of this research was to develop a direct injection (DI) diesel engine model based on the physics of diesel engine combustion and to use the developed model in a heavy-duty vehicle model that is capable of simulation of real world conditions (i.e., considering grade and other heavy-duty vehicle resistive forces).

1) Vehicle Modeling

The author played a role in developing the University of Texas Fuel Economy Model to estimate the fuel consumption of both light-duty and heavy-

duty vehicles operated on Texas roads, a project which was funded by the Texas Department of Transportation (Ates, 2009; Welter *et al.*, 2009; Matthews *et al.*, 2011; Ates and Matthews, 2012). One of the objectives of the model was to be as flexible as possible in order to be capable of simulating a variety of vehicles, payloads, and traffic conditions.

In addition to developing a technique to relate the engine, transmission, and differential of the light-duty vehicle to the fuel economy of the vehicle, a relatively simple model that was used for the spark ignition engines that are used in the vast majority of light-duty vehicles was developed. The University of Texas Fuel Economy model targets the vehicle speed input with time changing the transmission gear and the engine throttle position when calculating the required vehicle total resistive force provided by the engine torque after inefficient torque multiplication in both the transmission and differential. The drive cycle is a collection of data including vehicle speed and the road grade with respect to time. For light-duty vehicles, the Environmental Protection Agency's (EPA) federal fuel consumption and emissions test protocols use well known drive cycles, e.g. FTP 72/75, US06, SC03, and HWFET. The vehicle total resistive force can be calculating using coastdown coefficients for a given vehicle speed. The light-duty vehicle model relied on coastdown coefficients which are available from EPA's website (EPA, 2012) for all light-duty vehicles sold in the U.S.

For heavy-duty vehicles, there are no prescribed driving cycles, there are no coastdown coefficients available from the EPA, and we relied on experimental brake specific fuel consumption maps for a few heavy-duty diesel engines. A companion paper (Ates and Matthews, 2012) reviewed in Chapter 2, gives details of driving cycles for heavy-duty vehicles while explaining the calculation method

used for determining the coastdown coefficients, derived from measurements taken over a long stretch of roadway from heavy-duty truck coasting data and usage of these two important concepts, drive cycle and coastdown coefficients, in a detailed vehicle model.

2) Engine Modeling

The final objective of this research was to develop a numerical model of heavy-duty diesel engine performance so that the fuel consumption of the engine can be computed fairly rapidly in order to generate a fuel consumption map and then use the model-generated fuel consumption map within the UT Fuel Economy Model rather than relying on experimental maps of brake specific fuel consumption (*bsfc*). The goal of the engine model is to calculate the instantaneous fuel consumption rate based on the required engine speed and torque demand rather than relying on experimental *bsfc* maps. The engine model must be computationally fast in order to generate a *bsfc* map in a reasonable time.

1.2 Research Methodology

1) Drive cycles and Coastdown Coefficients

Heavy-duty vehicle drive cycles highly depend upon the vehicle load, the engine size, and the traffic conditions. To capture real driving conditions 54 drive cycles with three different Class 8 trucks, three weight configurations, three traffic congestion levels, and two drivers were collected. All drive cycles were taken on a 43 km (27 mile) section of Interstate 35 through downtown Austin, one of the five most congested traffic corridors in Texas.

Another important parameter that changes driver behavior for heavy-duty vehicle simulations is the grade of the road; this parameter is missing in common drive cycles (i.e. New York Bus (NYBus), Central Business District (CBD), City Suburban Cycle & Route (CSC) etc.) or sometimes artificial grade profiles are applied to these drive cycles. The heavy-duty drive cycles obtained in this research include road grade and vehicle speed data with time.

Due to the lack of data from the EPA for calculating the road load force for heavy-duty vehicles, it was necessary to perform coastdown tests. The research team used the procedure described in SAE Recommended Practices J1263 and J2263 (SAE, 1996, 2008a). Equipment requirements, necessary test conditions, and the test method are detailed in Chapter 2.

2) Diesel Engine Model

There are several ways of simulating the internal combustion engine depending upon requirements and run-time. The simplest engine modeling method is via thermodynamic (zero-dimensional) models and complexity and computer time per simulation increases from thermodynamic models to quasi-dimensional and CFD (Computational Fluid Dynamics) models.

A zero-dimensional model can estimate engine performance characteristics accurately enough if calibrated against experimental data. However, these models use a lot of empirical data that is not available for the present dissertation research. Additionally, they need re-calibration for every additional engine, which is an expensive task.

CFD models, on the other hand, rely on more physical equations and can produce very accurate simulations of engine performance in addition to emissions

estimates. Due to advancements in computing power, it is possible to run an engine simulation in 2-3 days for simplified single cylinder cases for just one operating condition. Of course, this is a very long run-time and if we are looking for a *bsfc* map of the engine this task can easily take months.

Therefore, quasi-dimensional engine models are the preferred choice for the present purpose of combination with a vehicle fuel economy model. Quasi-dimensional models are useful for estimating engine performance with less computational time than CFD models and they are better suited for engine optimization and *bsfc* map generation. Zonal engine modeling has a history of over half a century (e.g., the single-zone analysis of heat release studied by Austen and Lyn (1962), and the two-zone combustion model developed by Whitehouse and Sareen (1974)), and a broad range of such models can be found in the literature e.g., (Chiu, Shahed and Lyn, 1976; Hiroyasu and Kadota, 1976; Im and Huh, 2000; Jung and Assanis, 2001; Asay, 2003; Zhou, Zhou and Clelland, 2006; Maiboom *et al.*, 2009; Perini and Mattarelli, 2011; Xue and Caton, 2012).

Details of the developed quasi-dimensional heavy-duty direct injection diesel engine model are discussed in Chapter 3.

Chapter 2

Coastdown Coefficient Analysis of Heavy-Duty Vehicles and Application to the Examination of the Effects of Grade and Other Parameters on Fuel Consumption[1]

To perform coastdown tests on heavy-duty trucks, both long acceleration and coasting distances are required. It is very difficult to find long flat stretches of road to conduct these tests; for a Class 8 truck loaded to 80,000 lb, about 7 miles of road is needed to complete the coastdown tests. In the present study, a method for obtaining coastdown coefficients from data taken on a road of variable grade is presented. To this end, a computer code was written to provide a fast solution for the coastdown coefficients. Class 7 and Class 8 trucks were tested with three different weight configurations: empty, "cubed-out" (fully loaded but with a payload of moderate density), and "weighed-out" (loaded to the maximum permissible weight). To validate the method used to extract coastdown coefficients for tests on a roadway with variable grade, tests were also performed using a 2008 Ford F-150 light-duty pickup for which the present coastdown coefficients were compared to those available from the United States Environmental Protection Agency.

---

[1] Ates, M. and Matthews, R. D. (2012) *Coastdown Coefficient Analysis of Heavy-Duty Vehicles and Application to the Examination of the Effects of Grade and Other Parameters on Fuel Consumption*. SAE Technical Paper 2012-01-2051. doi: 10.4271/2012-01-2051.

The author collected drive cycles for the heavy-duty vehicles and developed a method for determining the coastdown coefficients, derived from measurements taken over a long stretch of roadway from heavy-duty truck coasting data.

Additionally, the effect of the coastdown coefficients on the fuel consumption of Class 7 and Class 8 trucks is discussed, where the coastdown coefficients were among the input parameters to the University of Texas Fuel Economy Model. This vehicle simulation software was developed for the Texas Department of Transportation to estimate the fuel consumption of both light-duty and heavy-duty vehicles.

2.1 Introduction

The research team was tasked by the Texas Department of Transportation (TxDOT) with developing a model that can be used to predict the fuel economy of any vehicle that travels the roadways in Texas (Welter *et al.*, 2009; Matthews *et al.*, 2011). While this is a relatively straightforward assignment for light-duty vehicles, the lack of coastdown coefficients for heavy-duty vehicles is an obstacle to development and/or use of such models for the heavy-duty vehicle application. Therefore, we found it necessary to perform the experiments that would allow us to generate the required heavy-duty truck coastdown coefficients (Ates, 2009).

The forces that resist the longitudinal motion of a vehicle are reviewed in the next subsection (Matthews, 2007; Ates, 2009). Coastdown coefficients for heavy-duty trucks are discussed in the final subsection of this Introduction.

2.1.1 Total Resistive Force

Federal test protocols require the use of chassis dynamometers for fuel economy and emissions testing, at least for light-duty vehicles (Federal Register, 2014). These dynamometers must simulate both the dynamic and steady state

loads on the vehicle drivetrain for such tests to provide an accurate representation of on-road behavior.

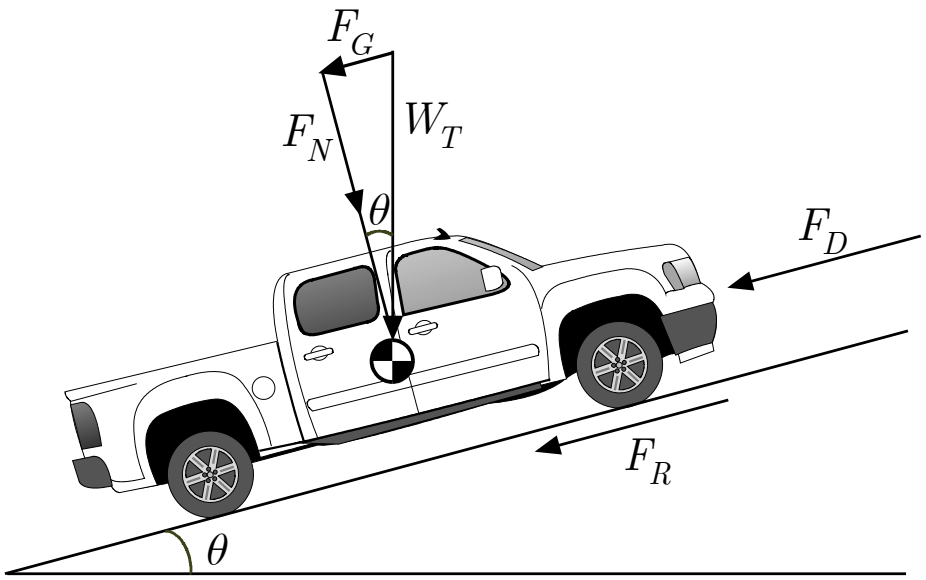

Figure 2.1 Forces acting on a vehicle driving at steady speed.

Figure 2.1 is an illustration of the forces resisting the movement of a vehicle driving on a road at a steady speed. The total resistive force, F_{res}, is the result of various individual forces that are additive. These forces are the aerodynamic drag force F_D, the rolling resistance force F_R, and the force imposed by a grade F_G:

$$F_{res} = F_D + F_R + F_G \tag{2.1}$$

These forces are illustrated in Figure 2.1, which also shows the force imposed by the "loaded" (total) weight of the vehicle W_T, which acts toward the center of the earth, and the force that is acting normal to the road surface F_N for a vehicle that is climbing a grade of angle θ.

The aerodynamic drag force is due to the resistance of the air to the movement of the vehicle. If S is the speed of the vehicle and the wind is blowing at total velocity U, with the component of the wind that is aligned with the direction of vehicle motion given symbol U_x and the component of the wind that is perpendicular to the direction of vehicle motion given symbol U_y, the aerodynamic drag force is:

$$F_D = \frac{1}{2}\rho_{air} C_D A_c \left(S \pm U_x\right)^2 + \frac{1}{2}\rho_{air} C_{Dy} A_c U_y^2 \tag{2.2}$$

where ρ_{air} is the density of the ambient air, C_D is the drag coefficient of the vehicle, A_c is the front cross-sectional area of the vehicle, and C_{Dy} is the dimensionless crosswind aerodynamic drag coefficient for the vehicle.

The rolling resistance is the frictional force acting between the tires and the road. In absence of a downforce imposed by aerodynamic devices (insignificant on all but some classes of race cars), this friction force is the product of the normal force and a friction coefficient:

$$F_R = C_R F_N = C_R W_T \cos\theta \tag{2.3}$$

where C_R is the coefficient of rolling resistance - the friction coefficient between the tires and the road surface in the direction opposed to vehicle motion.

Tire test machines roll the tire and wheel using a belt or drum, the surface of which is engineered to be similar to typical asphalt. The rolling resistance depends on both the properties of the tire and the properties of the road surface.

Additionally, both the construction and the compound of the tire affect the rolling resistance, as does the normal load on the tire. Most importantly, the coefficient of rolling resistance is dependent upon the vehicle speed. SAE Recommended Practice J1263 (1996) suggests that, unless specific information about the particular tires used is available, the following equation should be used to account for the increase in rolling resistance with increasing speed:

$$C_R = C_R^\circ \left(1 + C_R' S^2\right) \tag{2.4}$$

where C_R° is the "velocity independent coefficient of rolling resistance" (this value is the only coefficient of rolling resistance that may be available, if any, and is the value measured at low speed where C_R° is approximately constant) and C_R' is the "velocity coefficient of rolling resistance" (SAE J1263 (1996) suggests $C_R' = 50 \cdot 10^{-6} \Big/ mph^2 = 2.5 \cdot 10^{-4}\, s^2 \Big/ m^2$ if specific information is not available).

SAE Recommended Practice J2452 (2008b) describes the procedure for fitting tire test machine data for the rolling resistance force as a function of speed, the inflation pressure of the tires, and the normal load (Kelly, 2002):

$$F_R = C_R W_T = \left[\sum \left\{ P^\alpha \frac{F_Z^\beta}{F_Z} \left(C_1 + C_2 S + C_3 S^2\right) \right\}\right] W_T \tag{2.5}$$

where P is the pneumatic pressure in the tires (MPa), S is the vehicle speed (m/s), and coefficients α, β, and $C_1 - C_3$ are tire-specific constants. For the case that all tires on the vehicle are the same (have the same fitting coefficients) and the same inflation pressure and normal load, Eqn. (2.5) simplifies to:

$$F_R = C_R W_T = \left[P^{\alpha} W_T^{\beta-1} \left(C_1 + C_2 S + C_3 S^2 \right) \right] W_T \tag{2.6}$$

Eqn. (2.6) differs from Eqn. (2.4) in that Eqn. (2.4) lacks the term that is linearly dependent upon vehicle speed.

The force imposed by a grade is the force of gravity acting against the motion of the vehicle while driving uphill (or aiding the motion of the vehicle when driving downhill). As illustrated in Figure 2.1, this force is:

$$F_G = \pm W_T \sin\theta \tag{2.7}$$

where the positive sign applies to driving uphill and the negative sign applies when driving downhill.

Combining Eqns. (2.1)-(2.7) yields a relationship for the total force opposing the motion of the vehicle:

$$\begin{aligned} F_{res} &= \frac{1}{2}\rho_{air} C_D A_c (S \pm U_x)^2 + \frac{1}{2}\rho_{air} C_{Dy} A_c U_y^2 + P^{\alpha} W_T^{\beta} \left(C_1 + C_2 S + C_3 S^2 \right)_T \pm W_T \sin\theta \\ &= \left[\frac{1}{2}\rho_{air} A_c \left(C_D U_x^2 + C_{Dy} U_y^2 \right) + P^{\alpha} W_T^{\beta} C_1 \pm W_T \sin\theta \right] + \left(\pm \rho_{air} C_D A_c U_x + P^{\alpha} W_T^{\beta} C_2 \right) S \\ &\quad + \left(\frac{1}{2}\rho_{air} C_D A_c + P^{\alpha} W_T^{\beta} C_3 \right) S^2 \end{aligned} \tag{2.8}$$

Under road load conditions (a level road with no wind), Eqn. (2.8) simplifies to:

$$F_{RL} = P^{\alpha} W_T^{\beta} C_1 + \left(P^{\alpha} W_T^{\beta} C_2 \right) S + \left(\frac{1}{2}\rho_{air} C_D A_c + P^{\alpha} W_T^{\beta} C_3 \right) S^2 \tag{2.9}$$

The road load force in Eqn. (2.9) is the resistive force at the tire-road interface on a level road with no wind under steady state cruising conditions. One can account for transient operation by incorporating an inertial force term:

$$\left(F_{RL}\right)_{transient} = m_e \frac{dS}{dt} + P^{\alpha} W_T^{\beta} C_1 + \left(P^{\alpha} W_T^{\beta} C_2\right) S + \left(\frac{1}{2}\rho_{air} C_D A_c + P^{\alpha} W_T^{\beta} C_3\right) S^2 \tag{2.10}$$

When the road load force in Eqn. (2.9) is multiplied by the vehicle speed, one obtains the "road load power": the power that must be delivered to the drive axle from the engine after inefficient torque multiplication in both the transmission and differential. This road load power is also the power that must be absorbed by the chassis dyno each second during emissions certification tests.

2.1.2 Test Protocol History Leading to Coastdown Coefficients

For the light-duty vehicle manufacturers to demonstrate compliance with emissions standards and to determine the fuel economy of each make of vehicle for calculation of their Corporate Average Fuel Economy (CAFE), the auto manufacturers must have a method for consistently setting the power absorbed by their chassis dynamometers as a function of vehicle speed.

In the 1970s and 1980s, before the web became widely used, one could order reports from the Motor Vehicle Manufacturers Association (MVMA), in existence 1972-1999, now the Alliance of Automobile Manufacturers (Wikipedia, 2012) provided the drag coefficient and the front cross-sectional area. Separate reports

could be obtained for every light-duty vehicle sold in America. The vehicle manufacturer could then obtain the coefficient of rolling resistance for the tires, inflation pressure, and normal load on each tire from tire test machine data.

Historically, the product $C_D A$ was experimentally measured in tests that were conducted in a wind tunnel that did not have a "moving ground plane". Given the front cross-sectional area of the vehicle, one could then calculate the drag coefficient from the wind tunnel data. However, due to the difference in flow under the car because of the stationary floor in the wind tunnel, and especially because the tires were not rotating and thereby inducing additional aerodynamic drag, this value for C_D was not accurate (Hackett *et al.*, 1987).

Because there was uncertainty and imprecision in the method used to adjust the power absorbed by the chassis dynamometer as a function of vehicle speed, the EPA changed the technique for adjusting the road load power. Specifically, when use of 48 inch diameter chassis rolls became required in order to prevent overheating of the tires during the US06 driving cycle, this change in chassis dyno hardware also afforded the opportunity to require use of electric dynos rather than the prior water brake dynos. In turn, the use of electric chassis dynos allowed much more precise control. Therefore, the EPA changed the technique for specifying the power absorbed as a function of vehicle speed. They now provide three vehicle-specific coefficients of the form:

$$\left(F_{RL}\right)_{transient} = m_e \frac{dS}{dt} + \left(A + B \cdot S + C \cdot S^2\right) \tag{2.11}$$

where m_e is the effective mass of the vehicle (the curb weight of the vehicle divided by the local gravitational acceleration plus the EPA-specified payload of

300 lb_f plus the masses of the rotating wheel assemblies (wheels, tires, hubs, wheel bearings, etc.)) and coefficients A, B, and C are obtained from coastdown tests of the vehicle, as performed using SAE Recommended Practice J1263 or J2263 (1996, 2008a).

These coastdown coefficients, along with the "effective test weight" $\left(ETW = m_e / g\right)$, are available from the EPA (EPA, 2012) for all light-duty vehicles sold in the U.S. This website provides two sets of coastdown coefficients: Target A, Target B, and Target C plus Set A, Set B, and Set C. The target values were obtained from the on-road coastdown tests while the Set coefficients were obtained from coastdown tests on a chassis dyno. Thus, the Target coastdown coefficients are the relevant coefficients for on-road fuel economy modeling.

For driving schedules (or driving patterns) that do not involve hard acceleration or deceleration transients, or hills, the transient road load force from Eqn. (2.11) is essentially equal to the motive force. Therefore, the coastdown coefficients that are available for all light-duty vehicles that are sold in the U.S. can be used to calculate the motive force that must be provided at the tire-road interface for the vehicle to travel at any selected speed. Then, the motive torque at the tire-road interface can be calculated. One can then work one's way back through the drivetrain, given models for the differential and transmission, to determine the torque and rotational speed required from the engine, which is the consumer of the fuel.

2.1.3 Coastdown Coefficients for Heavy-Duty Vehicles

Unlike light-duty vehicles, there are many manufacturers of heavy-duty engines that may be used in heavy-duty vehicles that are assembled by other manufacturers. For example, if one purchases a heavy-duty truck, one can choose the engine from a variety of heavy-duty engine manufacturers. Because of this, and because the same heavy-duty engine can be used in a variety of vehicles and equipment, heavy-duty engines (rather than vehicles) are subjected to emissions standards (Federal Register, 2011) as assessed with the engine mounted on an engine dyno and operated over a specified heavy-duty engine test cycle. Furthermore, fuel economy standards for heavy-duty vehicles have only been promulgated recently (Federal Register, 2011) and they require improvement in the brake specific fuel consumption of the heavy-duty engine over this same operating cycle.

Therefore, the EPA provides data that are useful for fuel economy (and emissions) tests for light-duty vehicles, but does not provide any data that is useful for calculating the fuel economy of heavy-duty trucks. Some coastdown coefficients are available for European heavy-duty vehicles from Petrushov (1997, 1998) and there is a formula used by the EPA in their Motor Vehicle Emission Simulator (MOVES) model (Nam and Giannelli, 2005). The coastdown coefficient formula developed by the EPA for MOVES was derived from Petrushov (1997) and lacks the term that accounts for the linear speed dependence in Eqn. (2.9). Table 2.1 lists the coastdown coefficient formulae used in MOVES in American Conventional units.

Table 2.1 Heavy-duty vehicle coastdown coefficients obtained from other sources.

Road Load Parameters†			
Vehicle Mass[2]	**A (lb_f)**	**B (lb_f/mph)**	**C (lb_f/mph^2)**
***m* < 7,000 lb_m**	$1.0156 \times 10^{-2} m$	0	$0.051 + 1.064 \times 10^{-6} m$
7,000 ≤ *m* < 14,000 lb_m			$0.066 + 1.064 \times 10^{-6} m$
14,000 ≤ *m* ≤ 33,000 lb_m	$8.9225 \times 10^{-3} m$	0	$0.087 + 1.202 \times 10^{-6} m$
***m* > 33,000 lb_m**	$6.7403 \times 10^{-3} m$	0	$0.1298 + 8.579 \times 10^{-7} m$
Buses	$6.5568 \times 10^{-3} m$	0	$0.1447 + 1.031 \times 10^{-6} m$

† Developed from Petrushov (1997) and used in EPA's MOVES (Motor Vehicle Emission Simulator) model (Nam and Giannelli, 2005).

2.2 Coastdown Tests on Heavy-Duty Vehicles

Due to the lack of data from the EPA for calculating the road load force for heavy-duty vehicles, it was necessary to perform coastdown tests for TxDOT Project 0-5974 (Welter *et al.*, 2009; Matthews *et al.*, 2011). The research team used the procedure described in SAE Recommended Practices J1263 and J2263 (SAE, 1996, 2008a). Coastdown tests were performed on:

1) A TxDOT Ford F-150 (a light-duty vehicle, for which the coastdown coefficients are available from the EPA, to serve as a quality assurance reference),
2) A TxDOT International truck (a DOT Class 8A truck; 30,001-60,000 lb_f GVWR) with measurements made for three cases: empty (27,785 lb_f;

[2] At sea level, mass and weight are equivalent in the American Conventional System of units.

which falls into EPA Class 7, 26,001-33,000 lb_f), weighed-out (44,700 lb_f), and "cubed-out" (36,360 lb_f)

3) A TxDOT "weigh-in-motion" calibration truck (an EPA Class 8B truck with a flatbed trailer: 60,001-80,000 lb_f GVWR) with measurements made for three cases: empty (31,910 lb_f), weighed-out (78,785 lb_f), and "cubed-out" (56,470 lb_f); where two of these weight cases fall into EPA Class 8A.
4) A Texas grocery store chain loaned three Class 8 trucks with box van trailers (Figure 2.6) for this study, with wide single low rolling resistance tires and aerodynamic devices (another EPA Class 8B truck) with measurements made for three cases: empty (28,760 lb_f), weighed-out (81,010 lb_f), and "cubed-out" (55,760 lb_f); where, again, two of these weight cases fall into EPA Class 8A. This was critically important for ensuring that the University of Texas Fuel Economy Model had current data from trucks, trailers and tires that were utilized by many of the heavy-duty fleet operators who operate over the TxDOT network.

Above, "cubed-out" refers to a payload that completely fills the trailer with boxes or crates of cargo that is not so heavy that the maximum cargo weight is achieved. That is, the intermediate weights used in the present study were not simply the average between the empty weight and the GVWR. The intermediate (cubed-out) weights used for the coastdown tests of the various heavy-duty trucks were determined from TxDOT's weigh-in-motion data (Welter *et al.*, 2009). Figure 2.2 shows weigh-in-motion weight distribution data for EPA Class 8 trucks for January of 2006.

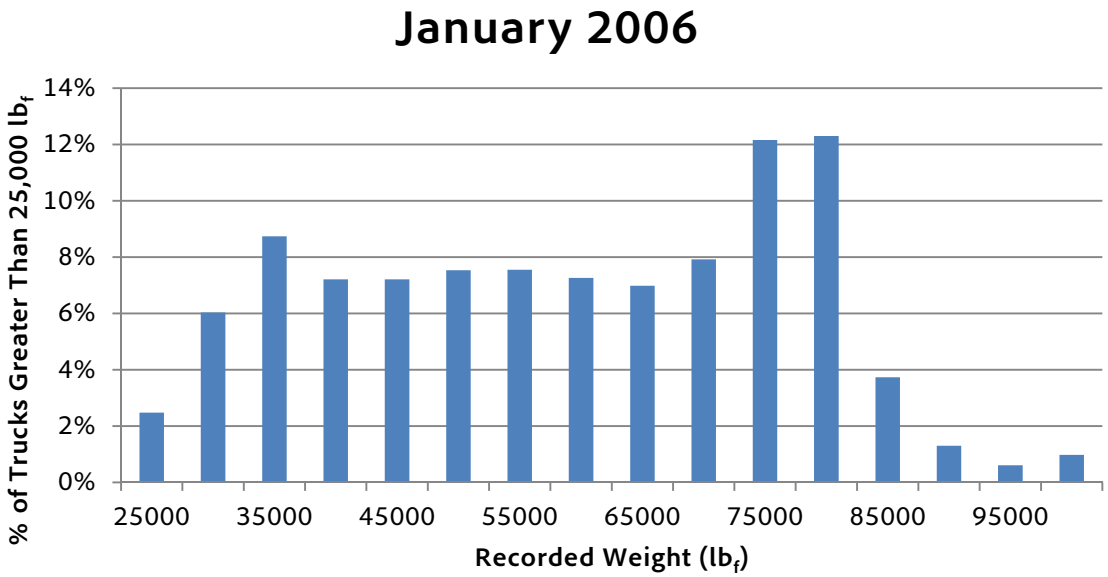

Figure 2.2 Weight-in-motion results for EPA Class 8 trucks (Welter *et al.*, 2009).

The F-150 was included in the coastdown test matrix as a quality assurance check on our coastdown test procedure. Because the F-150 is a light-duty vehicle, its coastdown coefficients are available from the EPA. We generated our own coastdown coefficients for the F-150 for comparison against EPA's values. Reasonable agreement between the two would indicate that our coastdown test results are sufficiently accurate to be useful for analyses.

Figure 2.3 is a map of the toll road that was used in our coastdown tests. TxDOT arranged for this new toll road, while in the final stages of completion, to be available for our coastdown tests. The coastdown tests ran approximately between Turnersville Road and just beyond Evelyn Road (Austin, TX) for Class 8B trucks weighting 80,000 lb_f. This provided the trucks with spaces at the end of each trip to be able to turn around and perform the coastdown test again in the opposite direction but in the same lane.

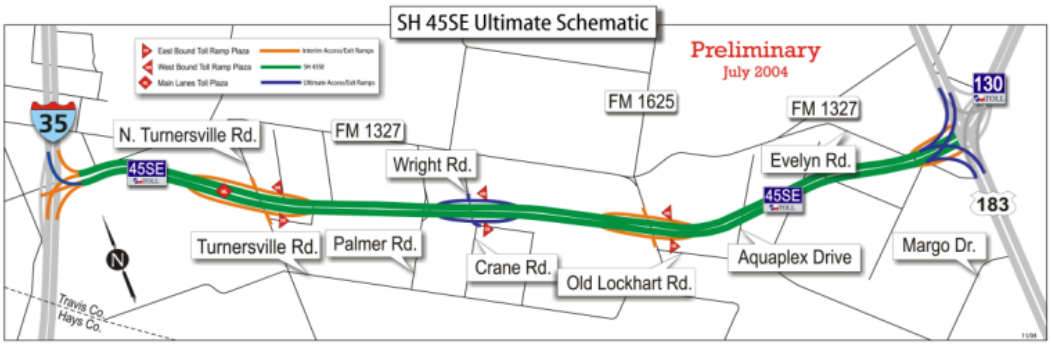

Figure 2.3 Toll road SH 45 (Austin, TX) where the coastdown tests were performed (Welter *et al.*, 2009).

During March and April 2009, 10 coastdown tests (each test consists of 5 or 6 pairs of run) were conducted for the four types of trucks specified above. Figure 2.4 shows the weigh-in-motion truck, which has a series of concrete blocks that can be taken off to reduce the weight on this truck. Figure 2.5 shows how these blocks are tied to the flatbed trailer.

Figure 2.4 TxDOT's weigh-in-motion truck with flatbed trailer viewed from the front.

Figure 2.5 TxDOT's weigh-in-motion flatbed trailer viewed from the side.

Figure 2.6 Test activity using a Class 8 truck with a box van trailer.

2.2.1 Equipment

First, the researchers set up a Honeywell TE923W weather station that included an anemometer which was attached to a standing pole at approximately 4.5 feet high (Honeywell, 2012). The weather station was used to measure wind speed, wind direction, air temperature, ambient pressure, and relative humidity

during each test. Our research team kept a tabulation (wind speed and direction was taken every minute) on these five metrics throughout the duration of the coastdown tests.

TxDOT supplied Haenni WL 101 wheel load portable scales that were used to measure the weight on each axle of every truck before each coastdown test run (Haenni Scales, 2012).

We recorded data from the vehicle's on-board computer using an Antx Messenger CAN/Bus data logger (Antx, 2012) and a GlobalSat DG-100 GPS data logger (USGlobalSat, 2012). These measurements included: vehicle speed, engine rpm, and fuel flow rate with time and GPS elevation and location. The time recording interval was 1 second. Vehicle speed recorded with the GPS data logger was used in the analysis instead of engine control unit (ECU) vehicle speed data since GPS speed data has higher accuracy (±0.1 m/s) and resolution compared to ECU vehicle speed.

2.2.2 Test Method

SAE Recommended Practices J1263 and J2263 describe the coastdown procedure in detail (1996, 2008a). Therefore, this procedure will not be repeated in this dissertation. Simply, the trucks would start at a point on the route, accelerate to 65 mph, shift the transmission into neutral, and then coast to a standing stop for each coastdown test. This would then be repeated in the reverse direction in the same lane to obtain matched pairs to minimize wind and grade effects imposed on the recorded data (Yasin, 1978). An example of the coasting data for a Class 8 truck with box van trailer in both test directions is shown in

Figure 2.7. The different coasting trend in each direction is due mostly to the slight grade.

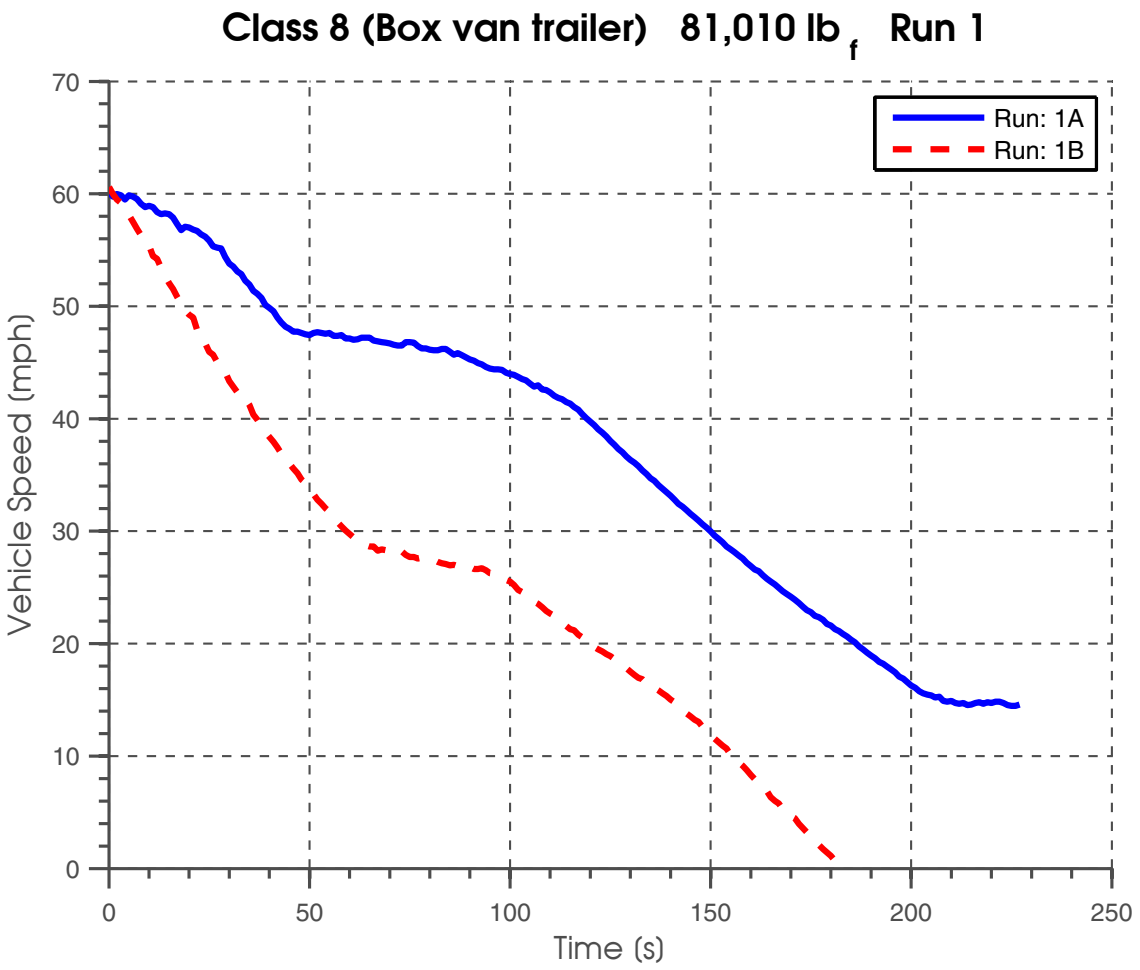

Figure 2.7 An example of coasting data in both directions for a Class 8 truck with box van trailer.

SAE Recommended Practices J1263 and J2263 (1996, 2008a) specify a maximum grade of 0.5% whereas the maximum grade on the portion of SH 45 that was used for the coastdown tests was 0.9%. Also, SAE Recommended Practices J1263 and J2263 (1996, 2008a) specify a maximum wind gust of <10 mph, but the wind speed was higher than 10 mph for some of the tests. For cases when the

wind speed was more than 10 mph, the vehicle sometimes continued to coast at lower speeds due to the combined effects of a downhill grade and a tailwind. For these conditions data below a vehicle speed of 15 mph were excluded. Moreover, data for vehicle speeds higher than 60 mph were not used to eliminate the transient due to shifting into neutral around 65 mph.

2.3 Calculation Method

Because seven miles of roadway were required for these heavy-duty truck coastdown tests, it was not possible to find the necessary stretch of road over which the grade was less than 0.5%. To compensate for this, the method I used to analyze the coastdown data was based on determining the road profile accurately. This is necessary since the grade at each point along the road should be known to compensate for the grade effect in the coastdown calculations. GPS vehicle speed data (V_{GPS}) as a function of time (t) was supplied to the coastdown coefficient calculation algorithm in addition to the effective mass (m_e) and the starting point (x_0) where coasting began. This coastdown coefficient program was solved using the High Performance Computing facility at the University of Texas.

The solution for the coastdown coefficients depends on the initial condition due to the variable grade involved in the process. Therefore, to identify the best initial condition possible, a set of ABC combinations was used as an initial guess to solve for the set that yielded the minimum error between the experimental data and the predicted coasting data based on the initial speed of the coastdown data. The ABC Matrix was made large enough to have solutions not near the limits of the ABC Matrix. An illustration of the calculation method is shown in Figure 2.8.

Acceleration/deceleration is calculated based on initial speed, V_0, at $t = 0$ as shown in Eqn. (2.12) by using the supplied coastdown coefficients A, B, and C from the ABC Matrix. The position of the vehicle was used to calculate the instantaneous grade at that position and then the force imposed by the grade was calculated as in Eqn. (2.7). The calculated acceleration (dV_0/dt) is then used to find the speed at the next time step, as shown in Eqn. (2.13). V_i and V_{i+1} are vehicle speeds at time step t_i and t_{i+1} respectively. Δt (0.1 seconds was used in this analysis) is the time step used in calculation of the new coasting data based on the supplied *ABC* Matrix.

$$\frac{dV_i}{dt} = -\frac{\left(A + BV_i + CV_i^2 \pm W_T \sin\theta\right)}{m_e} \tag{2.12}$$

$$V_{i+1} = V_i + \frac{dV_i}{dt}\Delta t \tag{2.13}$$

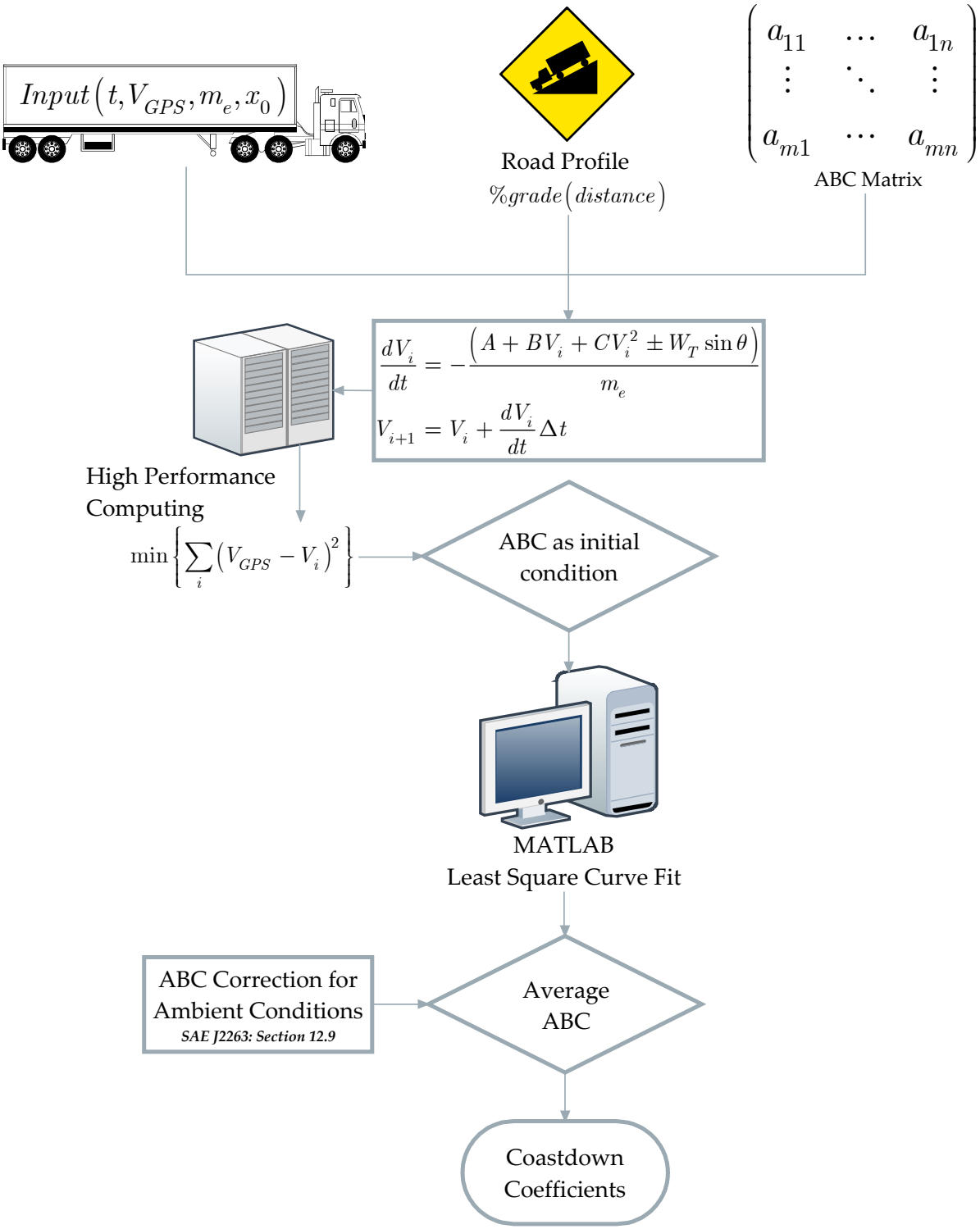

Figure 2.8 Illustration of the coastdown coefficient calculation method.

The difference between the experimental speed data and the calculated speed data from the ABC combination is squared and added as shown in Eqn. (2.14). The ABC combination that yields the minimum "error" as shown in the following equation was assumed as the initial condition for the least squares curve fit.

$$\min\left\{\sum_i \left(V_{GPS} - V_i\right)^2\right\} \tag{2.14}$$

For the Class 8 truck with the box van trailer weighing 80,010 lb_f, the range of the ABC Matrix is shown in Table 2.2 along with the matrix size and average R^2 for all of the tests with the best ABC combinations obtained. For this truck, the best ABC combination for Test 1A is shown in Figure 2.9 along with the experimental data obtained via GPS.

Table 2.2 A Sample *ABC* Combination for a Class 8 truck with box van trailer weighing 81,010 lb_f.

***A* Range [min:increment:max]**	200:1:750
***B* Range [min:increment:max]**	-15:0.1:20
***C* Range [min:increment:max]**	0.01:0.01:0.50
# of Elements in Matrix	9,670,050
Avg. R^2	0.9991

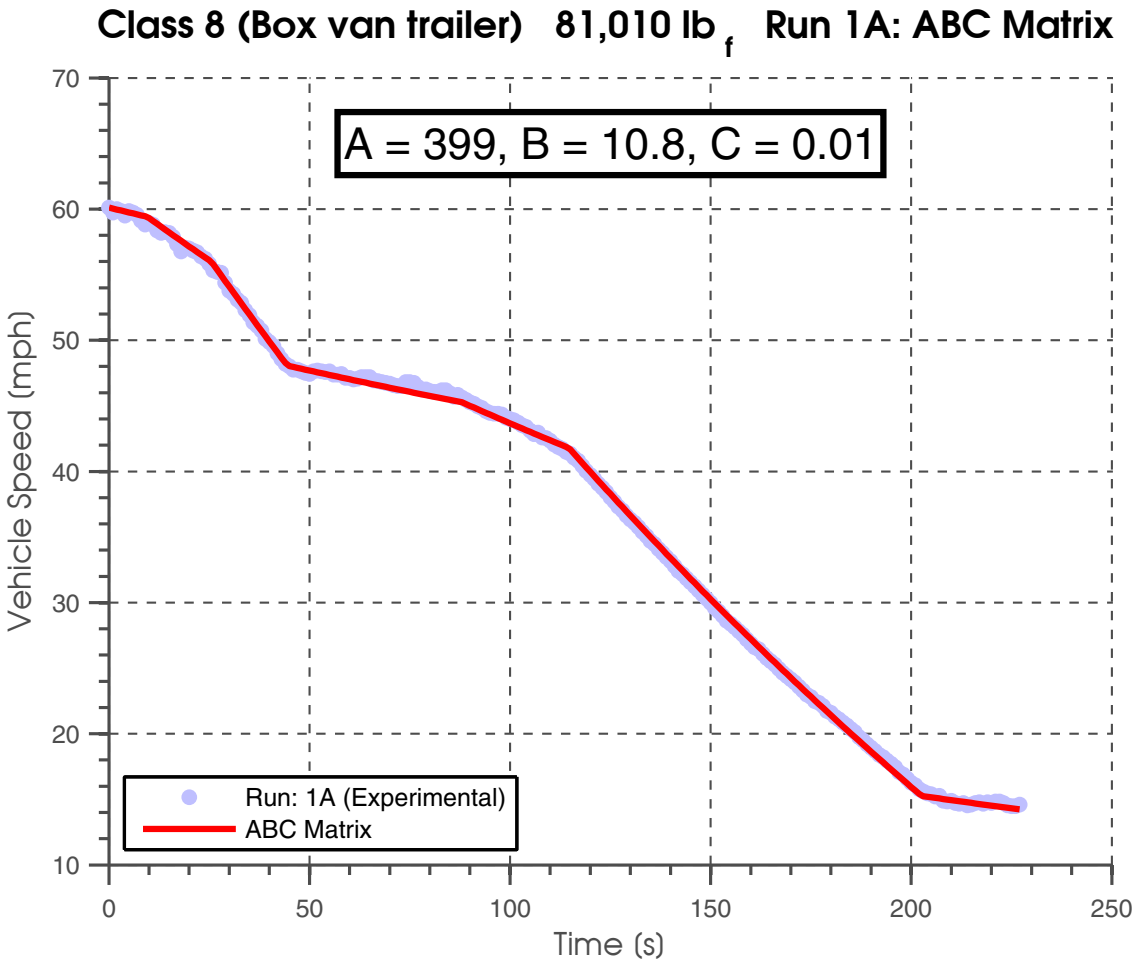

Figure 2.9 Best ABC combination for coastdown Test 1A of a Class 8 truck with box van trailer weighing 81,010 lb_f.

The least squares curve fit method was applied to fine tune the best *ABC* combination for each test. MATLAB's least squares curve fit method is capable of solving nonlinear data-fitting problems (MathWorks, 2012). An example of a least squares curve fit is shown in Figure 2.10 along with the coastdown coefficients.

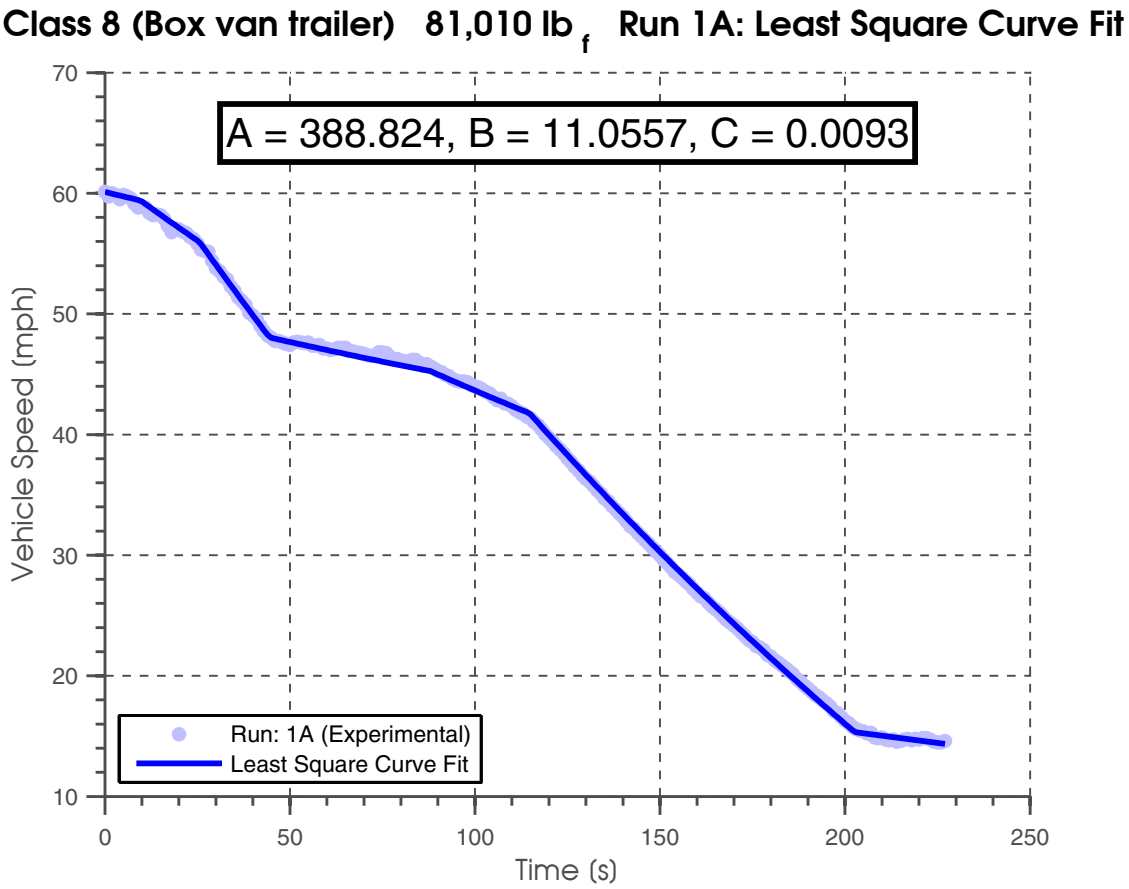

Figure 2.10 Least-squares curve fit for Test 1A of a Class 8 truck with box van trailer weighing 81,010 lb_f. The *A*, *B*, *C* combination shown in Figure 2.9 was used as an initial condition.

Coastdown coefficients A, B, and C were averaged over both directions of coasting for each test. Then, the coefficients obtained were compared with each other by drawing road load forces. Any curve not following the general trend was eliminated and the remaining test results averaged and corrected for ambient conditions as specified in SAE Recommended Practices J1263 and J2263 (1996, 2008a).

2.4 Results and Discussion

The road load force for the 2008 Ford F-150 calculated using the present coastdown coefficients from our experiments is compared with the road load force calculated using the EPA's coastdown coefficients for this vehicle in Figure 2.11. Because the calculated road load force curve using the coastdown coefficients from the present experiments is in good agreement with that using EPA's coastdown coefficients, the present method for removing the grade effect from coastdown tests provide confidence that this method of accounting for the effects of grade should also be useful for the heavy-duty truck coastdown tests. More precise agreement over the range from 10-80 mph was not expected because the TxDOT F-150 was 500 lb_f heavier than that tested by EPA due to propane tanks on the TxDOT F-150 and because the TxDOT vehicle had a light bar on the roof.

Table 2.3 summarizes the coastdown coefficients obtained for the vehicles tested. Figure 2.12, Figure 2.13, and Figure 2.14 show road load forces for 3 weight configurations for the Class 7/8A truck (dependent upon the weight of the payload), the Class 8B truck with flatbed trailer, and the Class 8B truck with box van trailer, respectively. Again, the Class 8B trucks can be categorized as EPA Class 8A trucks, depending upon the weight of the payload.

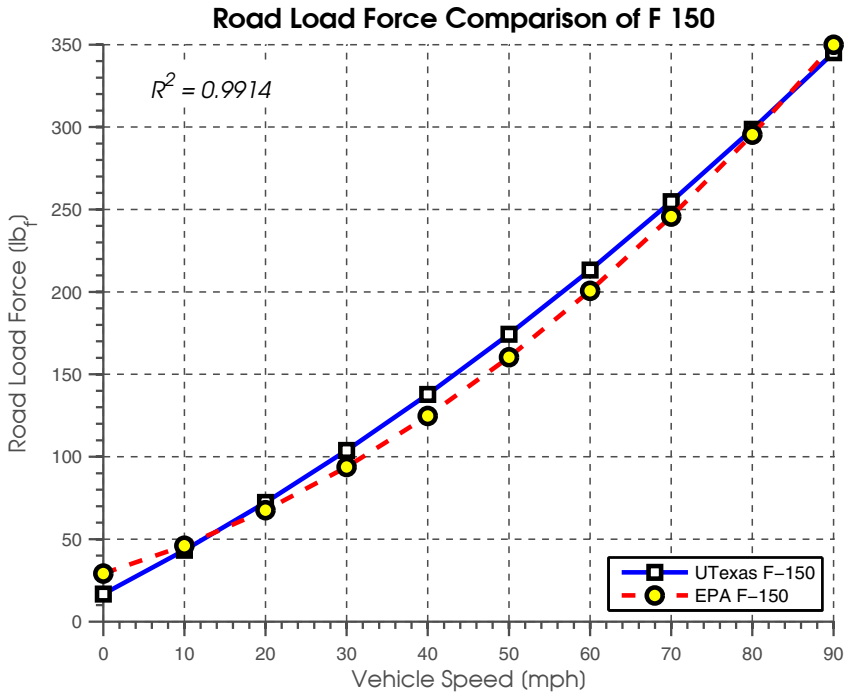

Figure 2.11 Comparison of the road load force from the present coastdown coefficients with those using EPA's coastdown coefficients for a 2008 Ford F-150.

Table 2.3 Coastdown coefficient results.

	A	*B*	*C*
F-150 – 5,890 lb_f	16.7245	2.5320	0.0124
Class 7 – 27,785 lb_f	154.5661	9.5467	0.0292
Class 7 – 36,300 lb_f	190.5042	9.2310	0.0778
Class 7 – 44,700 lb_f	243.3406	10.4669	0.0494
Class 8 flatbed – 31,910 lb_f	203.6913	2.8876	0.1819
Class 8 flatbed – 56,470 lb_f	297.0016	5.4343	0.1203
Class 8 flatbed – 78,785 lb_f	357.5108	6.8864	0.1341
Class 8 box van – 28,760 lb_f	130.5263	5.5472	0.1706
Class 8 box van – 55,760 lb_f	321.6260	9.3130	0.0617
Class 8 box van – 81,010 lb_f	446.3469	7.7606	0.1478

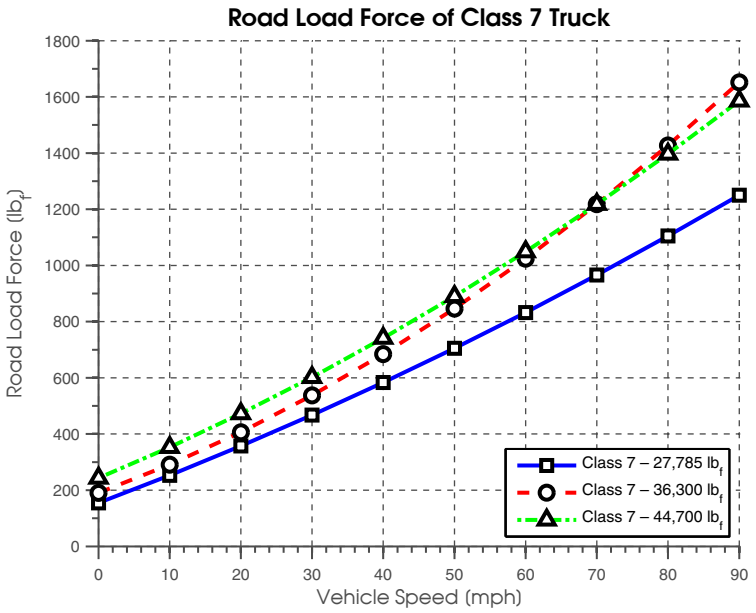

Figure 2.12 Road load force curves obtained from the present coastdown coefficients for an EPA Class 7/8A truck with 3 weight configurations.

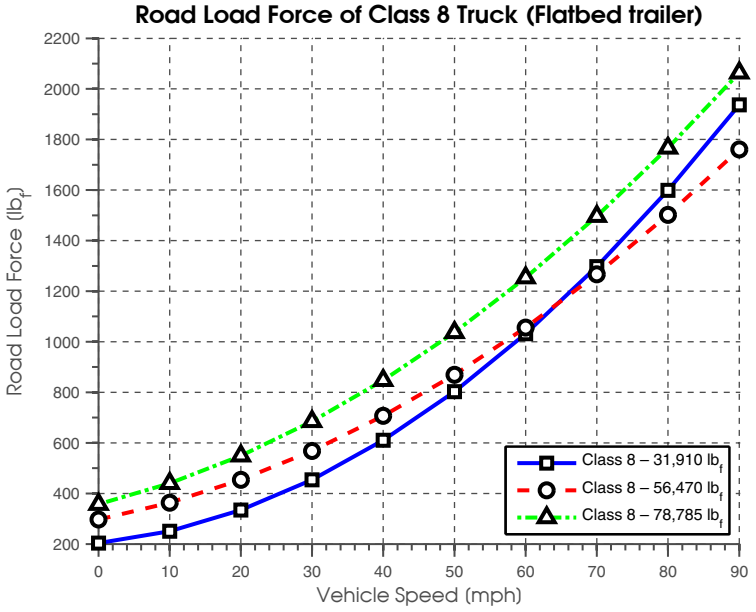

Figure 2.13 Road load force curves obtained from the present coastdown coefficients for an EPA Class 8 truck and flatbed trailer with 3 weight configurations.

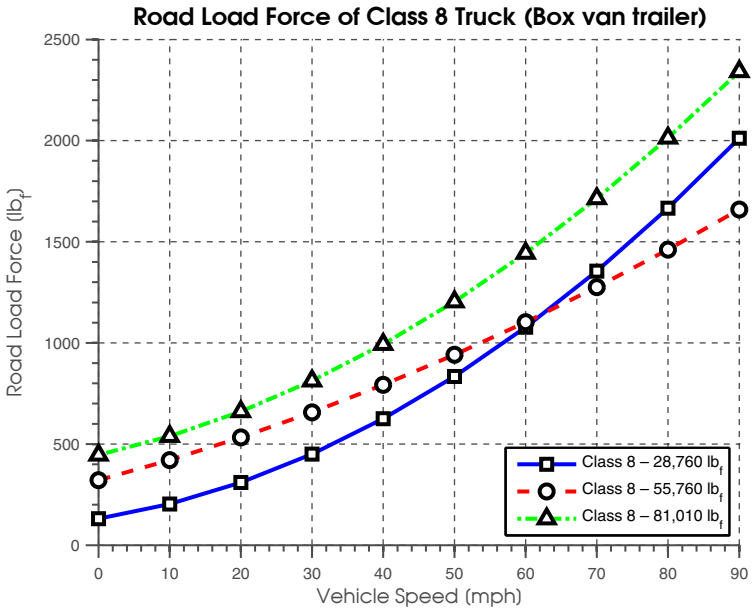

Figure 2.14 Road load force curves obtained from the present coastdown coefficients for an EPA Class 8 truck with box van trailer with 3 weight configurations.

In Figure 2.12, Figure 2.13, and Figure 2.14, the road load curves cross for some weight configurations relative to others. Petrushov (2009) states that lower tire pressures produce higher rolling resistance, which in turn can cause these curves to cross as it is shown experimentally in Figure 2.15. When the vehicle is loaded, the pressure in the tires increases due to the compression of the tires. Therefore, a change in rolling resistance can be expected. These crossings of the road load force curves may be explained by higher rolling resistance induced by lower tire pressure at the lower vehicle weight. This factor also reveals that there is an optimum loaded vehicle weight for the minimum road load force for speeds higher than 55 mph.

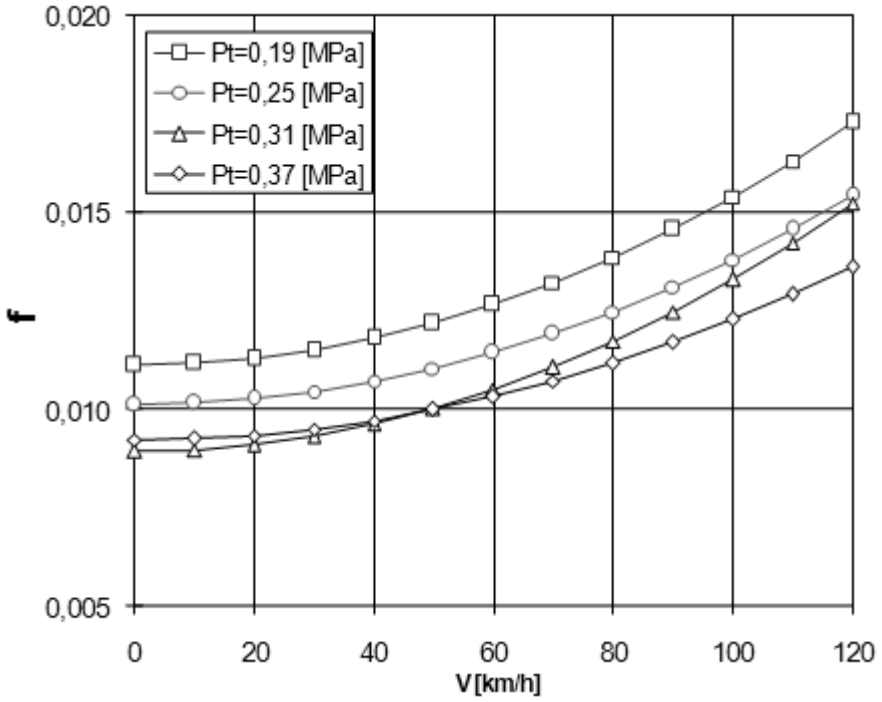

Figure 2.15 Rolling resistance coefficient f of the tire 175/65R14 due to vehicle speed V and inflation pressure P_t (Petrushov, 2009).

Generic Class 8 truck specifications can be estimated as shown in Table 2.4. The road load force for this generic vehicle was calculated via the fundamental method explained by Eqns. (2.1)-(2.3). Results were obtained for two weight configurations: 30,000 and 80,000 lb_f. Coastdown coefficients for these two vehicle weights were obtained via interpolation of the present coastdown coefficients from our experiments. A comparison of the results obtained using the present coastdown coefficients and via the road load versions of Eqns. (2.1)-(2.3) and Table 2.4 is shown in Figure 2.16 along with the MOVES results that were obtained by using the MOVES model parameters presented in Table 2.1.

Table 2.4 Generic Class 8 Truck Specifications

A_c	6.481 m^2
C_D	0.85
C_R	0.008

In Figure 2.16, the estimated road load force calculated using the road load versions of Eqns. (2.1)-(2.3) for the generic heavy-duty truck agrees closely with the road load force calculated using the coastdown coefficients in the MOVES model. However, the road load force results obtained using the present coastdown coefficients does not agree well with either the MOVES model or the fundamental approach (the road load versions of Eqns. (2.1)-(2.3) and Table 2.4) for either vehicle weight. This is due to the fact that the present coastdown coefficients include a term that is linear in vehicle speed whereas neither the MOVES model nor the simplified fundamental approach incorporates this term. Because we have illustrated the physical basis for a resistive force term that is linear in vehicle speed via Eqns. (2.8) and (2.9), we are confident that the road load force calculated using the present heavy-duty coastdown coefficients is more accurate than that obtained via either the MOVES model or the road load versions of Eqns. (2.1)-(2.3).

The coastdown results obtained in this study were also incorporated into the University of Texas Fuel Economy Model. Details of this model are provided in references (Welter *et al.*, 2009) and (Matthews *et al.*, 2011). Details are not presented here for the sake of brevity but the predictions of this model are included as a demonstration of both the use and accuracy of the present heavy-duty truck coastdown coefficients.

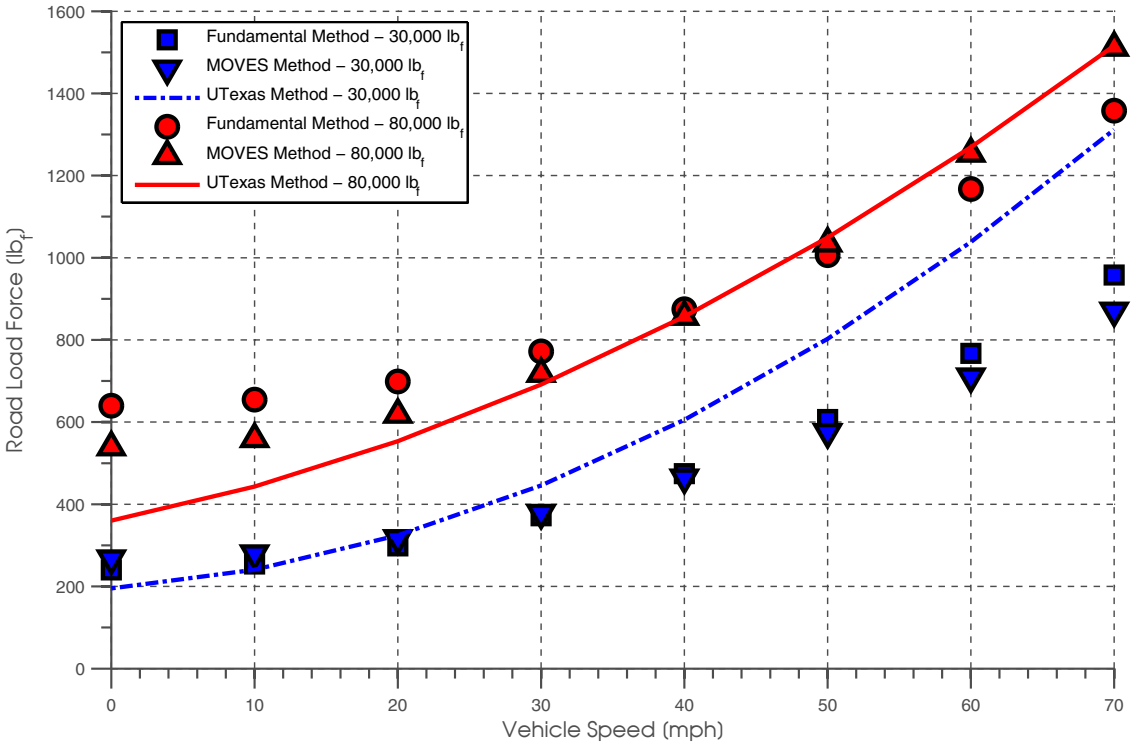

Figure 2.16 Comparison of the road load force obtained by adding the drag force to the rolling resistance of a generic Class 8 truck with the road load force calculated via two different sets of coastdown coefficients.

As mentioned previously, author also collected 54 drive cycles with three different Class 8 trucks, three weight configurations, three traffic congestion levels, and two drivers. All were taken on a 43 km (27 mile) section of Interstate 35 through downtown Austin, one of the five most congested traffic corridors in Texas. One of the drive cycles, taken with a 2001 model year Freightliner with one of the two drivers (identified as "Driver #2"), laden to 45,000 lb_f, during 9:30 AM traffic conditions, is shown in Figure 2.17. The elevation data shown in this figure was used in the UT Fuel Economy Model to calculate the instantaneous grade of the road but it is not the absolute elevation of the road from sea level since it was taken by the GPS data logger, but it is an accurate relative value. The maximum

uphill grade on this drive cycle was about 5.5% while the minimum was around -5.9%. Here it should be noted that drive cycles rarely include grades but they are important for heavy-duty vehicles.

While obtaining the drive cycle data, the fuel consumption rate of the trucks was logged with a DG Technologies DPA 4 Plus CAN/Bus data logger, from which the average fuel economy over the drive cycle was calculated (DG Technologies, 2012).

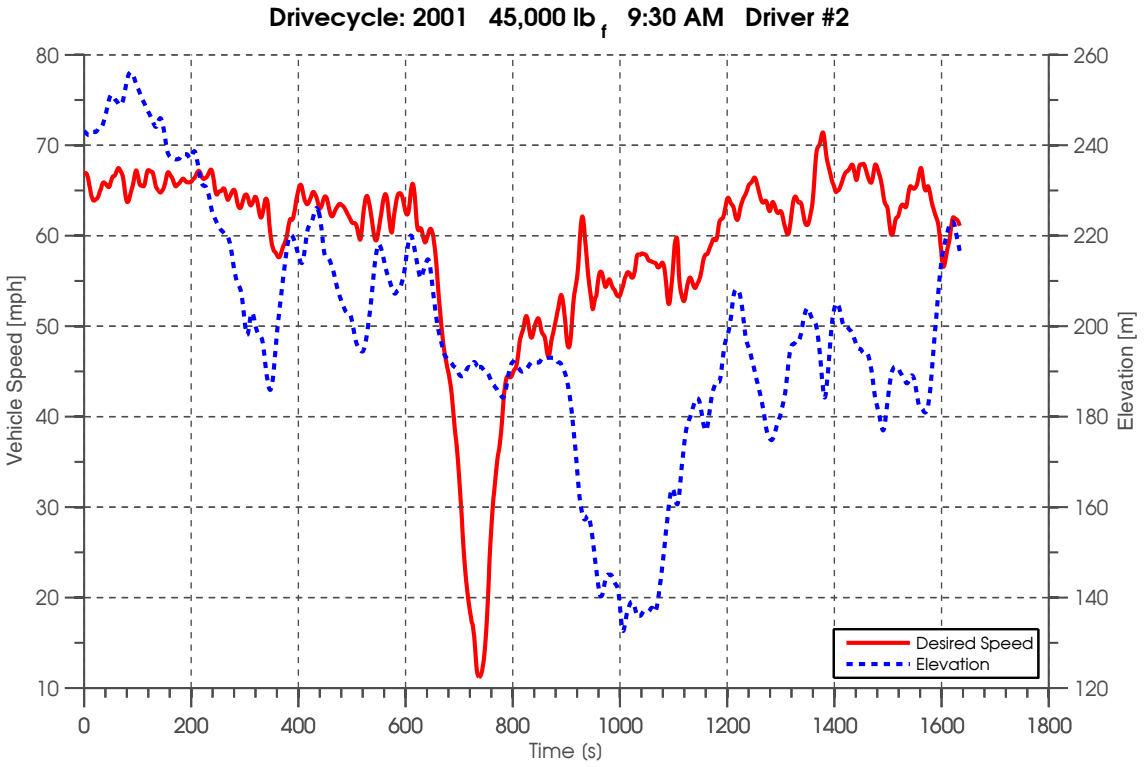

Figure 2.17 A sample drive cycle collected during 9:30 AM traffic conditions using a 2001 model year Class 8 truck laden to 45,000 lb_f driven by the second driver.

The UT Fuel Economy Model includes a "driver" sub-model that incorporates a shifting strategy and also controls the accelerator and brake pedals. This model also contains sub-models that account for the energy losses in the

transmission and differential. Figure 2.18 compares the desired speed (from the drive cycle that is supplied as an input) with the predicted ("actual") speed that the simulation generates. Obviously, the UT Fuel Economy Model is quite good at following the prescribed drive cycle even in the presence of a grade.

Table 2.5 lists the simulation results for the 9:30 AM drive cycle shown in Figure 2.17. As shown in Table 2.5, the distance covered by the truck predicted by the UT Fuel Economy Model was short by only 85 meters for the 9:30 AM drive cycle while it was short by about 110 meters for the (essentially free-flow) 11:00 AM drive cycle. Compared to the total drive cycle length of 43.3 km (26.9 miles), the error in the distance is about 0.20 and 0.26%, respectively, for each simulation.

Table 2.5 also compares the experimental fuel economy with the predicted fuel economy. The UT Fuel Economy Model under-estimates the fuel economy by 3.55% compared to the actual fuel economy for the 9:30 AM drive cycle while the model estimate is 2.89% lower than the actual fuel economy for the 11:00 AM drive cycle. Based on these results, it can be concluded that the use of the present coastdown coefficients in an accurate fuel economy model yields accurate fuel consumption predictions.

Figure 2.18 Comparison of the speed predicted using the UT Fuel Economy Model with the speed (and grade) input to this model for the 2001 Class 8 truck loaded to 45,000 lb_f during 9:30 AM congestion.

Table 2.5 Fuel Economy and Distance Comparison between the UT Fuel Economy Model and that Measured via the ECU.

45,000 lb_f	Fuel Economy [mpg] *From ECU*	Fuel Economy [mpg] *UT Predictions*	Distance Error [m]	Distance Error [%]
9:30 AM	7.88	7.60	-85.66	-0.20
11:00 AM	7.97	7.74	-110.75	-0.26

2.5 Summary and Conclusions

Coastdown tests were performed on heavy-duty trucks, which required an 11 km (7 mi) stretch of roadway. It was not possible to locate a state or federal highway in Texas for which such a road had a maximum grade of 0.5% in compliance with SAE Recommended Practices J1263 and J2263 (1996, 2008a). Therefore, a computational technique was developed to compensate for the grade, thereby allowing for the calculation of coastdown coefficients. This technique was validated by comparing the calculated coastdown coefficients for a light-duty truck, a 2008 Ford F-150, with the coastdown coefficients for this truck posted on EPA's website (2012). This comparison provided the conclusion that the present technique for accounting for the effects of grade is accurate. Thus, coastdown coefficients were generated for EPA Class 7 and Class 8 trucks, including Class 8 trucks with wide-single low rolling resistance tires and aerodynamic devices. Coastdown coefficients were calculated for the trucks as tested for empty, weighed-out, and "cubed-out" weight configurations.

The rolling resistance force from the present coastdown coefficients was compared against calculations using generic aerodynamic drag and rolling resistance coefficients for a Class 8 truck. These results were also compared with the rolling resistance calculated using the relevant coastdown coefficients in EPA's MOVES's model (Nam and Giannelli, 2005). The present coastdown coefficients include a term that is linear in speed while neither the MOVE's formulae nor the calculations via the generic drag and rolling resistance coefficients include this type of term. Thus, precise agreement between these three models cannot be expected. However, the calculations using the present coastdown coefficients do

agree reasonably well with both of the other techniques for the heavier loaded vehicle weight simulated (80,000 lb_f) but only agree with the other two techniques at low vehicle speeds for the lower vehicle weight simulated (30,000 lb_f). We argue that our technique is more accurate due to the inclusion of the term that is linearly speed dependent.

The coastdown coefficients and the drive cycles generated in the present study were also used in the University of Texas Fuel Economy Model to estimate the fuel consumption of heavy-duty vehicles operating on Texas roads. The UT Fuel Economy Model predictions for operation of a Class 8 truck operating over two different congestion levels with variable grade were compared to fuel economy data logged from a Class 8 truck. The model predictions were in excellent agreement with the measured fuel economy for both levels of traffic congestion. Based on these comparisons, it is concluded that the use of the present coastdown coefficients in an accurate fuel economy model yields accurate fuel consumption predictions.

Chapter 3

Quasi-Dimensional Direct Injection Diesel Engine Model

The objective of this part of the dissertation research was to develop a full cycle quasi-dimensional direct injection diesel engine model that would represent physical models of the in-cylinder processes accurately. Emphasis will be placed on modeling the combustion process quasi-dimensionally. On the other hand; the compression, expansion, and gas exchange stages are modeled via zero-dimensional single zone calculations. A full cycle simulation is necessary in order to: 1) capture the initial conditions of the closed section of the cycle (intake valve closing to exhaust valve opening) given the intake and the exhaust plenum conditions and 2) predict the brake specific fuel consumption.

In this section: 1) a brief development of the governing equations for a single zone open control volume will be given along with a source term in the energy equation due to combustion chemistry, 2) the developed governing equations will be simplified for the compression, expansion, and gas exchange processes, 3) engine sub-models (i.e. engine heat loss, blow-by mass flow, intake mass flow, etc.) will be presented, and 4) the quasi-dimensional combustion governing equations will be developed.

3.1 Governing Equations for a Control Volume

The governing equations for mass, species, and energy will be developed for an open engine cylinder control volume as shown in Figure 3.1. The most general form of each governing equation will be presented first. Each equation

will be simplified later for each specific process (such as the intake process and the combustion process) throughout the thermodynamic cycle. The contents of the cylinder volume are assumed to be homogenous and well-stirred except during the combustion phase.

3.1.1 Conservation of Mass

The total mass in the cylinder changes as a result of flow through the cylinder's inlets (i.e. intake air mass flow and fuel injection) and outlets (i.e. exhaust mass flow and blow-by). The rate of change of cylinder total mass, dm/dt, is the net in-flux of mass across the system boundaries.

$$\frac{dm}{dt} = \sum_{in} \dot{m}_{in} - \sum_{out} \dot{m}_{out} \tag{3.1}$$

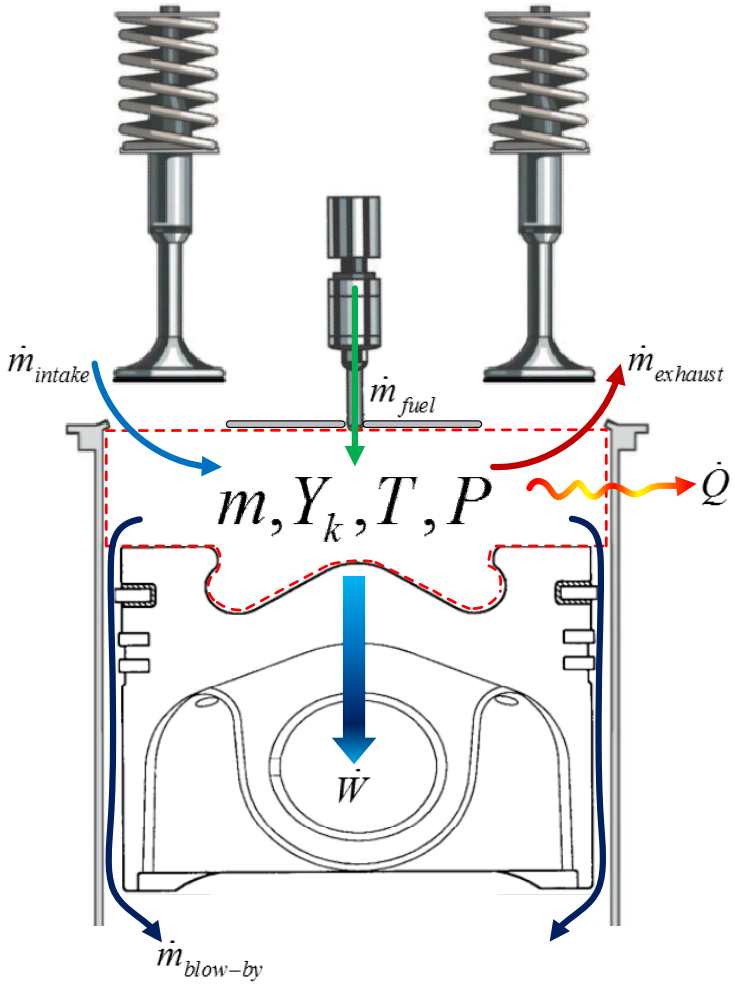

Figure 3.1 Engine cylinder control volume with intake, fuel injection, exhaust, and ring pack mass flow rates

3.1.2 Conservation of Species

The rate of change in the mass of each species, k, in the control volume is the sum of the net in-flux of species k mass and the generation/depletion of species k by chemical reaction

$$\frac{d\left(mY_k\right)}{dt} = \sum_{in} \dot{m}_{in} Y_{k,in} - \sum_{out} \dot{m}_{out} Y_k + \dot{m}_{k,gen} \tag{3.2}$$

where Y is the mass fraction of species k. The rate at which species k is generated (or consumed) through homogenous phase reaction is

$$\dot{m}_{k,gen} = V\dot{\omega}_k W_k \tag{3.3}$$

where V is the cylinder volume, $\dot{\omega}_k$ is the net production rate of species k per unit volume, and W_k is the molecular weight of species k. One can get the final form of the species conservation equation by expanding Eqn. (3.2) and applying mass conservation

$$\begin{aligned} \frac{d\left(mY_k\right)}{dt} &= m\frac{dY_k}{dt} + Y_k\frac{dm}{dt} \\ &= m\frac{dY_k}{dt} + Y_k\left[\sum_{in}\dot{m}_{in} - \sum_{out}\dot{m}_{out}\right] \end{aligned} \tag{3.4}$$

$$m\frac{dY_k}{dt} + Y_k\left[\sum_{in}\dot{m}_{in} - \cancel{\sum_{out}\dot{m}_{out}}\right] = \sum_{in}\dot{m}_{in}Y_{k,in} - \cancel{\sum_{out}\dot{m}_{out}Y_k} + \dot{m}_{k,gen} \tag{3.5}$$

$$\frac{dY_k}{dt} = \sum_{in}\frac{\dot{m}_{in}}{m}\left(Y_{k,in} - Y_k\right) + \nu\dot{\omega}_k W_k \tag{3.6}$$

where ν is the specific volume of the mixture.

3.1.3 Conservation of Energy

The rate of change of total energy in the cylinder volume is the net enthalpy in-flux minus the power produced and heat lost. The enthalpy leaving the control volume equals to the control volume enthalpy since the control volume is well stirred and homogeneous.

$$\frac{dU}{dt} = \sum_{in} \dot{m}_{in} h_{in} - h \sum_{out} \dot{m}_{out} - P\frac{dV}{dt} - \dot{Q}_{ht} \tag{3.7}$$

The conservation of energy equation can be written in the following form as well:

$$\frac{dH}{dt} = \sum_{in} \dot{m}_{in} h_{in} - h \sum_{out} \dot{m}_{out} - \dot{Q}_{ht} \tag{3.8}$$

where H is the total enthalpy.

For an ideal gas, one can write the total internal energy U in terms of the species mass fractions:

$$U = m \sum_{k} Y_k u_k \left(T\right) \tag{3.9}$$

The left hand side of Eqn. (3.7) can be expanded by using Eqn. (3.9):

$$\frac{dU}{dt} = u\frac{dm}{dt} + mc_v \frac{dT}{dt} + m \sum_{k} u_k \frac{dY_k}{dt} \tag{3.10}$$

Combining Eqns. (3.6), (3.7), and (3.10) in order to obtain the mass average cylinder temperature yields:

$$mc_v \frac{dT}{dt} = \sum_{in} \dot{m}_{in} \left(h_{in} - \sum_{k} u_k Y_{k,in} \right) - P\nu \sum_{out} \dot{m}_{out} - \sum_{k} \dot{m}_{k,gen} u_k - P\frac{dV}{dt} - \dot{Q}_{ht} \tag{3.11}$$

To relate the rate of change of the mass average temperature to the rate of change of pressure, the Ideal Gas Law is used in its differential form. Taking the log of the Ideal Gas Law and differentiating yields

$$\frac{\dot{P}}{P} + \frac{\dot{V}}{V} = \frac{\dot{m}}{m} + \frac{\dot{R}}{R} + \frac{\dot{T}}{T} \tag{3.12}$$

where R is the specific gas constant of the mixture which can be expressed as $\sum_k Y_k R_k$. We can then write the rate of change of pressure as:

$$\frac{dP}{dt} = P\left[\frac{\dot{m}}{m} + \frac{\sum_k \dot{Y}_k R_k}{R} + \frac{\dot{T}}{T} - \frac{\dot{V}}{V}\right] \tag{3.13}$$

The final set of governing equations for the open homogeneous control volume consists of Eqns. (3.1), (3.6), (3.11), and (3.13), creating a set of four nonlinear, ordinary differential equations. The state variables are

$$\left\{m, Y_k, T, P\right\} \tag{3.14}$$

and sub-models are used to describe all other variables and time derivatives (i.e. fuel injection, exhaust, heat loss, and blow-by mass flow rates, etc.). These sub-models are described in later sections.

3.2 Compression Process

The compression process starts at intake valve closing (**IVC**) and ends at the start of fuel injection (**SOI**). Although the compression stroke normally begins before IVC and ends after SOI, here the compression "process" refers to the portion of the compression stroke during which the cylinder is essentially a fixed mass system except for the minor change in trapped mass due to flow into, and

possibly completely through, the piston ring pack. Therefore, the overall cylinder mass conservation equation can be written as:

$$\frac{dm}{dt} = -\dot{m}_{RP} \tag{3.15}$$

It is assumed that the mass entering (when the pressure within the piston ring pack is higher than the cylinder pressure) to the cylinder volume through the blow-by process has the same composition as the cylinder volume contents. Hence, the species conservation equation simplifies to only the species generation term which is zero since there is no reaction in the cylinder during the compression process.

$$\frac{dY_k}{dt} = \nu\dot{\omega}_k W_k = 0 \tag{3.16}$$

The energy conservation equation for the compression process is:

$$mc_v \frac{dT}{dt} = \dot{m}_{in}\left(h_{in} - \sum_k u_k Y_{k,in}\right) - P\nu\sum_{out}\dot{m}_{out} - P\frac{dV}{dt} - \dot{Q} \tag{3.17}$$

The first term on the right hand side exists only when there is in-flow from the ring pack to the cylinder volume. The rate of change of pressure can be simplified as:

$$\frac{dP}{dt} = P\left[\frac{\dot{m}}{m} + \frac{\dot{T}}{T} - \frac{\dot{V}}{V}\right] \tag{3.18}$$

3.2.1 Engine Geometry

The cylinder volume as a function of crank angle, the rate of change of cylinder volume with respect to crank angle, and the total in-cylinder surface area of an internal combustion engine will be presented in this section.

The geometry of an internal combustion engine is shown in Figure 3.2, where V_c is the clearance volume, V_s is the swept volume, B is the bore of the cylinder, S is the piston stroke, l is the connecting rod length, a is the crank radius, s is the distance between the crank axis and the piston pin axis, θ is the crank angle, **TDC** is top dead center, and **BDC** is bottom dead center.

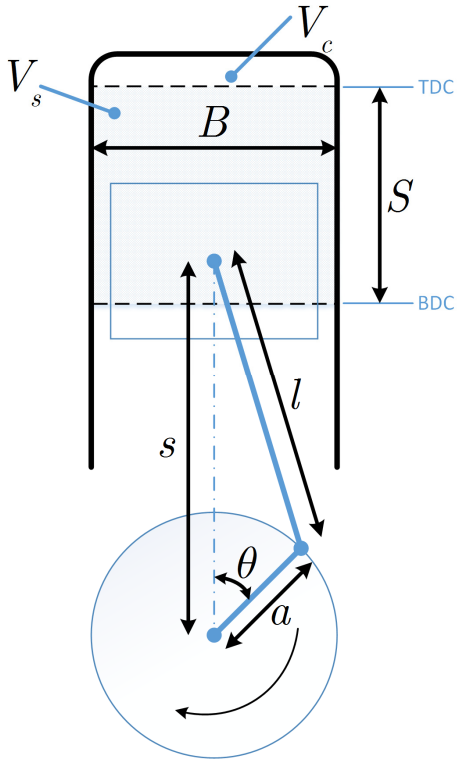

Figure 3.2 The geometry of the internal combustion engine cylinder, re-created from (Heywood, 1988, p. 44)

Using the slider crank model, one can calculate the total cylinder volume at any crank angle of the piston as

$$V = V_c + \frac{\pi B^2}{4}\left(l + a - s\right) \tag{3.19}$$

and s, the distance between centers of the piston pin and crank is given by

$$s = a\cos\theta + \left(l^2 - a^2\sin^2\theta\right)^{1/2} \tag{3.20}$$

Substituting Eqn. (3.20) into Eqn. (3.19), one can get the cylinder volume as a function of crank angle

$$V = V_c\left\{1 + \frac{1}{2}\left(r_c - 1\right)\left[R + 1 - \cos\theta - \left(R^2 - \sin^2\theta\right)^{1/2}\right]\right\} \tag{3.21}$$

where r_c is the compression ratio, and R is the ratio of the connecting rod length to crank radius which is $R = l/a$. The rate of change of cylinder volume appears in the conservation of energy, Eqn. (3.11), and the derivative of the Ideal Gas Law, Eqn. (3.13). By taking the derivative of Eqn. (3.21) with respect to crank angle, one can get

$$\frac{dV}{d\theta} = \frac{1}{2}V_c\left(r_c - 1\right)\sin\theta\left(1 + \frac{\cos\theta}{\left(R^2 - \sin^2\theta\right)}\right) \tag{3.22}$$

and the differential crank angle is $d\theta = \omega \cdot dt$ where ω is the engine speed in radians per second.

Similarly, the liner surface area as a function of crank angle is a relevant parameter for the heat transfer formulation, and it is given by

$$A_l = \pi B\Big(l + a - s\Big) \tag{3.23}$$

Substituting Eqn. (3.20) into Eqn. (3.23), one can get the liner surface area as a function of crank angle

$$A_l = \frac{\pi BS}{2}\left[R + 1 - \cos\theta - \Big(R^2 - \sin^2\theta\Big)^{1/2}\right] \tag{3.24}$$

3.2.2 Ring Pack Flow Sub-model

The ring pack model implemented in the engine model is a zero-dimensional ring-flow model based on the model developed by Namazian and Heywood (1982) and Roberts and Matthews (1996). Typically, the ring pack consists of two compression rings and one oil control ring. Consequently, the final assembly creates seven zones as shown in Figure 3.3.

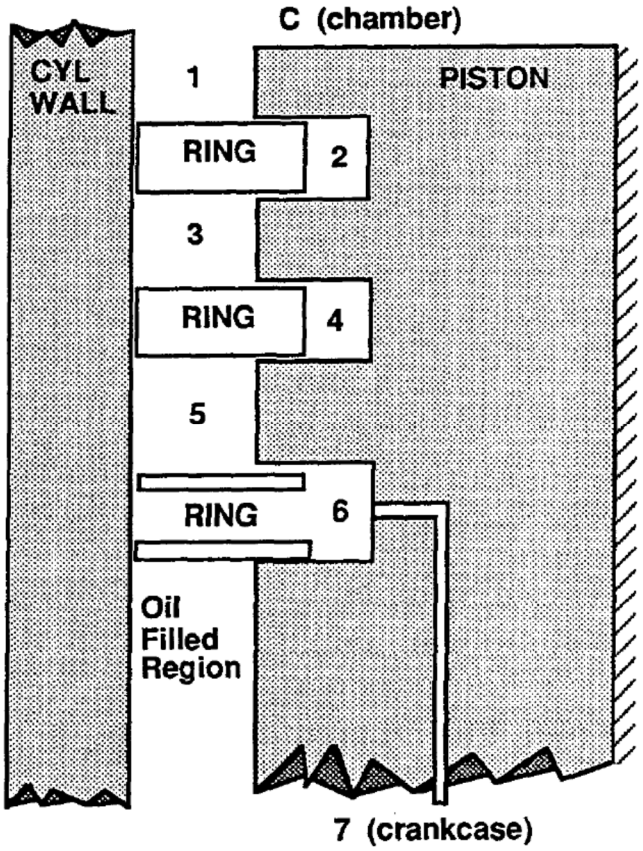

Figure 3.3 Ring pack geometry and zones (Roberts and Matthews, 1996)

The flow in the piston crevice region is assumed to be laminar compressible flow and, assuming orifice flow, the mass flow through the ring end gaps can be written as

$$\dot{m}_{end\ gap} = C_d A_g \rho c \eta \tag{3.25}$$

where C_d is the discharge coefficient ($C_d = 0.7$ was used in this study), A_g is the effective gap area, ρ is the cylinder gas density evaluated at the cylinder wall

temperature, c is the local speed of sound, and η is a compressibility factor given by Eqn. (3.26).

$$\eta = \begin{cases} \frac{2}{\gamma-1}\left[\left(\frac{P_d}{P_u}\right)^{\frac{2}{\gamma}} - \left(\frac{P_d}{P_u}\right)^{\frac{\gamma+1}{\gamma}}\right]^{1/2} & \frac{P_d}{P_u} > \left(\frac{2}{\gamma+1}\right)^{\frac{\gamma}{\gamma-1}} \\ \left(\frac{2}{\gamma+1}\right)^{\frac{\gamma+1}{2(\gamma-1)}} & \frac{P_d}{P_u} \leq \left(\frac{2}{\gamma+1}\right)^{\frac{\gamma}{\gamma-1}} \end{cases} \tag{3.26}$$

where γ is the ratio of specific heats, P_u is the upstream pressure, and P_d is the downstream pressure. The mass flow rates through the top and bottom faces (e.g. Zone 1 to Zone 2 in Figure 3.3), which are called "edge" flows, are calculated from

$$\dot{m}_{edge} = \frac{h^2\left(P_u^2 - P_d^2\right)A_{cl}}{24W_r\mu_{gas}RT} = \pi ID_{ring}\frac{h^3\left(P_u^2 - P_d^2\right)}{24W_r\mu_{gas}RT} \tag{3.27}$$

where h is the cross-sectional area of the gap between the top (or bottom, depending upon the ring's instantaneous position within the ring groove) of the ring and the upper (or lower) surface of the ring groove, W_r is the width of the ring, μ_{gas} is the local gas dynamic viscosity, R is the gas constant, T is the gas temperature, A_{cl} is the area perpendicular to the gas flow between the ring and the top (or bottom) surface of the groove, and ID_{ring} is the internal diameter of the piston ring. Zone 1 and Zone 7 have known pressures, therefore the system of equations for the other crevice zones are:

$$\frac{dP_2}{dt} = \frac{P_2}{m_2}\left(\dot{m}_{12} - \dot{m}_{23}\right) \tag{3.28}$$

$$\frac{dP_4}{dt} = \frac{P_4}{m_4}\left(\dot{m}_{34} - \dot{m}_{45}\right) \tag{3.29}$$

$$\frac{dP_6}{dt} = \frac{P_6}{m_6}\left(\dot{m}_{56} - \dot{m}_{67}\right) \tag{3.30}$$

$$\frac{dP_3}{dt} = \frac{P_3}{m_3}\left(\dot{m}_{23} + \dot{m}_{13} - \dot{m}_{34} - \dot{m}_{35}\right) \tag{3.31}$$

$$\frac{dP_5}{dt} = \frac{P_5}{m_5}\left(\dot{m}_{45} + \dot{m}_{35} - \dot{m}_{56}\right) \tag{3.32}$$

The mass flow rates for numerically adjacent zones (e.g. 1-2, 2-3, etc.) are given by "edge" mass flow rates, Eqn. (3.27), and mass flow rates for zones separated by two integers (e.g. 1-3, 3-5) are given by "end gap" mass flow rates, Eqn. (3.25). The ring pack mass flow rate in Eqn. (3.15) can be expressed as the sum of "edge" and "end gap" mass flow rates from Zone 1 to Zone 2 and Zone 3

$$\dot{m}_{RP} = \dot{m}_{12} + \dot{m}_{13} \tag{3.33}$$

Of course, Zone 3 feeds mass into Zones 4 and 5 or, if the pressure gradient is appropriate, reverse flow back into Zone 1 can occur. The main point here is that flow into the ring pack from the cylinder, or flow back out of the ring pack into the cylinder, can be calculated in a straightforward manner with minimal burden on computational time.

3.2.3 Heat Transfer Sub-model

The heat transfer (loss) term appearing in the energy equation will be quantified in this section. The peak cylinder temperatures of a DI diesel engine

may surpass 2500 K locally; hence convection, conduction, and radiation (due to the particulate matter in diesel combustion) heat transfer mechanisms play an important role. Using a lumped Newton's law of cooling model for the cylinder volume, one can express heat transfer as

$$Q_{ht} = h\left[A_h \left(T_{avg} - T_h \right) + A_p \left(T_{avg} - T_p \right) + A_l \left(T_{avg} - T_l \right) \right] \qquad (3.34)$$

where h is the overall heat transfer coefficient, A_h is the cylinder head surface area, A_p is the piston crown surface area, A_l is the instantaneous liner surface area, given by Eqn. (3.24), T_{avg} is the average temperature of the cylinder gases, T_h is the temperature of the cylinder head, T_p is the piston surface temperature and T_l is the cylinder liner wall temperature. The heat transfer coefficient can be estimated using empirical correlations such as those developed by Annand (1963), Woschni (1967), and Hohenberg (1979). Woshni's correlation is explained by Heywood (1988):

$$h = 3.26 B^{-0.2} P^{0.8} T_{avg}^{-0.55} w^{0.8} \qquad (3.35)$$

where the heat transfer coefficient is in W/m^2K, B is the cylinder bore in m, P is the cylinder pressure in kPa, T_{avg} is in K, and w is the mean cylinder gas speed in m/s. The mean cylinder gas speed is determined from:

$$w = C_1 \overline{S}_p + C_2 \frac{V_d T_{IVC}}{P_{IVC} V_{IVC}} \left(P - P_m \right) \qquad (3.36)$$

where $\overline{S}_p$ is the mean piston speed, V_d is the displacement volume, T_{IVC} is the cylinder bulk temperature at intake valve closure (IVC), P_{IVC} is the cylinder pressure at IVC, V_{IVC} is the cylinder volume at IVC, and P, P_m are the cylinder pressure and motoring pressure at the same crank angle. Constants C_1 and C_2 are given as:

a) Compression

$$C_1 = 2.28, \qquad C_2 = 0 \tag{3.37}$$

b) Combustion and Expansion

$$C_1 = 2.28, \qquad C_2 = 3.24 \cdot 10^{-3} \tag{3.38}$$

c) Gas Exchange

$$C_1 = 6.18, \qquad C_2 = 0 \tag{3.39}$$

Set of Governing Equations

The final set of governing equations for the compression process consists of Eqns. (3.15)-(3.36), creating a set of nine nonlinear, ordinary differential equations. The state variables are

$$\left\{ m, Y_k, T, P, P_2, P_3, P_4, P_5, P_6 \right\} \tag{3.40}$$

3.3 Combustion Process

The diesel engine combustion process is a very complex phenomenon due to turbocharging, **EGR** (Exhaust Gas Recirculation), high pressure fuel injection, advanced fuel injection strategies (e.g. more than one injection per cylinder per cycle), etc. Therefore, in order to predict fuel economy and emissions accurately, a quasi-dimensional engine model must rely on physical models more rather than on empirical results obtained from engine tests. In this section, the quasi-dimensional diesel combustion model will be discussed in terms of 1) Conceptual Model, 2) Zone Description, and 3) Governing Equations.

3.3.1 Conceptual Modeling of Diesel Combustion Phenomena

Deep understanding of the diesel combustion and chemical kinetics processes are necessary in order to develop computer simulations that are capable of predicting engine performance, fuel consumption, and emissions. Prior to the developments in laser imaging technology, the only available data was the cylinder pressure versus cylinder volume data and the apparent heat release rate that is derived from this pressure trace. These data provide little information in regard to how the combustion occurs inside the combustion chamber. In the following sub-sections, first a brief summary of the pre-laser conceptual models which are based on cylinder pressure measurements and constant volume test vessel spray experiments will be presented, and then the new conceptual model which is based on laser–sheet images of the diesel spray and combustion process will be introduced.

3.3.1.1 Pre-laser Conceptual Models

By using cylinder pressure data and constant volume spray experiments, Hiroyasu and Kadota (1976) developed a conceptual model of direct injection diesel engine combustion and this model has been used widely (Im and Huh, 2000; Jung and Assanis, 2001; Zhou, Zhou and Clelland, 2006; Perini and Mattarelli, 2011). In this pre-laser ("old") conceptual model, it is assumed that the fuel spray is distributed into parcels and in each parcel, hot air causes the liquid fuel to breakup into fine droplets as shown in Figure 3.4 (a). The parcels located outside of the core fuel spray mix with air during the ignition delay. At the end of the ignition delay, premixed mixture burns and the unmixed fuel core mixes with air and combustion products. Hiroyasu and Kadota believed that mixing controlled combustion onset at the end of the premixed combustion stage. Scientists also assumed that all fuel-air packages burn stoichiometrically.

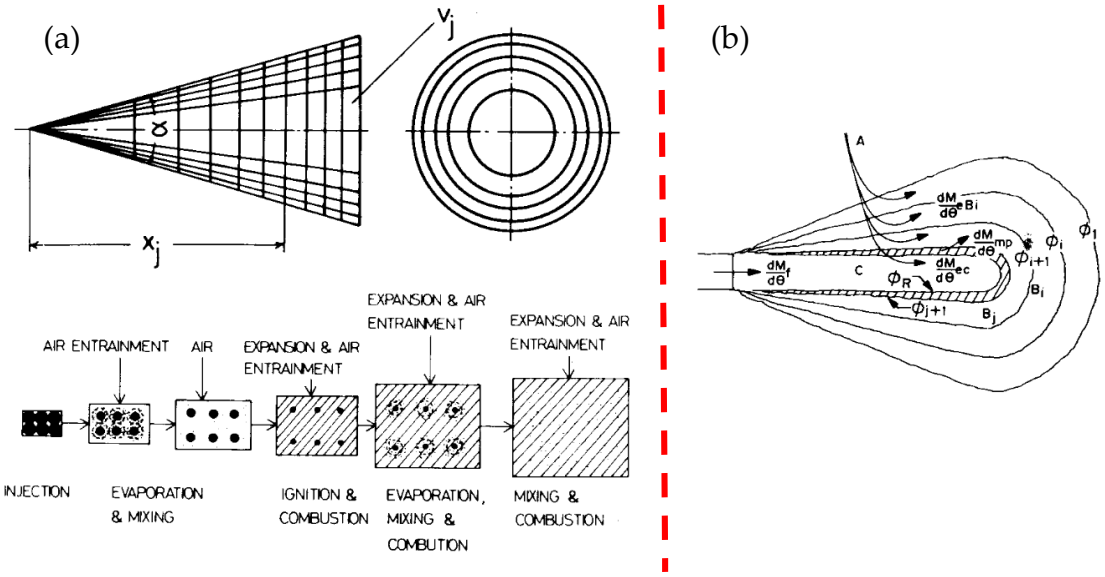

Figure 3.4 Pre-laser conceptual diesel multi–zone models: **(a)** Hiroyasu and Kadota (1976): Divided packages of the spray (top) and schematic diagram of the spray combustion (bottom) shown, **(b)** Chiu, Shahed and Lyn (1976): Schematic representation of zones and entrainment rates for a spray mixing model.

In the same year as Hiroyasu and Kadota's combustion model, another conceptual model was proposed by Chiu, Shahed and Lyn (1976) and this model was based on shadowgraph pictures and Schlieren movies obtained from constant volume test vessel spray experiments. Chiu and his colleagues described the diesel combustion process as the fuel spray having a fuel rich liquid core and the fuel distributed in a Gaussian like distribution with increasing radius. Moreover, the equivalence ratio is distributed from the lean flammability limit at the periphery of the spray to the rich limit at the core as shown in Figure 3.4 (b). After premixed combustion ended, as by Hiroyasu and Kadota, it is assumed that combustion occurred solely in the diffusion flame and is confined to the periphery of the flame. Moreover, soot was believed to be generated in the shell like region around the periphery.

3.3.1.2 Post-laser Conceptual Model

With the advances in the imaging techniques of engine sprays and combustion in the 1990s, it became well recognized that analogies with steady flames in furnaces and gas turbines (Faeth, 1977; Agnew, 1985) do not apply in the highly transient diesel engine combustion. A major development in conceptual modeling of how direct injection (**DI**) diesel combustion occurs came with the analysis performed by Dec (1997) and Flynn *et al.* (1999). Dec used laser-sheet imaging and other recent optical data to synthesize a conceptual model of diesel combustion. The idea of the temporal evolution of the fuel jet and events occurring in the reacting jet replaced the earlier concepts of diffusion flames occurring around the fuel droplets and pure-fuel spray core, proposed by Hiroyasu & Kadota (1976) and Chiu *et al.* (1976) respectively. A review of the conceptual model developed by Dec (1997) and Flynn and his colleagues (1999) is given below.

The temporal evolvement of the conventional DI diesel combustion from the start of injection (**SOI**) up through the early part of the mixing controlled burn is summarized in Figure 3.5 along with the corresponding injector needle lift and apparent heat release rate (**AHRR**) curves. It should be noted that, even though diesel combustion is highly turbulent, for simplicity in this synthesis, the effects of turbulence, swirl, and wall impingement are neglected while the surfaces are drawn smoothly. Moreover, the description given is for a certain engine and operating condition[3], and therefore the quantitative information is only symbolic.

[3] Cummins N–14 DI diesel engine with a bore of 139.7 mm and a stroke of 152.4 mm (2.34 liters) used in this research with all data taken at an engine speed of 1200 rpm (Dec, 1997).

Injection starts at 11° before top dead center (**BTDC**) and the time of the images in Figure 3.5 are referenced to this point: i.e. 1° **ASI** (After Start of Injection).

Initially, the dark brown region labeled as liquid fuel covers the whole cross section of the fuel jet as shown at 1° ASI. As high pressure liquid fuel is injected into the hot cylinder gases, hot air is entrained, forming a mixture of air and fuel droplets: due to heating by the air, and because the boiling temperature of diesel fuel (~430 K) is well below the gas temperature (~950 K), fuel readily evaporates. Then, a fuel-vapor/air mixture starts to develop along the sides of the fuel jet (2° ASI). There is a maximum penetration distance for the liquid fuel jet, called the ***liquid length***, of the order of about 20 mm (Espey and Dec, 1995; Dec, 1997; Siebers and Higgins, 2001). Beyond the liquid length, there is no more liquid fuel, i.e., entrainment of hot air into the jet has been sufficient to vaporize all the liquid fuel emerging from the injector.

At 3° ASI, the liquid fuel reaches the liquid length, as its size is not changing in the remaining figures. Chemiluminescence (emission of light as a result of chemical reaction) appears at 3° ASI downstream from the jet and the apparent heat release rate (AHRR) increases at this time as shown in Figure 3.5. It is not known if the chemiluminescence occurs at the surface or volumetrically throughout the fuel-vapor/air mixture at this stage. However, by 4.5° ASI most of the chemiluminescence is coming from fuel-vapor/air mixture in the leading portion of the jet. The temperature in the fuel-vapor/air zone is around 825 K which is well beyond the auto-ignition temperature of diesel fuel (~500-550 K) (Setchkin, 1954; International Programme on Chemical Safety, 1996). Then, the sequence of low-to-intermediate temperature reactions progresses to the energy release stage, and auto-ignition occurs in the premixed zone. Fuel breaks down

by 5° ASI and large **PAHs** (poly-aromatic hydrocarbons) form almost uniformly in the leading portion of the jet and the cylinder pressure rises rapidly. By 6° ASI, small soot particles form throughout the downstream portion of the fuel jet due to the very high equivalence ratio (2-4) in the premixed burn. The soot and PAH distributions show cycle to cycle variation and it is difficult to define a pattern.

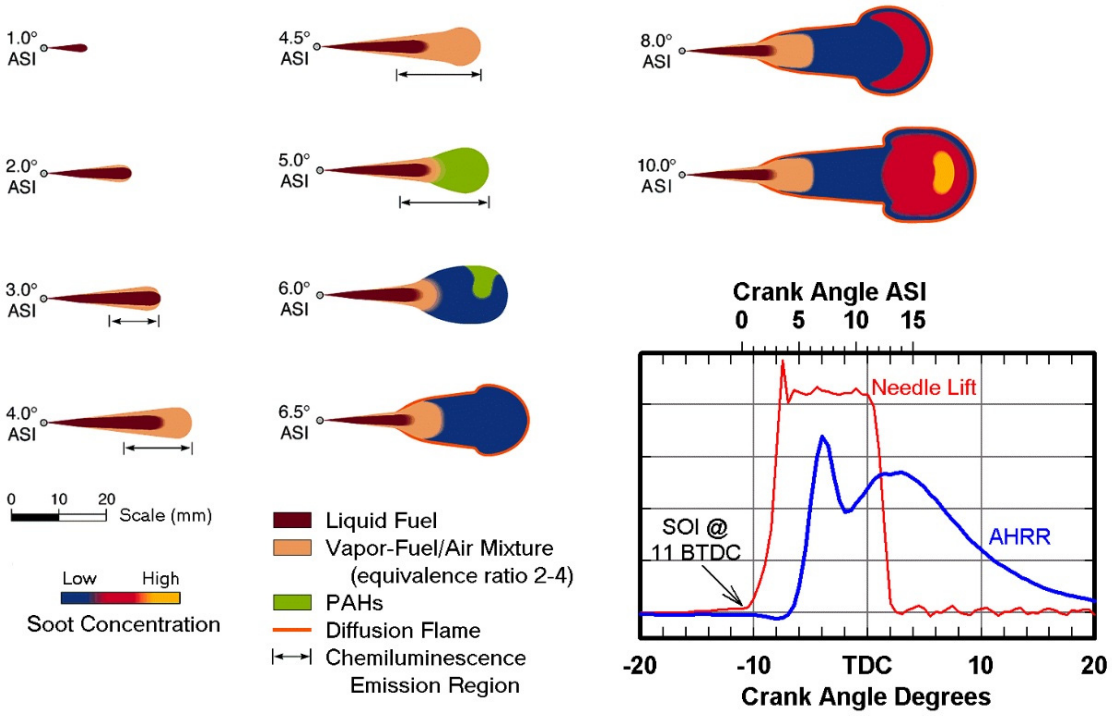

Figure 3.5 A temporal sequence of schematics showing how DI diesel combustion evolves from the SOI (Start of Injection) up through the early part of the mixing controlled burn. (1200 rpm–1°=139μs) (Flynn *et al.*, 1999)

A diffusion flame develops between 5.5° and 6.5° ASI at the periphery of the jet between the fuel-rich premixed burn products and the surrounding air where the equivalence ratio of the mixture is stoichiometric. This thin diffusion flame completely surrounds the downstream portion of the jet including the fuel-

vapor/air mixture and a portion of the liquid column. The distance from the injector nozzle to the edge of the diffusion flame is called the ***lift-off length***. Due to the higher temperatures in the diffusion flame, the liquid column evaporates more readily and the liquid length becomes 2 to 3 mm shorter while the fuel-vapor/air mixture zone grows. Partially burned premixed combustion products; especially unburned hydrocarbons, CO, H_2, and soot feed the diffusion flame from inside of the jet while air feeds from the cylinder wall side. It should be noted that premixed combustion and diffusion combustion coexist during some portion of the diesel combustion and they are no longer sequential.

Larger soot particles are observed at the periphery of the jet where the diffusion flame exists, however the soot volume concentration remains similar to that of the center region, where soot particles are smaller. As the 8° ASI schematic suggests, the premixed region continues to grow as the diffusion flame temperature increases due to supplied "fuel-rich" premixed burn products. As a result, the head of the jet also grows. A region of soot particles even larger than the particles at the jet periphery starts to form near the leading edge as the rich jet of combustion products from the rich premixed flame loses momentum and a recirculation zone is formed.

As most of the fuel rich fuel-vapor/air mixture is consumed, the burning jet transforms from the premixed combustion to a mixing controlled combustion phase and becomes quasi-steady as the 10° ASI schematic shows. Figure 3.6 shows the conceptual model of mixing controlled conventional DI diesel combustion prior to the end of injection (**EoI**) and this concept follows the 10° ASI.

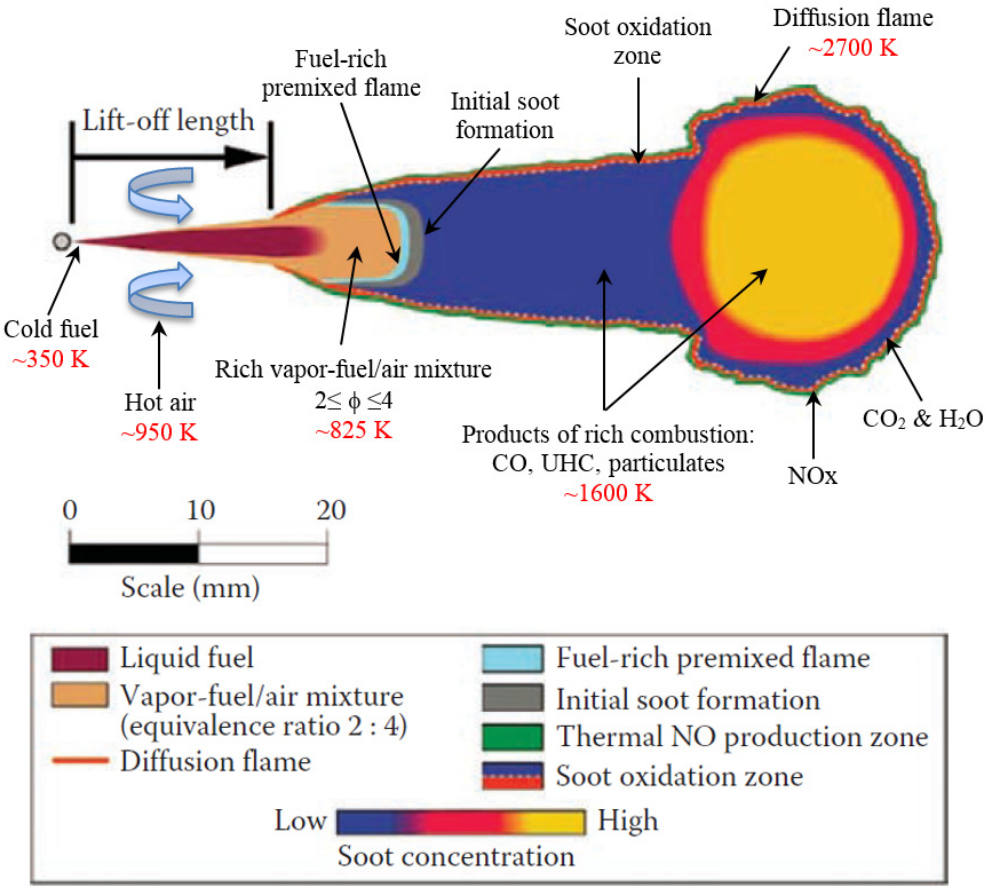

Figure 3.6 Conceptual model of conventional DI diesel combustion characterized by a sequence of processes occurring in a fully developed reacting jet developed by Dec (1997) and Flynn *et al.* (Flynn *et al.*, 1999).

In addition to the discussed premixed combustion zone and the evolvement of the spray in Figure 3.5, Figure 3.6 shows initial soot formation and soot and NOx production areas in the mixing controlled combustion phase. As shown with the gray color, the initial soot occurs downstream of the hypothesized standing fuel-rich premixed flame. The soot particles developed in this region are relatively small compared to the soot particles located at the head region of the spray. It is

believed that small particles combine and grow in size as soot flows downstream. Some portion of these small soot particles oxidize in the diffusion flame and result in high OH radical concentrations in the diffusion flame zone. Soot oxidation is indicated by the dashed white line between low soot concentration and the diffusion flame in Figure 3.6.

The quasi-steady combustion phase ends at the end of the fuel injection. The later portion of the combustion process is not well understood. A likely scenario for the remaining combustion process can be 1) the last injected liquid-fuel droplets will continue to flow downstream and entrained air will evaporate the liquid fuel and form a rich fuel-vapor/air mixture, 2) due to the decreased momentum of the liquid column, the lift-off length will move upstream toward the injector, 3) eventually, the diffusion flame surrounds the entire jet and some of the liquid-fuel will be used by this flame since large soot particles are observed upstream of the jet immediately following the end of injection (Dec, 1997), 4) the standing premixed flame will move upstream by consuming premixed fuel-vapor/air mixture and eventually will disappear when the last liquid fuel has evaporated and been consumed, 5) the jet will become a diffusion-only combustion process with unburned hydrocarbons, CO, H_2, and soot filling the inside and air on the cylinder wall side, and 6) diffusion combustion will continue until either it consumes all the mass enclosed or until the cylinder temperature does not support combustion anymore due to the expansion by the piston motion. Due to the momentum of the spray, even in large bore engines, the jet can (depending upon the engine load, and the duration of fuel injection) reach the piston bowl walls and impinge on the walls. By the time of the impingement, the

heat release is nearly complete and the impingement will affect only the engine emissions. It is possible that a large jet will split into pockets and have diffusion flames around each pocket due to the vortices created by impingement and the cylinder swirl (Miles, 2000).

3.3.2 Zone Description

The conceptual model described in Section 3.3.1.2 is applied in this section to develop the quasi-dimensional direct injection (DI) diesel engine combustion model. The combustion chamber is divided into six zones as shown in Figure 3.7.

Zone 1: Liquid-vapor fuel and entrained air that starts from the injector nozzle and continues up to the liquid length, s_{LL} (maximum liquid penetration length).

Zone 2: Fuel-vapor and entrained cylinder gas zone that starts from the liquid length and fills the conical volume beneath Zone 1 in Figure 3.7. The volume of this zone is determined from the momentum balance between injected fuel mass and entrained air. After auto ignition, Zone 2 transforms and moves downstream while a fresh Zone 2, which is called Zone 2', is forming.

Zone 2': Fresh fuel-vapor coming from Zone 1 and entrained cylinder gas forms Zone 2' when auto-ignition of Zone 2 starts.

Zone 3: Standing rich premixed flame zone where prepared fuel rich mixture (Zone 2') is burned and produces products to fill Zone 4; especially unburned hydrocarbons, CO, H_2, and soot.

Zone 4: Zone 2 can be called Zone 4 in the quasi-steady form, since combustion products in this zone have connection to the initial formation of Zone 2. In order to minimize confusion after auto-ignition Zone 2 is named Zone 4. In the quasi-

steady form, the standing premixed flame feeds Zone 4 and the combustion products eventually feed the diffusion flame.

Zone 5: Diffusion flame zone where the rich premixed combustion products oxidize, envelops the jet starting from the lift-off length, s_{LoL}, up to the spray tip.

Zone 6: Cylinder gases zone that contains air and EGR surrounding the other five zones.

Zone 1 : Liquid-vapor fuel and entrained air mixture
Zone 2' : Fuel-vapor and entrained cylinder gas mixture
Zone 3 : Standing rich premixed flame
Zone 4 : Rich premixed combustion products
Zone 5 : Diffusion flame
Zone 6 : Cylinder gases surrounding the jet

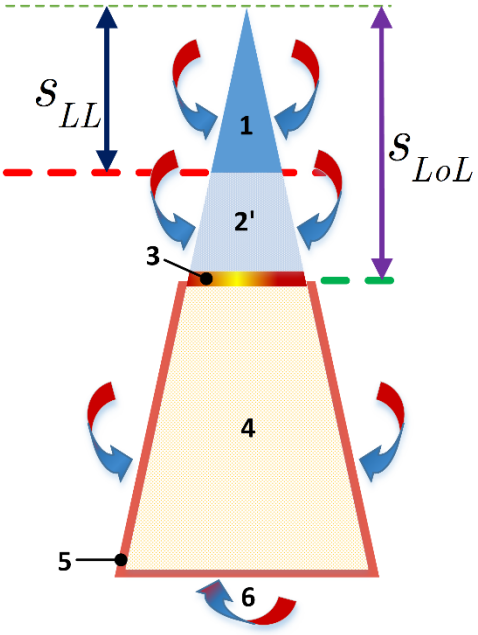

Figure 3.7 Schematic diagram of the quasi-steady jet showing DI diesel combustion in six zones.

The temporal evolution of the quasi-dimensional DI diesel combustion zones from the start of injection (SOI) to the quasi-steady form is shown in Figure 3.8. The injected liquid fuel fills Zone 1 and mixes with the surrounding hot gases entrained into this zone. Some portion of the liquid fuel evaporates at the periphery of Zone 1 as shown in Figure 3.5. Eventually, Zone 1 reaches the liquid

length (maximum liquid length) and Zone 2, which is fuel-vapor/air mixture, forms downstream of Zone 1. When the spray reaches the liquid length, the volume of Zone 1 stays constant until the end of fuel injection. On the other hand, Zone 2 continues to grow downstream as more fuel is injected until auto-ignition occurs. As stated by Dec (1997), the equivalence ratio in Zone 2 is in the range of 2 to 4 during feeding the standing premixed flame and the equivalence ratio is relatively uniform. Nevertheless, the local equivalence ratios can go up to 8 as shown by Espey et al. (1997). As described in the post-laser conceptual model section, the temperature in Zone 2 is around 825 K which is well beyond the auto-ignition temperature of diesel fuel (~500-550 K (Setchkin, 1954; International Programme on Chemical Safety, 1996)). Then, auto-ignition occurs in the premixed zone volumetrically. During the auto-ignition period, a fresh Zone 2 forms (which is called Zone 2'), holds the fuel vapor and air leaving Zone 1 and the air entrained from Zone 6. After the auto-ignition of the initial premixed zone, a standing premixed flame, which is Zone 3, appears between Zone 2' and products of the auto-ignition, Zone 4 (post Zone 2).

The fuel-rich combustion products of the premixed flame fill Zone 4. The temperature of this zone is around 1600-1800 K and there is not any oxygen left due to the rich-premixed flame (Zone 3). When the equivalence ratio is close to unity at the periphery of Zone 4, a diffusion flame surrounds Zone 4 and the distance from this flame to the injector nozzle is defined by the ***lift-off length*** as stated before. The diffusion flame that surrounds the jet periphery is Zone 5, and the surrounding cylinder gases constitute Zone 6. The spray jet continues to have all six zones in a quasi-steady form as shown in the last schematic of Figure 3.8.

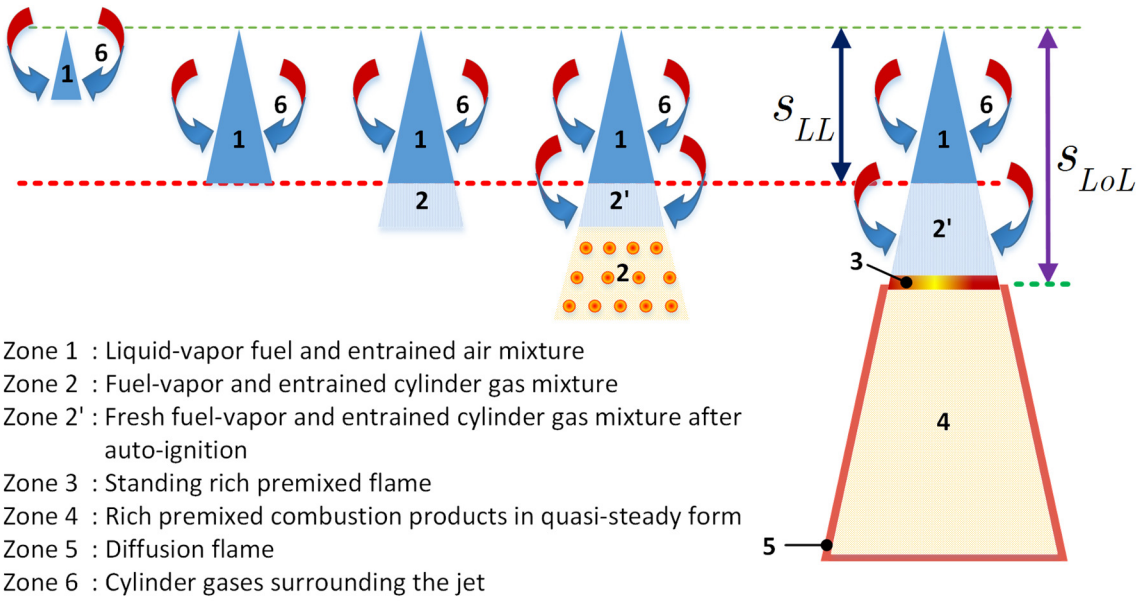

Figure 3.8 A temporal sequence of schematics showing how DI diesel combustion zones evolve from the SOI (Start of Injection) up through the early part of the mixing controlled burn.

The laser images of evolution of the spray jet after the end of injection are not clear due to the chaotic structure of the jet. The last portion of the liquid fuel will be assumed to penetrate further into the cylinder and the diffusion flame surrounds the whole jet as shown in the second schematic of Figure 3.9. The diffusion flame first moves from Zones 3 and 4 to Zone 1, then, evaporates liquid fuel and the liquid fuel mixes into Zone 2′. Similarly to the quasi-steady mixing controlled combustion, rich fuel-vapor/gas mixture goes through the standing premixed flame of Zone 3 and fills Zone 4 in order to oxidize in the diffusion flame, Zone 5. Eventually, the standing premixed flame is assumed to move upstream to the nozzle and consume the remaining fuel-vapor/gas mixture, leaving only combustion products, Zone 4, surrounded by the diffusion flame. A temporal

sequence of how combustion proceeds in DI diesel engines from the end of injection (**EoI**) to the end of combustion (**EoC**) is schematized in Figure 3.9.

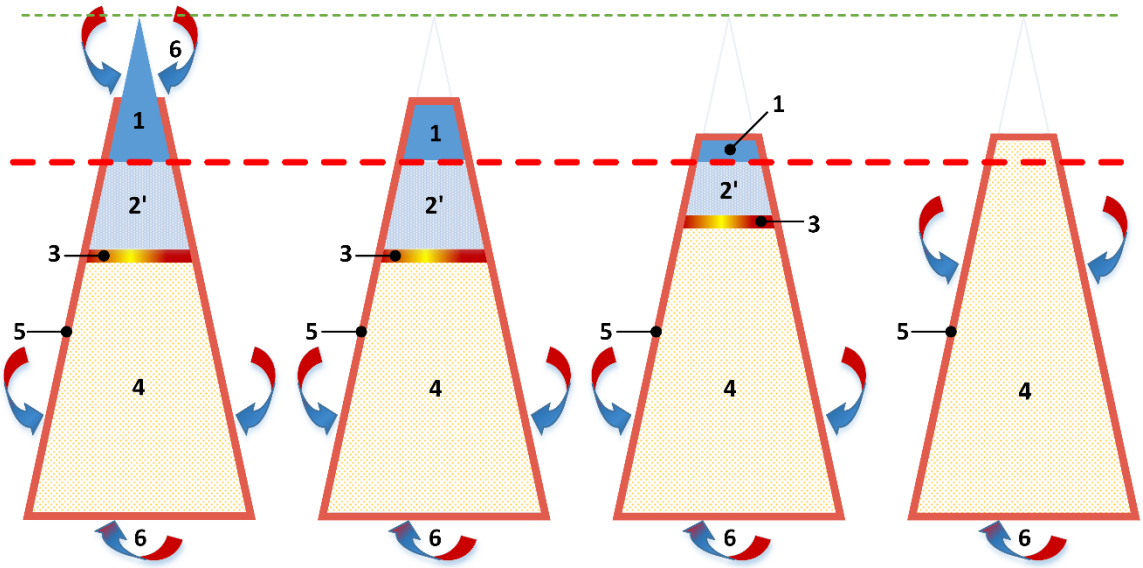

Figure 3.9 A temporal sequence of schematics showing how DI diesel combustion zones evolve from the early part of the mixing controlled burn up through the EoC (End of Combustion).

3.3.3 Governing Equations

In the following sub-sections the equations governing DI diesel engine combustion are given for 1) spray evolution and 2) zone thermodynamic states.

3.3.3.1 Spray Model

Naber and Siebers (1996) developed DI diesel fuel spray penetration correlations using constant-volume combustion vessel experiments for quiescent-type engine conditions. In their study; the effects of the injector parameters, fuel type, and in-cylinder thermodynamic conditions were considered. A quasi-steady

control volume analysis was presented by assuming 1) a uniform velocity profile at the injector exit plane, 2) a non-vaporizing, isothermal spray, 3) no-slip condition at the periphery (i.e. the fuel velocity is equal to the entrained gas velocity), and 4) a constant spray spreading angle. Experimental data obtained from constant-volume combustion vessel experiments over a wide range of DI diesel engine conditions (Naber and Siebers, 1996; Siebers, 1998) was correlated to non-vaporizing and non-reacting spray penetration data.

The penetration distance correlation developed by Naber and Siebers (1996) in non-dimensional form is given as

$$\tilde{t} = \frac{\tilde{s}}{2} + \frac{\tilde{s}}{4}\sqrt{1+16\tilde{s}^2} + \frac{\ln\left(4\tilde{s}+\sqrt{1+16\tilde{s}^2}\right)}{16} \tag{3.41}$$

where dimensionless penetration time, $\tilde{t}$, is a function of dimensionless penetration distance, $\tilde{s}$. The dimensionless penetration time and distance are defined as:

$$\tilde{t} = \frac{t}{t^*} \text{ and } \tilde{s} = \frac{s}{s^*} \tag{3.42}$$

The terms t and s are the penetration time and penetration distance and they are scaled with the penetration time scale t^* and characteristic length scale s^* defined as:

$$t^* = \frac{d_f\sqrt{\tilde{\rho}}}{U_f \tan\left(\alpha/2\right)} \tag{3.43}$$

$$s^* = \frac{d_f\sqrt{\tilde{\rho}}}{\tan\left(\alpha/2\right)} \tag{3.44}$$

The density ratio, $\tilde{\rho}$, is defined as the ratio of the fuel density ρ_f to the ambient gas density ρ_a:

$$\tilde{\rho} = \frac{\rho_f}{\rho_a} \tag{3.45}$$

Above, the effective nozzle diameter, d_f, can be calculated from the nozzle orifice diameter d_o by accounting for area contraction (i.e. the area contraction coefficient C_a):

$$d_f = \sqrt{C_a}d_o \tag{3.46}$$

The fuel velocity at the exit of the injector nozzle is derived from Bernoulli's principle as:

$$U_f = C_v\sqrt{2\frac{\left(P_f - P_a\right)}{\rho_f}} \tag{3.47}$$

and P_f is the fuel injector pressure and P_a is the ambient gas pressure. The velocity contraction coefficient C_v accounts for the head losses in the nozzle. The discharge coefficient of the injector orifice is the multiplication of the area contraction and velocity contraction coefficients.

$$C_d = C_aC_v \tag{3.48}$$

Naber and Siebers (1996) defined an inverse penetration distance relationship as a function of time that is accurate within 5% of the original time versus tip penetration distance equation, Eqn. (3.41)

$$\tilde{s} = \frac{\tilde{t}}{\left(1 + \tilde{t}^{n/2}\right)^{\frac{1}{n}}} \tag{3.49}$$

where n equals to 2.2. Therefore, the inverse relationship can be used as an initial guess for the iterative solution of Eqn. (3.41) for the penetration distance.

The "model" spray angle α in the penetration time and penetration distance scales, Eqns. (3.43) and (3.44), should be related to the "real" spray angle θ. An empirical relation was developed for the "real" spray angle by Siebers (1999, 2009)

$$\tan\left(\theta/2\right) = c_1\left(\left(\frac{\rho_a}{\rho_f}\right)^{0.19} - 0.0043\sqrt{\frac{\rho_f}{\rho_a}}\right) \tag{3.50}$$

Constant c_1 in Eqn. (3.50) is dependent upon the injector orifice with values reported over the range from 0.26 to 0.40 (Naber and Siebers, 1996; Siebers, 1999). The "model" spray angle α is related to the "real" spray angle θ by a constant (Naber and Siebers, 1996)

$$\tan\alpha = a\tan\theta \tag{3.51}$$

The constant a was recommended by Naber and Siebers (1996) as 0.66 initially, however, a new value of $a = 0.75$ was more recently recommended by Siebers *et*

al. (2002) due to improved measurements of the injector orifice area contraction coefficient.

The axial variation of the total ambient gas entrainment mass flow rate, $\dot{m}_a$, up to an axial location with respect to the amount of fuel injected, $\dot{m}_f$, can be expressed in non-dimensional form as (Naber and Siebers, 1996; Siebers, 1999):

$$\frac{\dot{m}_f}{\dot{m}_a} = \frac{2}{\sqrt{1+16\tilde{s}^2}-1} \tag{3.52}$$

The instantaneous injector fuel mass flow rate can be calculated using injector parameters:

$$\dot{m}_f = \rho_f A_f U_f = \dot{m}_f\left(s\right) \tag{3.53}$$

where A_f is the effective injector orifice area based on the effective injector diameter defined by Eqn. (3.46). The average axial velocity of the spray in any cross-section is,

$$\bar{U} = \frac{2U_f}{\sqrt{1+16\tilde{s}^2}+1} \tag{3.54}$$

Moreover, a cross-sectional average equivalence ratio can be expressed using Eqn. (3.52) (Naber and Siebers, 1996):

$$\bar{\phi} = \frac{2AF_s}{\sqrt{1+16\tilde{s}^2}-1} \tag{3.55}$$

where AF_s is the stoichiometric air/fuel ratio of the fuel.

Siebers (1999) developed the liquid phase dimensionless penetration length for an evaporating fuel spray:

$$\tilde{L} = 0.47\sqrt{\left(\frac{2}{B\left(T_a, P_a, T_f\right)} + 1\right)^2 - 1} \tag{3.56}$$

where $\tilde{L}$ is the normalized liquid length defined as

$$\tilde{L} = \frac{s_{LL}}{s^*} \tag{3.57}$$

The "specific energy ratio" *B* for single component fuels is given by:

$$B\left(T_a, P_a, T_f\right) = \frac{Z_a\left(T_s, P_a - P_s\right) P_s M_f}{Z_f\left(T_s, P_s\right)\left(P_a - P_s\right) M_a} = \frac{h_a\left(T_a, P_a\right) - h_a\left(T_s, P_a - P_s\right)}{h_f\left(T_s\right) - h_f\left(T_f, P_a\right)} \tag{3.58}$$

where the temperatures T_a, T_s, and T_f are the ambient gas temperature, fuel saturation temperature, fuel temperature at the exit of the injector, respectively. The pressure P_a is the ambient gas pressure, P_s is the fuel saturation pressure at the liquid length. The remaining terms Z_a and Z_f are the compressibility factors of the ambient gas and fuel vapor at the saturation temperature of the fuel; M_a and M_f are the molar mass of the ambient gas and fuel; and h_a and h_f are the specific enthalpies of the ambient gas and the fuel, respectively.

The specific energy ratio, *B*, is solved iteratively via Eqn. (3.58) by first solving for the saturation temperature at the liquid length, T_s, using the energy balance on the fuel jet and the equation of state. Then, the obtained value for *B* can be used with Eqns. (3.56), (3.57), and (3.44) to determine liquid length.

Siebers and coworkers (Siebers and Higgins, 2001; Siebers, Higgins and Pickett, 2002) developed a diffusion flame lift-off length correlation by using a #2 diesel fuel

$$s_{LoL} = c_I \frac{U_f d_o^{\,0.34}}{T_{gas}^{\,3.74} \rho_{gas}^{\,0.85} Z_{st}} \tag{3.59}$$

where s_{LoL} is the lift-off length in mm, c_I is a proportional constant (a value of $7.04 \cdot 10^8$ was used by (Pickett, Siebers and Idicheria, 2005), and $6 \cdot 10^6$ was used by (Xue and Caton, 2012) - $7.04 \cdot 10^8$ was used in this research), U_f is the injector exit velocity in m/s, d_o is the injector nozzle orifice diameter in μm, T_{gas} is the temperature of the surrounding gases in K, ρ_{gas} is the in-cylinder gas density in kg/m^3, and Z_{st} is the stoichiometric mixture fraction i.e. stoichiometric fuel mass divided by the total mass of mixture.

To sum up, the correlations expressed in this section define the spray geometry and necessary dimensional parameters in addition to the equivalence ratio as function of penetration distance.

3.3.3.2 Zone Governing Equations

The governing equations for each zone are presented in this subsection. The equations are presented for each orifice in a multi-hole injector. The total effect for the injector will be obtained simply by multiplying by the number of nozzles per injector. Then the total effect for the engine will be calculated simply by multiplying by the number of cylinders.

Zone 1: Liquid Fuel + Vapor Fuel + Entrained Air

The length of the liquid column from SOI up to the time at which the column reaches its maximum length will be calculated using Eqns. (3.41)-(3.49). The volume of this column will be that of a cone that is truncated at the small end by the orifice diameter, d_o. The angle of this truncated cone will be calculated using Eqns. (3.50) and (3.51).

The maximum, steady state liquid tip penetration will be calculated using Eqn. (3.56), where *B* expression is from Eqn. (3.58).

The continuity equation for the liquid column (Zone 1) is:

$$\frac{dm_1}{dt} = \dot{m}_{f,inj} + \dot{m}_{a_{6-1}} - \dot{m}_{f_{1-2}} - \dot{m}_{a_{1-2}} \tag{3.60}$$

where $\dot{m}_{f,inj}$ is the instantaneous fuel injection rate, $\dot{m}_{a_{6-1}}$ is the air entrainment rate to Zone 1 from Zone 6, $\dot{m}_{f_{1-2}}$ is the rate at which fuel is evaporated and transported into Zone 2 (Zone 2′ after auto-ignition), and $\dot{m}_{a_{1-2}}$ is the rate of the air mass entering Zone 2 from Zone 1 (all of the transient governing equations will

be integrated over a user-specified crank angle window). Until reaching the liquid length, no mass leaves Zone 1; therefore the last two terms of Eqn. (3.60) equal to zero during this period.

Liquid fuel evaporates at an increasing rate until it reaches its maximum length; when this liquid length is reached all of the fuel injected evaporates instantly. An evaporation curve for Zone 1 in the following form is assumed to simplify the analysis (a detailed evaporation model is available from several sources (Hiroyasu, Arai and Tabata, 1989; Hiroyasu and Arai, 1990; Jung and Assanis, 2001; Perini and Mattarelli, 2011)).

$$\chi = \frac{kx^*}{1 + k - x^*} \tag{3.61}$$

$$\left.\frac{dm_{f,vap}}{dt}\right|_1 = \chi \dot{m}_{f,\mathrm{inj}} \tag{3.62}$$

$$\left.\frac{dm_{f,\mathrm{liq}}}{dt}\right|_1 = \left(1 - \chi\right) \dot{m}_{f,\mathrm{inj}} \tag{3.63}$$

where χ is the evaporation fraction of the injected fuel mass in the time step, k is the calibration constant, and x^* is the ratio of the spray length to liquid length.

$$x^* = \frac{s}{s_{LL}} \tag{3.64}$$

When Zone 1 reaches liquid length, evaporation fraction becomes unity and the rate of change of fuel vapor and liquid fuel mass simplify to:

$$\left.\frac{dm_{f,vap}}{dt}\right|_1 = \dot{m}_{f,\text{inj}} - \dot{m}_{f_{1-2}} = 0$$
$$\left.\frac{dm_{f,\text{liq}}}{dt}\right|_1 = 0 \tag{3.65}$$

Once this steady state length has been attained, the continuity equation simplifies to the statement that the mass of fuel injected during the current crank angle window equals the mass of fuel vapor entering Zone 2. Similarly, the mass of the entrained air to Zone 1 equals to the mass of air entering Zone 2.

The First Law for Zone 1 is given by:

$$\frac{dH_1}{dt} = \dot{m}_{f,inj} h_{liq,T_{inj}} + \dot{m}_{a_{6-1}} h_{a,T_6} - \dot{m}_{f_{1-2}} h_{vap,T_{1g}} - \dot{m}_{a_{1-2}} h_{a,T_{1g}} \tag{3.66}$$

where the left hand side is the rate of change of total enthalpy in Zone 1, $h_{liq,T_{inj}}$ is the absolute enthalpy of the liquid fuel at the temperature indicated in the subscript, $h_{vap,T_{1g}}$ is the absolute enthalpy of the fuel vapor at the Zone 1 gas temperature, $h_{a,T_{1g}}$ is the absolute enthalpy of the air at the Zone 1 gas temperature, and the rate of heat transfer from Zone 1 to the cylinder walls is neglected.

The mass averaged gas temperature has to be found iteratively using the total enthalpy of Zone 1 and the gaseous mixture composition. Further, the liquid fuel temperature in Zone 1 is assumed to be constant and equal to the injected fuel temperature throughout the cycle.

The composition of the gaseous mixture in Zone 1 contains fuel-vapor and entrained air from Zone 6. The air composition of Zone 1 will not change until the

diffusion flame (Zone 5) surrounds the spray jet, then the air mass fraction of Zone 1 can be calculated from:

$$\left.\frac{dY_k}{dt}\right|_{1,a} = \frac{\dot{m}_{6-1}}{m_{1,a}}\left(Y_{k,6-1} - Y_k\Big|_{1,a}\right) \tag{3.67}$$

The gaseous composition of the Zone 1 at any given time is:

$$Y_k\Big|_{1,gas} = \frac{m_{1,vap}\, Y_k\Big|_{1,vap} + m_{1,a}\, Y_k\Big|_{1,a}}{m_{1,gas}} \tag{3.68}$$

Zone 1 after the End of Injection

After the end of injection, the volume of the liquid column will decrease as the height of the truncated cone decreases from the orifice end. The geometry of the cone shaped spray is shown in Figure 3.10. The volume of the liquid spray column at any cross section is

$$V_s = \frac{\pi}{3\tan\alpha}\left(r^3 - r_o^3\right) \tag{3.69}$$

where r is the radius at the instantaneous spray length, s, r_o is the radius of the nozzle injector, and α is the half angle of the spray.

The continuity equation for Zone 1 is given by

$$\frac{dm_1}{dt} = -\dot{m}_{f_{1-2'}} - \dot{m}_{a_{1-2'}} \tag{3.70}$$

The total mass leaving Zone 1 is assumed to be equal to the sum of the liquid mass injected and the entrained air mass in the last time step of the injection

period. The composition of Zone 1 during end of injection period is also assumed to be constant. Therefore, the rate of change of fuel vapor mass and the rate of air mass leaving Zone 1 are proportional to the fuel and air mass in the zone.

$$\dot{m}_{f_{1-2'}} = \frac{m_{f1}}{m_1}\dot{m}_{in}\Big|_{t=t_{EoI}} \tag{3.71}$$

$$\dot{m}_{a_{1-2'}} = \frac{m_{a1}}{m_1}\dot{m}_{in}\Big|_{t=t_{EoI}} \tag{3.72}$$

Correspondingly, the conservation of energy for Zone 1 is given by

$$\frac{dH_1}{dt} = -\dot{m}_{f_{1-2'}} h_{vap,T_{1g}} - \dot{m}_{a_{1-2'}} h_{a,T_{1g}} \tag{3.73}$$

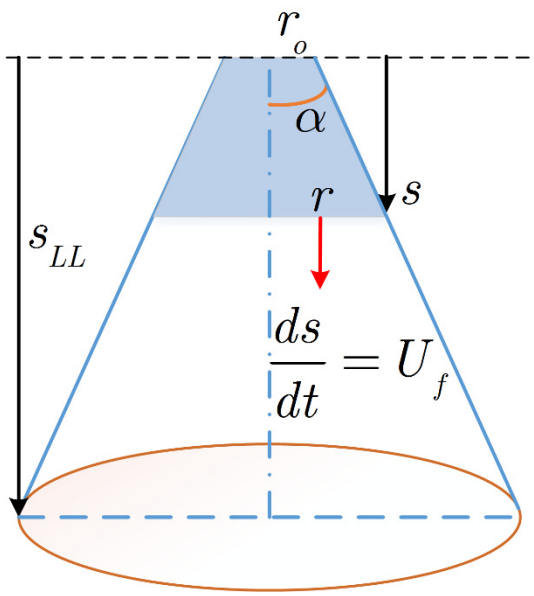

Figure 3.10 The geometry of the liquid cone

The mass averaged gas temperature of Zone 1 is found iteratively using the total enthalpy of Zone 1 and the gaseous mixture composition which is constant during the end of the injection period.

Zone 2: Fuel-vapor and Air Mixture

1) Up to the Ignition Delay:

Between the attainment of the maximum liquid length and the time of auto-ignition, the fuel vapor from the end of the liquid column will be mixing with the gases from Zone 6 as the entrainment rate given by Eqn. (3.52). The air entrainment rate from Zone 6 to Zone 1 will be subtracted from the total air entrainment rate from Zone 6 to the entire spray i.e. Zone 1 and Zone 2.

$$\dot{m}_{a_{6-2}} = \dot{m}_{a_{spray}} - \dot{m}_{a_{6-1}} \tag{3.74}$$

where $\dot{m}_{a_{spray}}$ is the total air entrainment rate up to the spray tip.

The continuity equation for Zone 2 for each injector orifice during the ignition delay period is:

$$\frac{dm_2}{dt} = \dot{m}_{1-2} + \dot{m}_{a_{6-2}} \tag{3.75}$$

where $\dot{m}_{1-2}$ is the fuel-vapor and air mixture exiting through the liquid length cross-section from Zone 1 and entering into Zone 2 during the ignition delay.

$$\dot{m}_{1-2} = \dot{m}_{f,inj} + \dot{m}_{a_{6-1}} \tag{3.76}$$

Once Zone 1 reaches to the liquid length, the mass flow rate of fuel vapor leaving Zone 1 equals the injector mass flow rate.

The First Law for each injector orifice for Zone 2 during the ignition delay period is:

$$\frac{dH_2}{dt} = \dot{m}_{f_{1-2}} h_{vap,T_{1g}} + \dot{m}_{a_{1-2}} h_{a,T_{1g}} + \dot{m}_{a_{6-2}} h_{a,T_6} \tag{3.77}$$

where the left hand side is the rate of change of total enthalpy of Zone 2, $h_{\mathrm{vap},T_{1g}}$ is the absolute enthalpy of the fuel-vapor at the gas temperature of Zone 1, $h_{a,T_{1g}}$ is the absolute enthalpy of the air at the Zone 1 gas temperature, and the rate of heat transfer from Zone 2 to the cylinder walls is neglected.

Similar to Zone 1, the mass averaged gas temperature has to be found iteratively using the total enthalpy of Zone 2 and the gaseous mixture composition.

$$\left.\frac{dY_k}{dt}\right|_2 = \sum_{in} \frac{\dot{m}_{in}}{m_2} \left(Y_{k,in} - Y_k \big|_2 \right) \tag{3.78}$$

2) The Ignition Delay:

The ignition delay can be simulated a variety of ways depending upon the criteria used to determine the start of combustion (Kuo, 2005). Assanis *et al.* (2003) present the following empirical formula for the ignition delay in DI diesels under steady-state and transient operation based on Watson *et al.*'s correlation (1980) by adding an equivalence ratio dependence:

$$\tau_{ID} = 2.4\phi^{-0.2} P^{-1.02} \exp\left(\frac{E_a}{R_u T}\right) \tag{3.79}$$

where τ_{ID} is the ignition delay in ms, is the overall equivalence ratio, P is the cylinder pressure in bar, T is the cylinder bulk temperature in K, E_a is the global activation energy for the auto-ignition reactions in kJ/kmole, and R_u is the universal gas constant. For No. 2 diesel fuel mixed with air, Watson et al. (1980) suggest $E_a \big/ R_u = 2100$.

The ignition delay is calculated every time step starting with SOI using the instantaneous values of the cylinder pressure and temperature until auto-ignition occurs. The following constraint accounts for the transient effects on the properties of the cylinder contents (Livengood and Wu, 1955):

$$\int_{t_{SOI}}^{t_{ID}} \frac{dt}{\tau_{ID}\left(t\right)} = 1 \tag{3.80}$$

This empirical model has shown good agreement with experimental data for DI diesel engines over a wide range of operating conditions.

3) Auto-ignition

Higgins *et al.* (2000) researched the evolution of the auto-ignition of a DI diesel spray under no swirl conditions. It is observed that chemiluminescence occurs uniformly between the liquid length and the tip of the spray. The uniform character of ignition downstream of the liquid length indicates a homogenous mixture in this region. Miles (2000) investigated the influence of swirl on direct-

injection diesel combustion at moderate speed and load. The cylinder pressure traces obtained from different levels of swirl showed longer ignition delay times for the lower swirl ratios. However, during the auto-ignition period cylinder pressure traces followed similar slope and reached a similar maximum pressure at the end of auto-ignition for all the swirl levels. Therefore; in the auto-ignition period, Zone 2 is considered to behave like an adiabatic homogenous cylinder-piston system that reacts volumetrically without a strong effect of turbulence and the products of combustion mix with the unburned composition until all of the available oxygen is consumed (Figure 3.11). Hence, a single temperature and species concentration suffice to describe the evolution of Zone 2 during the auto-ignition period.

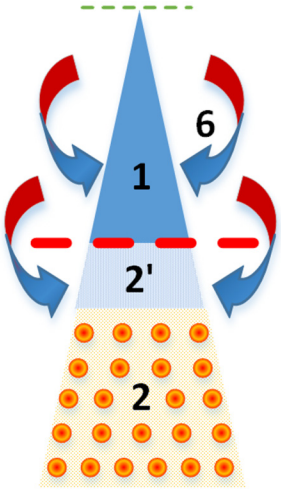

Figure 3.11 Auto-ignition occurs uniformly within Zone 2.

A one-step global reaction with unburned mass fraction dependence is assumed to define the rate of mass burning:

$$\dot{m}_{b_2} = A\rho_2^2\psi^2\left(\frac{Y_{O_2}}{Y_{O_2}+Y_F}\right)\exp\left(-\frac{E_a}{R_uT_2}\right)V_2 \qquad (3.81)$$

including a frequency factor A, Zone 2 mixture density ρ_2, unburned oxygen mass fraction ψ, mass fraction of oxygen Y_{O_2}, mass fraction of fuel Y_F, activation energy E_a, universal gas constant R_u, Zone 2 mixture temperature T_2, and Zone 2 volume V_2. The frequency factor and the activation temperature are assumed to be $A = 5 \times 10^{10}\, m^3 \big/ kg \cdot s$ (Nishida and Hiroyasu, 1989) and $E_a \big/ R_u = 15098K$ (Westbrook and Dryer, 1984) respectively in this research. The unburned oxygen mass fraction is defined as the ratio of the available oxygen to the mass of the oxygen at the beginning of the auto-ignition period:

$$\psi = \frac{m_{O_2}\left(t\right)}{m_{O_2}\Big|_{t=t_{ID}}} \tag{3.82}$$

The mass burning in a time step is equilibrated at constant enthalpy and pressure then mixed with the remaining contents of Zone 2. Moon *et al.* (2010) investigated gas entrainment characteristics of diesel sprays using laser imaging (LIF-PIV technique). The entrained gas velocity images suggest the air entrainment to the leading portion is negligible. Therefore, Zone 2 becomes a fixed mass system during auto-ignition.

$$\frac{dm_2}{dt} = 0 \tag{3.83}$$

The First Law for each injector orifice for Zone 2 during the auto-ignition period is:

$$\frac{dH_2}{dt} = 0 \tag{3.84}$$

The mass averaged gas temperature has to be found iteratively using the total enthalpy of Zone 2 and the gaseous mixture composition:

$$Y_k\Big|_2 = \frac{\left(m_2 - m_{b_2}\right)Y_k\Big|_2 + m_{b_2}\,Y_k\Big|_{eq}}{m_2} \tag{3.85}$$

The auto-ignition period ends when there is no more oxygen available within Zone 2. Following auto-ignition, the jet enters a quasi-steady state. Zone 2 is renamed Zone 4 when the auto-ignition period ends in order to emphasize the zone location and its role in feeding the diffusion flame.

Zone 2′: Formation of Fresh Fuel-vapor Air Mixture after Auto-ignition

A fresh Zone 2, which is renamed Zone 2′, forms during the auto-ignition period of Zone 2. Zone 2′ shows the same behavior as Zone 2 except it does not auto-ignite and after the auto-ignition period, Zone 2′ feeds the standing premixed flame (Zone 3) which, in turn, feeds Zone 4.

The conservation of mass for Zone 2′ can be written as:

$$\frac{dm_{2'}}{dt} = \dot{m}_{1-2'} + \dot{m}_{a_{6-2'}} - \dot{m}_{f_{2'-3}} - \dot{m}_{a_{2'-3}} \tag{3.86}$$

where $\dot{m}_{1-2'}$ is the rate of the fuel-vapor and air mixture exiting through the liquid length cross-section from Zone 1 and entering Zone 2′, $\dot{m}_{a_{6-2'}}$ is the rate of air mass entrainment to Zone 2′ from Zone 6, $\dot{m}_{f_{2'-3}}$ is the rate of fuel-vapor mass that is

feeding the standing premixed flame that onsets at the end of the auto-ignition period of Zone 2, and $\dot{m}_{a_{2'-3}}$ is the rate of the air mass feeding the standing premixed flame.

The lift-off length defined in Eqn. (3.59) controls the air mass flow rate entrainment to Zone 2′ when a diffusion flame envelopes the jet after auto-ignition. Prior to onset of the diffusion flame, the air entrainment rate to Zone 2′ is calculated similar to Zone 2. The corresponding rate of mass flows during the spray evolution are:

1) Auto-ignition Period

$$\dot{m}_{1-2'} = \dot{m}_{f,inj} + \dot{m}_{a_{6-1}} \tag{3.87}$$

$$\dot{m}_{a_{6-2'}} = \dot{m}_{a_{6-S}}\Big|_{s_{2'}} - \dot{m}_{a_{6-1}} \tag{3.88}$$

where $\dot{m}_{a_{6-S}}\Big|_{s_{2'}}$ is the total air entrainment from Zone 6 to the spray section that is $s_{2'}$ long. The length of spray from the tip of the injector up to the end of Zone 2′ is $s_{2'}$. The Zone 2′ penetration time is set to the time when Zone 1 reaches the liquid length. When Zone 2′ onsets, the rate of air mass flow entrainment can be calculated by Eqns. (3.41)-(3.52).

Zone 3 forms between Zone 2′ and Zone 2 (called Zone 4 after auto-ignition) when the auto-ignition period ends; therefore, the mass flow rates to Zone 3 are zero during the auto-ignition period.

$$\begin{aligned} \dot{m}_{f_{2'-3}} &= 0 \\ \dot{m}_{a_{2'-3}} &= 0 \end{aligned} \tag{3.89}$$

2) Quasi-steady Period

In the quasi-steady period, Zone 2′ interacts with Zone 1, Zone 3, Zone 5, and Zone 6. The lift-off length controls the rate of air entrainment to Zone 2′ from Zone 6 and the volume of Zone 2′ is fixed in this period between the liquid length and the standing premixed flame. Therefore, there is no mass accumulation or depletion within Zone 2′ during the quasi-steady period. The corresponding rate of mass flows of fuel-vapor and air can be calculated as:

$$\frac{dm_{2'}}{dt} = 0 \tag{3.90}$$

$$\dot{m}_{1-2'} = \dot{m}_{f,inj} + \dot{m}_{a_{6-1}} \tag{3.91}$$

$$\dot{m}_{a_{6-2'}} = \dot{m}_{a_{spray}}\Big|_{s_{2'}} - \dot{m}_{a_{6-1}} \tag{3.92}$$

$$\dot{m}_{f_{2'-3}} = \dot{m}_{f,inj} \tag{3.93}$$

$$\dot{m}_{a_{2'-3}} = \left(\dot{m}_{a_{spray}}\Big|_{s_{2'}} - \dot{m}_{a_{6-1}} \right) + \dot{m}_{a_{6-1}} = \dot{m}_{a_{spray}}\Big|_{s_{2'}} \tag{3.94}$$

When the lift-off length is shorter than the distance from the injector to the standing premixed flame location, s_3 (Zone 3), the diffusion flame prevents air entrainment. The rate of air entrainment in this case can be calculated by Eqn. (3.52) by updating the dimensionless penetration distance, $\tilde{s}$.

$$\tilde{s} = \frac{s_{LoL}}{s^*} \tag{3.95}$$

3) End of Injection Period

When the injection ends, Zone 1 shrinks and fuel-vapor and air mixture continues to enter as described in the quasi-steady period. The quasi-steady equations are still valid until Zone 1 does not hold any mass. The rate of mass that evaporates within Zone 1 in this period is assumed to be proportional to the sum of last rate of fuel mass injected and air entrained, Eqn. (3.71), and this is constant until all the liquid fuel has evaporated. Moreover, in this period there is no more air entrainment from Zone 6 to either Zone 1 or Zone 2' since the diffusion flame envelopes all the jet when the injection ends. Similar to the fuel evaporation rate, the rate of air mass flow from Zone 1 to Zone 2' is assumed to be proportional to the sum of the last rate of liquid fuel injection and the rate of air entrainment mass flow to Zone 1 from Zone 6 and given by Eqn. (3.72).

a) When Zone 1 Exists

$$\frac{dm_{2'}}{dt} = 0 \tag{3.96}$$

$$\dot{m}_{1-2'} = \dot{m}_{f_{1-2'}} + \dot{m}_{a_{1-2'}} \tag{3.97}$$

$$\dot{m}_{f_{1-2'}} = \frac{m_{f1}}{m_1}\dot{m}_{in}\Big|_{t=t_{EoI}} \tag{3.98}$$

$$\dot{m}_{a_{1-2'}} = \frac{m_{a1}}{m_1}\dot{m}_{in}\Big|_{t=t_{EoI}} \tag{3.99}$$

$$\dot{m}_{a_{6-2'}} = 0 \tag{3.100}$$

$$\dot{m}_{f_{2'-3}} = \dot{m}_{f_{1-2'}} \tag{3.101}$$

$$\dot{m}_{a_{2'-3}} = \dot{m}_{a_{1-2'}} \tag{3.102}$$

b) When Zone 1 Does not Exist

Zone 2′ is the next to shrink and deplete after Zone 1. Similar to Zone 1, the rate of fuel vapor mass leaving Zone 2′ and feeding the standing premixed flame is assumed to be proportional to the sum of the last injected fuel mass rate and the last entrained air mass rate again the rate of air mass leaving from Zone 2′ to Zone 3 is proportional to the amount of the last total mass entrained to Zone 1 from injector and Zone 6.

$$\dot{m}_{1-2'} = 0 \tag{3.103}$$

$$\dot{m}_{a_{6-2'}} = 0 \tag{3.104}$$

$$\dot{m}_{a_{2'-3}} = \frac{\dot{m}_{in}\Big|_{t=t_{EoI}}}{1+\phi_{2'}FA_s} \tag{3.105}$$

$$\dot{m}_{f_{2'-3}} = \dot{m}_{in}\Big|_{t=t_{EoI}} - \dot{m}_{a_{2'-3}} \tag{3.106}$$

$$\dot{m}_{2'-3} = \dot{m}_{a_{2'-3}} + \dot{m}_{f_{2'-3}} \tag{3.107}$$

The First Law for each injector orifice for Zone 2′ is:

$$\frac{dH_{2'}}{dt} = \dot{m}_{f_{1-2'}}h_{vap,T_{1g}} + \dot{m}_{a_{1-2'}}h_{a,T_{1g}} + \dot{m}_{a_{6-2'}}h_{a,T_6} - \dot{m}_{f_{2'-3}}h_{vap,T_{2'}} - \dot{m}_{a_{2'-3}}h_{a,T_{2'}} \tag{3.108}$$

The corresponding rate of mass flows presented for the auto-ignition, quasi-steady, and end of injection periods. The mass averaged gas temperature has to be found iteratively using the total enthalpy of Zone 2′ and the gaseous mixture composition.

$$\left.\frac{dY_k}{dt}\right|_{2'} = \sum_{in} \frac{\dot{m}_{in}}{m_{2'}} \left(Y_{k,in} - Y_k \big|_{2'} \right) \tag{3.109}$$

Zone 3: Formation of a Standing Premixed Flame

Once the mixture in Zone 2 has been auto-ignited, Zone 2 will be instantly transformed into the "feed stream" for the diffusion flame (Zone 5) and Zone 2, renamed Zone 4 after the auto-ignition period, (Figure 3.8). Zone 3 is located between the downstream end of Zone 2′ and the upstream end of Zone 4. The equivalence ratio for the standing premixed flame equals to the equivalence ratio of Zone 2′. The rate of fuel-vapor mass and the rate of air entrainment mass to Zone 2′ controls the composition that is feeding to the premixed flame. There is no accumulation or depletion of mass within Zone 3. The mass entering the premixed flame equilibrates at constant specific enthalpy and pressure, then the equilibrium products enter to the zone downstream of the flame which is Zone 4. A freeware software, Cantera (Goodwin *et al.*, 2014), is used to find the equilibrium composition of the products in Zone 3. Cantera's equilibrium solver is based on the element potential method (Powell and Sarner, 1959) and uses a damped Newton method to solve these equations. Further details of the formulation and algorithm can be found in Smith and Missen (1982).

Zone 4: Auto-ignition and Standing Premixed Flame Products

The rich products from the standing premixed flame (Zone 3) are the source for a gaseous jet (Zone 4, called Zone 2 during the auto-ignition period) issuing into Zone 6. At the end of the auto-ignition period, the diffusion flame envelopes Zone 4 and the jet transforms to the quasi-steady period. The diffusion flame

surface, which is Zone 5, exists where the equivalence ratio equals to unity. The continuity equation for Zone 4 for each injector orifice is:

$$\frac{dm_4}{dt} = \dot{m}_{3-4} - \dot{m}_{4-5} \tag{3.110}$$

The mass entrainment rate from the standing premixed flame (Zone 3) into Zone 4 is given in the Zone 2′ description; Eqns. (3.93) and (3.94) for the quasi-steady period, and Eqns. (3.101) and (3.102) for the end of injection period until Zone 2′ is consumed. The rate of mass flow from Zone 4 to the diffusion flame will be explained in the governing equations for Zone 5 below.

The First Law for each injector orifice for Zone 4 is:

$$\frac{dH_4}{dt} = \dot{m}_{3-4} h_{T_3} - \dot{m}_{4-5} h_{T_4} \tag{3.111}$$

Again, the mass averaged gas temperature has to be found iteratively using the total enthalpy of Zone 4 and the gaseous mixture composition.

$$\left.\frac{dY_k}{dt}\right|_4 = \sum_{in} \frac{\dot{m}_{in}}{m_4} \left(Y_{k,in} - Y_k \big|_4 \right) \tag{3.112}$$

Zone 5: Diffusion Flame

The diffusion flame onsets at the end of the auto-ignition period. Zone 4 feeds "fuel" from inside of the gas jet while Zone 6 is supplying necessary oxygen from outside of the jet for the diffusion flame. The combustion products formed at the diffusion flame surface are assumed to diffuse only into Zone 6. The

turbulence level within the cylinder affects the rate of combustion of the diffusion flame significantly and this effect shows itself in the cylinder pressure traces (Miles, 2000). A turbulence model will be used to represent the in-cylinder motion effect on the diffusion combustion rate.

There is no mass existing within Zone 5 (which is infinitesimally thin); therefore, the continuity equation for each injector is:

$$\frac{dm_5}{dt} = \dot{m}_{4-5} + \dot{m}_{6-5} - \dot{m}_{b_5} = 0 \tag{3.113}$$

where $\dot{m}_{b_5}$ is the rate of mass burn within Zone 5. The rate of mass that is feeding the diffusion flame from Zone 4, $\dot{m}_{4-5}$, is determined by a mixing controlled combustion model. A mixing frequency model of Boulouchos and Eberle (1991), incorporated by Barba *et al.* (2000) in a single-zone model of DI diesel engines, will be used for the present quasi-dimensional model. The mixing frequency determined by the turbulence model controls the mass of the "fuel" entrainment from Zone 4:

$$\dot{m}_{4-5} = f_m m_4 \tag{3.114}$$

The mixing frequency is given by the following relation:

$$f_m = C_{diff} \frac{\sqrt{c_G \overline{S}_p^2 + c_k \frac{k}{\frac{3}{2}m}}}{\sqrt[3]{\phi \frac{V}{n_N}}} \tag{3.115}$$

where C_{diff}, (Barba *et al.* (2000) reported 1.8 to 3 for the three engines evaluated), and c_k (differs in the range from 0.1 to 0.4 (Barba *et al.*, 2000)) are constants, $\overline{S}_p$ is the mean piston speed, k is the turbulent kinetic energy, m is the cylinder mass, ϕ is the overall equivalence ratio, V is the cylinder volume, and n_N is the number injector nozzles. The $c_G \overline{S}_p^2$ term is the mean mixing velocity due to bulk cylinder motion while $2c_k k \big/ 3m$ is the mean mixing velocity due to turbulence within the cylinder.

The $k-\varepsilon$ turbulence model is preferred in this research due to its simple nature and computationally fast solution. Assanis *et al.* (1985) presented a detailed description of this model for the engine application and will be summarized here for completeness.

The energy cascade model is based on the mean flow kinetic energy, K, entering the cylinder through the intake valves and conversion of this kinetic energy to the turbulent kinetic energy, k, through turbulent dissipation. Viscous dissipation converts turbulent kinetic energy to heat. When mass is lost through the exhaust valves or blow by, both the mean flow and turbulent kinetic energy are lost as well.

The rate of change of mean flow kinetic energy is:

$$\frac{dK}{dt} = \frac{1}{2}\dot{m}_i V_i^2 - \mathrm{P} - K\frac{\dot{m}_e}{m} \tag{3.116}$$

where the first term is the kinetic energy entering the cylinder through the intake valves and the injector, the second term is the rate of turbulent kinetic energy

production, and the third term is the energy carried out with the exiting mass from cylinder.

The rate of change of turbulent kinetic energy is:

$$\frac{dk}{dt} = \mathrm{P} - m\varepsilon - k\frac{\dot{m}_e}{m} + A \tag{3.117}$$

where the second term is the rate of turbulent kinetic energy dissipation, the third term is the rate of turbulent kinetic energy carried away by the exiting mass, and the last term is the rate of turbulent kinetic energy amplification due to rapid distortion.

Turbulence production within cylinder, which can be estimated by:

$$\mathrm{P} = 0.3307 C_\beta \left(\frac{K}{l}\right)\sqrt{\frac{k}{m}} \tag{3.118}$$

where C_β is an adjustable constant set to be 1 in this study, and l is the characteristic length defined as the ratio of the instantaneous cylinder volume to the cylinder cross-sectional area:

$$l = \frac{V}{\pi\dfrac{B^2}{4}} \tag{3.119}$$

If the characteristic length is larger than half of the cylinder bore, then the characteristic length is equal to half of the cylinder bore.

The rate of turbulent kinetic energy dissipation per unit mass is given as:

$$\varepsilon = \frac{\left(\frac{2k}{3m}\right)^{3/2}}{l} \tag{3.120}$$

The rate of turbulent kinetic energy amplification due to rapid distortion is given by:

$$A = \frac{2}{3} k \frac{\dot{\rho}}{\rho} \tag{3.121}$$

An initial estimate of the mean flow kinetic energy at intake valve closure (**IVC**) is given by (Heywood, 1988):

$$K_{IVC} = \frac{1}{16} m \left(B R_s w \right)^2 \tag{3.122}$$

where B is the bore of the cylinder in meters, R_s is the swirl ratio, and w is the engine speed in rad/s. An initial estimate of turbulent kinetic energy is given by Grasso and Bracco (1983):

$$k_{IVC} = \alpha m_{IVC} \left(\eta_v N \right)^2 \tag{3.123}$$

where $\alpha = 0.61 \times 10^{-4}$, m_{IVC} is the cylinder total mass at IVC, η_v is the volumetric efficiency, and N is the engine speed in rpm. The mean flow and turbulent kinetic energies are in units of J when given units are used.

The rate of air entrainment from Zone 6 to Zone 5 is found iteratively once the rate of "fuel" consumption is determined by Eqns. (3.114) - (3.123). The goal of the iterations is to maximize the equilibrium temperature at constant enthalpy

and pressure since the diffusion flame assumed to be at the adiabatic flame temperature.

Zone 6: Cylinder Gas (air + EGR) Surrounding the Spray Jet

The surrounding gas will be treated as an isothermal core, as the unburned zone in a spark ignition engine is modeled. The temperature of Zone 6 will vary with piston motion, energy release in the other zones, and heat losses. The continuity equation for Zone 6 for each injector orifice is:

$$\frac{dm_6}{dt} = -\sum_{i=1}^{5} \dot{m}_{a_{6-i}} + \dot{m}_{5-6} - \dot{m}_{RP} \tag{3.124}$$

where $\dot{m}_{RP}$ is the mass flow into the ring pack (or out of the ring pack if the pressure gradient is favorable), as explained in Section 3.2.2.

The First Law for each injector orifice for Zone 6 is calculated using the energy balance of the wedge (the cylinder volume is divided into wedges for each injector orifice) and existing zones:

$$\frac{dU_w}{dt} = \dot{m}_{f,inj} h_{liq,T_{inj}} - \dot{m}_{RP} h_{T_6} - P\frac{dV}{dt} - \dot{Q}_{ht} \tag{3.125}$$

$$U_6 = U_w - \sum_{i=1}^{5} U_i \tag{3.126}$$

The mass averaged gas temperature has to be found iteratively using the total internal energy of Zone 6 and the gaseous mixture composition. It is assumed that the ring pack has the same composition as Zone 6; therefore, the species equation simplifies to:

$$\left.\frac{dY_k}{dt}\right|_6 = \frac{\dot{m}_{5-6}}{m_6}\left(Y_{k,5_{eq}} - Y_k\Big|_6\right) \tag{3.127}$$

The cylinder pressure is the same in all zones; hence, it is calculated using all of the cylinder contents in the gas phase. In order to simplify the calculations, all the gaseous cylinder contents are grouped and named Zone 0.

Zone 0: All of the Cylinder Fluid in the Gas Phase

The mass of gas phase cylinder fluid can be found by subtracting the liquid fuel mass from the mass of the wedge mass:

$$m_0 = m_w - m_{liq} \tag{3.128}$$

Similarly, the total internal energy of Zone 0 is calculated by subtracting the liquid fuel total energy from the total energy of the wedge.

$$U_0 = U_w - U_{liq} \tag{3.129}$$

The cylinder pressure has to be found iteratively using the total internal energy of Zone 0, the density of Zone 0, and the gaseous mixture composition.

$$Y_k\Big|_0 = \frac{\sum_{i=1}^{6} m_{i,gas}\, Y_k\Big|_{i,gas}}{m_0} \tag{3.130}$$

3.4 Expansion Process

The expansion process starts at the end of combustion (EoC) and ends at exhaust valve opening (EVO). Similarly to the compression process, although the expansion stroke normally begins before EoC and ends after EVO, here the expansion "process" refers to the portion of the expansion stroke during which the cylinder is essentially a fixed mass system, except for the minor change in trapped mass due to flow leaving the combustion chamber into the piston ring pack. Therefore, the overall cylinder mass conservation equation will be the same as that for the compression process, Eqn. (3.15), including the same equation set for the ring pack flow, Eqns. (3.25)-(3.33).

Continued reaction will not be allowed after the end of combustion, but the return flow out of the ring pack will be accounted for in the species conservation equation, and will be the same as that during the compression process, Eqn. (3.16) . The energy conservation equation for the expansion process is also the same as that used for the compression process, Eqn. (3.17).

The heat loss model used for the compression process, discussed earlier, will also be used for the expansion process, Eqns. (3.34)-(3.36).

Set of Governing Equations

The final set of governing equations for the expansion process consists of Eqns. (3.15)-(3.36), creating a set of nine nonlinear, ordinary differential equations. The state variables are

$$\left\{ m, Y_k, T, P, P_2, P_3, P_4, P_5, P_6 \right\} \tag{3.131}$$

3.5 Gas Exchange Process

This section deals with the governing equations for the intake and exhaust processes adopted from Watson and Janota's work (1982). The gas exchange process starts with the beginning of exhaust valve opening (EVO) and ends at intake valve closing (IVC). Moreover, the processes occurring during gas exchange can be divided into exhaust, valve overlap, and inlet periods. These periods will be considered separately and sub-divided based on the flow direction. The governing equations for the intake and exhaust processes are summarized at the end of this section.

3.5.1 Exhaust Period (EVO to IVO)

The exhaust period starts from exhaust valve opening (EVO) and ends at intake valve opening (IVO). During this period, combustion products flow into the exhaust manifold. However, depending upon the pressure difference between cylinder pressure and the exhaust manifold pressure, a reverse flow may be induced.

a) Normal flow, cylinder to exhaust manifold, $P_{cyl} > P_{exh}$

It is assumed that the flow through a valve is quasi-steady, one-dimensional orifice flow. In practice, this flow is highly unsteady and three-dimensional. Consequently, a discharge coefficient, C_d is adopted to overcome non-ideal effects. Moreover, the valve throat pressure will not be known; therefore, it is assumed that no diffusion occurs between the valve throat and the downstream (i.e. exhaust

valve port) due to the turbulence; i.e., $P_{throat} \approx P_{manifold}$. As the valve opens, the pressure ratio across the valve will decide if the flow is choked or not. Consequently, the mass flow rate through the valve can be expressed as

$$\dot{m}_{valve} = \begin{cases} C_d A_{flow} P_u \sqrt{\left\{ \left(\frac{2\gamma}{\gamma - 1} \right) \frac{1}{RT_u} \left[\left(\frac{P_d}{P_u} \right)^{\frac{2}{\gamma}} - \left(\frac{P_d}{P_u} \right)^{\frac{\gamma+1}{\gamma}} \right] \right\}} & \frac{P_d}{P_u} > \left(\frac{2}{\gamma+1} \right)^{\frac{\gamma}{\gamma-1}} \\ C_d A_{flow} P_u \sqrt{\frac{\gamma}{RT_u} \left(\frac{2}{\gamma+1} \right)^{\frac{\gamma+1}{2(\gamma-1)}}} & \frac{P_d}{P_u} \leq \left(\frac{2}{\gamma+1} \right)^{\frac{\gamma}{\gamma-1}} \end{cases}$$

(3.132)

where A_{flow} is the reference area of the valve that the discharge coefficient is based on, subscript u represents upstream flow, and subscript d represents downstream flow. In this case the upstream side is the cylinder and the downstream side is the exhaust port. In practice, the discharge coefficient for flow across the valve is measured using a flow bench during which the valve lift is slowly varied and the flow is measured for fixed upstream and downstream pressures. The discharge coefficient is then calculated as a function of valve lift. Usually, for the flow across the exhaust valves the minimum area available for the flow is selected as reference area. As the exhaust valve opens, the restricting area is the valve "curtain" area. This is the area of a right circular cylinder between the valve and the valve seat. Once the valve is sufficiently open, the area that restricts the flow is the effective area of the port: the cross sectional area of the port normal to the flow minus the cross sectional area of the valve stem.

Therefore, the overall cylinder mass conservation equation can be written as

$$\frac{dm}{dt} = -\dot{m}_{exh} - \dot{m}_{RP} \tag{3.133}$$

where $\dot{m}_{RP}$ is the mass flow into the ring pack (or out of the ring pack if the pressure gradient is favorable).

b) Reverse flow, exhaust manifold to cylinder, $P_{exh} > P_{cyl}$

In this case upstream is the exhaust manifold and downstream is the cylinder volume. Therefore, the overall cylinder mass conservation equation becomes

$$\frac{dm}{dt} = \dot{m}_{exh} - \dot{m}_{RP} \tag{3.134}$$

Enthalpy, species mass fractions, and temperature in the exhaust manifold are assumed to be known. Consequently, a separate sub-model for the manifolds will not be included.

3.5.2 Valve Overlap Period (IVO to EVC)

The valve overlap period of a reciprocating engine is when both the intake and exhaust valves are open at the same time. Valve overlap increases engine volumetric efficiency by allowing the momentum of the exhaust gases leaving the cylinder to suck fresh charge into the cylinder. During this period there are three possible flow directions depending upon the pressures in the intake manifold, cylinder volume, and exhaust manifold. Each of the three possible situations is discussed in the following subsections.

a) Normal scavenging, $P_{int} > P_{cyl} > P_{exh}$

It is assumed that the intake valve and the exhaust manifold pressures, temperatures and species mass fractions are known. Moreover, the cylinder volume content is treated to be homogenous by assuming complete mixing of the intake gases. The mass flow rates across the intake and exhaust valves are calculated from Eqn. (3.132). For the intake mass flow rate: upstream pressure is the intake manifold pressure and downstream pressure is the cylinder pressure. On the other hand, for the exhaust mass flow rate, the upstream pressure is cylinder pressure and downstream pressure is the exhaust manifold pressure. Consequently, mass conservation is

$$\frac{dm}{dt} = \dot{m}_{int} - \dot{m}_{exh} - \dot{m}_{RP} \tag{3.135}$$

b) Reverse flow into the cylinder, $P_{int} > P_{cyl} < P_{exh}$

If this pressure distribution occurs, during this period the rate of change of cylinder mass is the sum of the intake and exhaust mass flow rates minus the mass lost due to flow into the ring pack (if any). The upstream and downstream pressures are assigned (which is upstream and which is downstream) based on flow direction as discussed earlier in this section.

$$\frac{dm}{dt} = \dot{m}_{int} + \dot{m}_{exh} - \dot{m}_{RP} \tag{3.136}$$

c) Reverse flow into the intake manifold, $P_{exh} > P_{cyl} > P_{int}$

If this pressure distribution occurs, during this period mass flows from the exhaust port to the cylinder and from the cylinder volume to the intake port.

$$\frac{dm}{dt} = \dot{m}_{exh} - \dot{m}_{int} - \dot{m}_{RP} \tag{3.137}$$

3.5.3 Intake Period (EVC to IVC)

Only the intake valve is open during this period and a fresh charge of air with exhaust recirculation gases fill the cylinder volume. Even for turbocharged engines, the pressure in the intake port (assumed, as usual, equal to the pressure in the intake manifold) is not sufficiently higher than the cylinder pressure (essentially exhaust manifold pressure) to induce choked flow.

a) Normal flow, inlet manifold to cylinder, $P_{int} > P_{cyl}$

During this period, the rate of change of cylinder mass is the intake mass flow rate minus the ring pack mass flow rate

$$\frac{dm}{dt} = \dot{m}_{int} - \dot{m}_{RP} \tag{3.138}$$

b) Reverse flow, cylinder to inlet manifold, $P_{cyl} > P_{int}$

During this case the flow is reversed to the intake manifold. Therefore, the rate of change of cylinder mass is the rate of mass loss to the intake manifold plus the rate of mass loss to the ring pack

$$\frac{dm}{dt} = -\dot{m}_{int} - \dot{m}_{RP} \tag{3.139}$$

Set of Governing Equations

The rate of change of cylinder mass is given by Eqns. (3.133)-(3.139) depending upon the relative pressures of the manifolds and cylinder pressure values. Moreover, the mass flow rate through the valve can be calculated by Eqn. (3.132) with selection of appropriate upstream and downstream pressure values.

The species conservation equation simplifies to accounting for the in-flow term only since there is no reaction in the cylinder during the gas exchange process.

$$\frac{dY_k}{dt} = \sum_{in} \frac{\dot{m}_{in}}{m} \left(Y_{k,in} - Y_k \right) \tag{3.140}$$

The in-flow can come from the intake/exhaust manifolds or the ring pack and their respective species composition, temperature and pressure values are assumed to be known. Therefore, with the appropriate in-flow enthalpies the conservation of energy equation simplifies to

$$mc_v \frac{dT}{dt} = \sum_{in} \dot{m}_{in} \left(h_{in} - \sum_k u_k Y_{k,in} \right) - P\nu \sum_{out} \dot{m}_{out} - P\frac{dV}{dt} - \dot{Q}_{ht} \tag{3.141}$$

The rate of change of pressure, similar to the compression process can be simplified as:

$$\frac{dP}{dt} = P\left[\frac{\dot{m}}{m} + \frac{\dot{T}}{T} - \frac{\dot{V}}{V}\right] \tag{3.142}$$

The final set of governing equations for the gas exchange process consists of Eqns. (3.25)-(3.33) (ring pack model) and Eqns. (3.132)-(3.142), creating a set of nine nonlinear, ordinary differential equations. The state variables are

$$\left\{m, Y_k, T, P, P_2, P_3, P_4, P_5, P_6\right\} \tag{3.143}$$

3.6 End of Cycle Calculations

Comparing the quasi-dimensional DI diesel engine computer model output with engine cylinder measurements is an important part of the development procedure of the numerical model. In this section, the description of parameters that are usually used in model-experiment comparison will be given.

The apparent heat release rate (AHRR) provides more insight about the combustion rate than can be obtained from pressure and temperature data either from an experiment or a computer simulation. The term apparent is used since the AHRR goes negative soon after SOI due to the decrease in trapped air temperature due to extraction of energy from the air to evaporate the fuel, with the consequent decrease in cylinder pressure compared to what the cylinder pressure would have been without injection. Krieger and Borman (1966) first proposed a method of quantifying the heat release rate based on the First Law of Thermodynamics. They assumed: 1) a homogenous cylinder mixture, 2) thermodynamic equilibrium, 3) complete combustion, 4) constant cylinder wall temperatures, and 5) a uniform heat transfer coefficient in the heat transfer model.

Under these assumptions, the apparent heat release rate is given by Eqn. (3.144) using the First Law of Thermodynamics.

$$\frac{dQ_{AHRR}}{d\theta} = \frac{dQ_{ch}}{d\theta} - \frac{dQ_{ht}}{d\theta} = \frac{\gamma}{\gamma - 1} P \frac{dV}{d\theta} + \frac{V}{\gamma - 1} \frac{dP}{d\theta} \tag{3.144}$$

where γ is the ratio of specific heats of the mixture. The AHRR is calculated in J/CA°.

Another useful parameter that is used in comparison of models with experimental data is the brake mean effective pressure ($bmep$). This is the normalized torque at the output of the crankshaft that is calculated from dynamometer horsepower. The quasi-dimensional DI diesel engine model simulates in-cylinder conditions. The average simulation or experimental cylinder pressure over the full cycle is called the indicated mean effective pressure $\left(imep = W_{net}/V_s\right)$. Due to friction, it is not possible to transfer all of the indicated work produced by the cylinder gases to the engine output shaft. This friction loss is quantified as the friction mean effective pressure ($fmep$).

$$bmep = imep - fmep \tag{3.145}$$

A friction mean effective pressure model similar in form to Chen-Flynn model (Chen and Flynn, 1965), based upon $imep$ and $bmep$ measurements is (Matthews, 2007):

$$fmep = K_1 + K_2 P_{\max} + K_3\left(2SN\right) + K_4\left(2SN\right)^2 \tag{3.146}$$

which yields the $fmep$ in kPa given the maximum pressure in kPa, the stroke S in mm, and the engine speed N in rpm. The constants K_1, K_2, K_3, and K_4 are determined using experimental data.

The brake specific fuel consumption ($bsfc$) is another important measure of engine performance and fuel economy and it is defined by:

$$bsfc = \frac{m_{f,inj} N}{bp \cdot x} \tag{3.147}$$

where $m_{f,inj}$ is the total fuel mass injected into the cylinder, N is the engine speed, bp is the brake power given by Eqn. (3.148), and x is the number of power strokes per crankshaft rotation which is 2 for a 4-stroke piston engine.

$$bp = bmep \frac{D \cdot N}{x} \tag{3.148}$$

where D is the engine displacement.

3.7 Solution Method

The governing equations for the quasi-dimensional direct-injection diesel engine model are sets of nonlinear, ordinary differential equations (ODEs) and partial differential equations (PDEs). These equations must be solved simultaneously for each crank angle increment over the full cycle. The structure of the quasi-dimensional direct injection diesel engine simulation code is shown in Figure 3.12.

The program first starts with reading the input file and proceeds with the initialization of the engine parameters, i.e. engine dimensions, flow coefficients, cam profiles, etc. Then, the program integrates each crank angle segment where the governing equations are simplified to represent the physics of the process. For every time step, during integration the code calls required subroutines to calculate cylinder volume and surface area, heat transfer, etc., as shown in Figure 3.12. The program checks convergence criteria at the end of the cycle and continues to run until convergence conditions are satisfied. When the model converges, the program proceeds to calculate the apparent heat release rate (AHRR), *imep*, *fmep*, *bmep*, and *bsfc* from the simulation data, then plots the figures and writes results to the hard drive.

The program initializes the temperature, pressure, residual mass fraction, and equivalence ratio at the beginning of the simulation cycle, and re-calculates these parameters and checks convergence at the end of the cycle. The start of the cycle is the intake valve closure. The re-calculated values are set as new initial values, and the program iterates until the specified 0.1% convergence tolerance is achieved.

The amount of fuel to be injected is calculated from the equivalence ratio (input to the model) and the cylinder mass at IVC:

$$m_{fuel} = m_{IVC} FA_s \phi \tag{3.149}$$

where FA_s is the stoichiometric fuel/air mass ratio, and ϕ is the input equivalence ratio. A square injection pressure profile with a delay at the start of injection is assumed since no rail pressure measurement was available during development

of the model. Although, a start of injection delay decreases with increasing rail pressure (Seykens, 2009) for simplicity a constant injector delay time to reach the set rail pressure will be assumed. The injector closed when the amount of fuel mass calculated by Eqn. (3.149) is reached.

Piston top dead center (TDC) at the beginning of the intake stroke is selected as 0° crank angle (CA). Consequently, 180° is bottom dead center (BDC) at the beginning of compression and the full engine cycle is 720°.

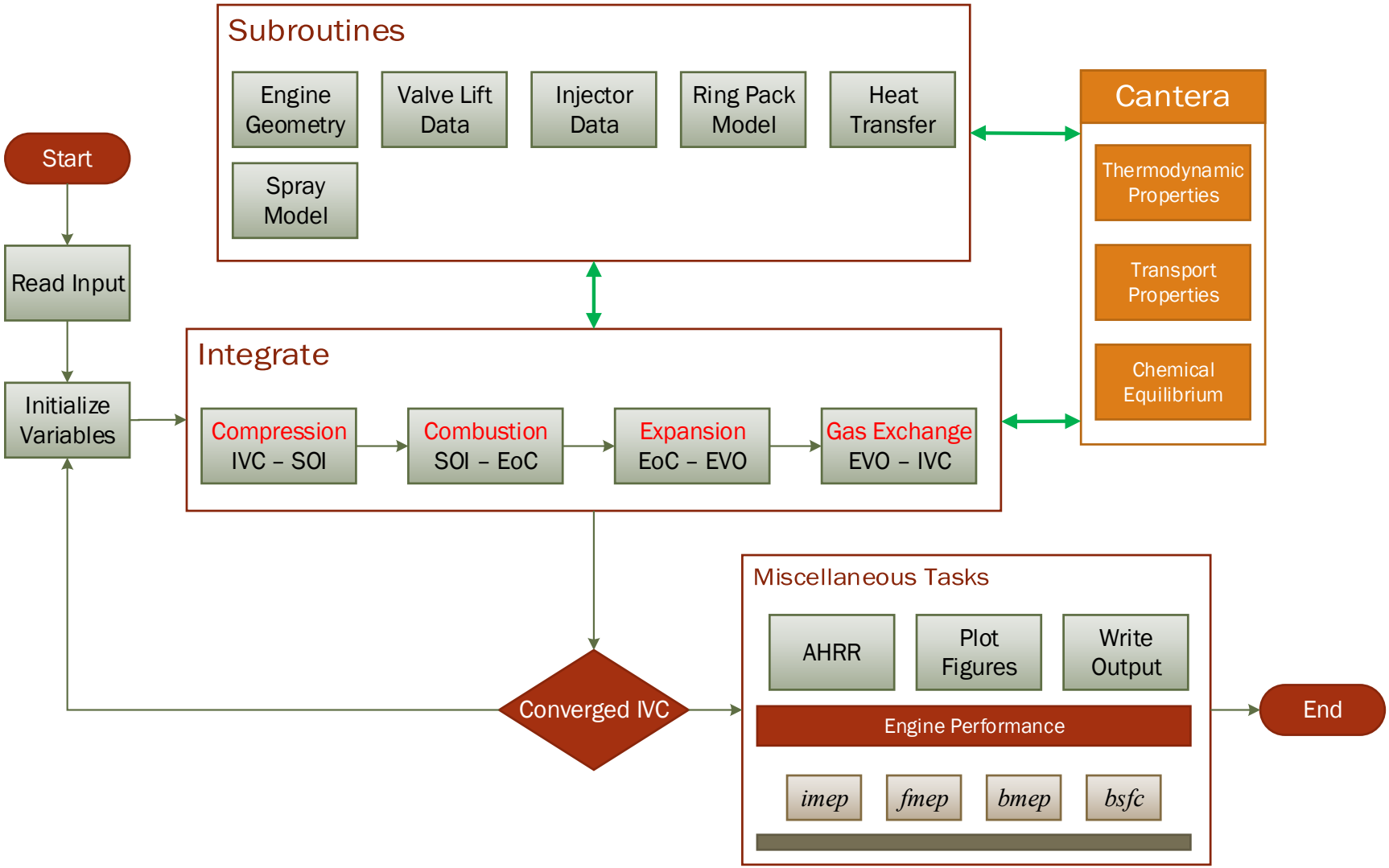

Figure 3.12 Quasi-dimensional direct injection diesel engine simulation logic flow

The quasi-dimensional engine mathematical model has been implemented in the MATLAB programming language because it is one of the most widely used packages among engineers for numerical analysis purposes (1 million users of MATLAB worldwide (MathWorks, 2016b)). Ordinary differential equations are solved using forward Euler discretization scheme for the time derivatives. This scheme is first order accurate, meaning that the error in discretization is $O\left(\triangle t\right)$.

$$\frac{df}{dt} \approx \frac{f_{t_{i+1}} - f_{t_i}}{\triangle t} \tag{3.150}$$

The chemical equilibrium is solved by using Cantera (Goodwin *et al.*, 2014). Cantera is a freeware software tool add-on to MATLAB that is used for problems involving chemical kinetics, thermodynamics, and transport processes. A reduced reaction mechanism of n-heptane with 29 species and 52 reactions validated under both constant-volume and DI diesel engine conditions (Patel, Kong and Reitz, 2004) is used in Cantera in order to find the equilibrium composition of the products from both the premixed and the diffusion flames.

Chapter 4

Results and Discussion

The quasi-dimensional DI diesel engine model results will be compared against the experimental measurements obtained from a 6 cylinder, 15 L turbocharged heavy-duty DI diesel engine. The specifications of the engine as tested by Southwest Research Institute (SwRI) are listed in Table 4.1. First, the experimental cases will be described; second, the calibration procedure with the obtained calibration coefficients will be presented, and finally, the model and experiment results will be compared along with the zonal results.

Table 4.1 Specifications of the turbocharged heavy-duty DI diesel engine

Compression ratio :	18.9
Bore :	136.9 mm
Stroke :	168.9 mm
Displacement:	15 L
EVO :	497.2°
IVO :	703°

4.1 Engine Operating Points

In this research, 12 engine operating points that cover 3 sets of engine speeds (i.e. low, medium, and high speeds) and 4 levels of engine load (Figure 4.1) were used to calibrate and test the developed quasi-dimensional DI diesel engine model. The cases with the corresponding engine speed, power, torque, and load

along with injection timing and overall equivalence ratio are presented in Table 4.2.

Table 4.2 Experimental engine operating points

Case #	Engine Speed rpm	Engine Power kW	Engine Torque N-m	Load %	SOI BTDC	Equivalence Ratio None
1	1243	319	2447	100	8°	0.50
2	1243	239	1836	75	9°	0.44
3	1243	160	1228	50	8°	0.38
4	1243	80	615	25	7°	0.28
5	1539	345	2139	100	9°	0.54
6	1539	259	1609	75	10°	0.44
7	1539	174	1078	50	9°	0.34
8	1539	87	537	25	9°	0.31
9	1830	342	1783	100	10°	0.55
10	1830	256	1338	75	10°	0.47
11	1830	171	891	50	10°	0.39
12	1830	85	445	25	8°	0.28

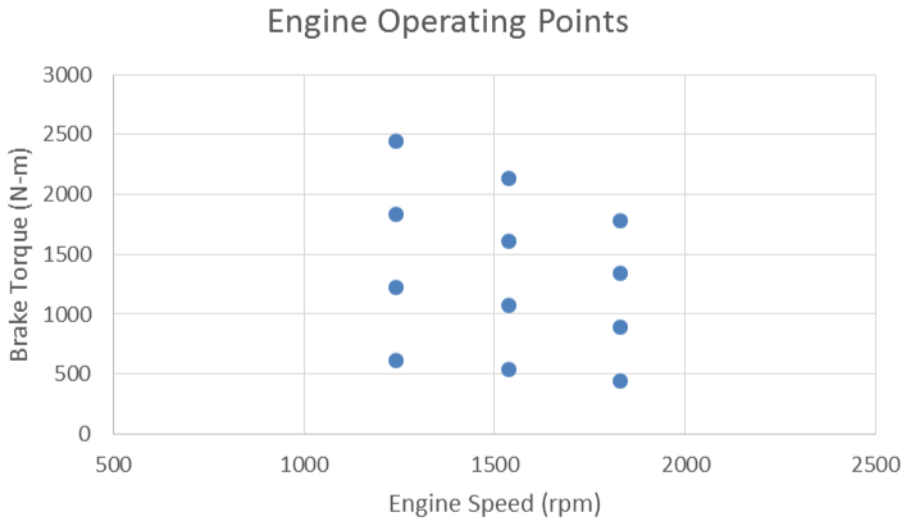

Figure 4.1 Experimental engine operating points on the torque speed map

4.2 Engine Model Calibration

The empirical models implemented in the quasi-dimensional DI engine model use coefficients given in the respective literature except the fuel evaporation and the diffusion combustion models. The calibration of the engine model was carried out using all of the available cases by comparing the cylinder pressure obtained by the simulation with the experimental, in addition to the comparison of a few performance parameters selected.

The friction mean effective pressure (*fmep*) model expressed in Section 3.6 was calibrated using the test cell measurements of net indicated and brake mean effective pressures (*nimep* and *bmep*).

4.2.1 Evaporation Model Calibration

The evaporation of the liquid-fuel does not emphasize its effect on the cylinder pressure (i.e. kneeling of the cylinder pressure curve) during the ignition delay period for the modern high pressure injector equipped diesel engines. Therefore, another data set showing "kneeling" in the cylinder pressure from a different diesel engine was utilized for the calibration of the evaporation constant. The specifications of this engine are presented in Table 4.3.

Table 4.3 Specifications of the second DI diesel engine used for the calibration of the spray evaporation

Compression ratio :	17
Bore :	131 mm
Stroke :	158 mm
Displacement:	12.9 L

The evaporation fraction of the injected fuel mass in the time step (χ) is plotted against the ratio of spray length to liquid length (x^*) for different evaporation calibration constants (k) during the transient period of Zone 1 as shown in Figure 4.2. In all of the cases, when liquid length is reached, the evaporation fraction becomes unity. The evaporation curve was expressed as (Eqn. (3.61))

$$\chi = \frac{kx^*}{1 + k - x^*} \tag{4.1}$$

Four levels of evaporation constant (0.2, 0.3, 0.4, and 1) are applied to the engine model and the obtained cylinder pressures plotted against the cylinder pressure obtained from the test cell (Figure 4.3). There is not any significant variance among the cylinder pressures simulated for the considered set of evaporation constants. With the assumed curve however, the "kneeling" effect due to evaporation was captured in the simulated cylinder pressure. For completeness, an evaporation constant of 0.3 was selected by re-stating that no significant difference was observed among the set of evaporation constants used in the calibration.

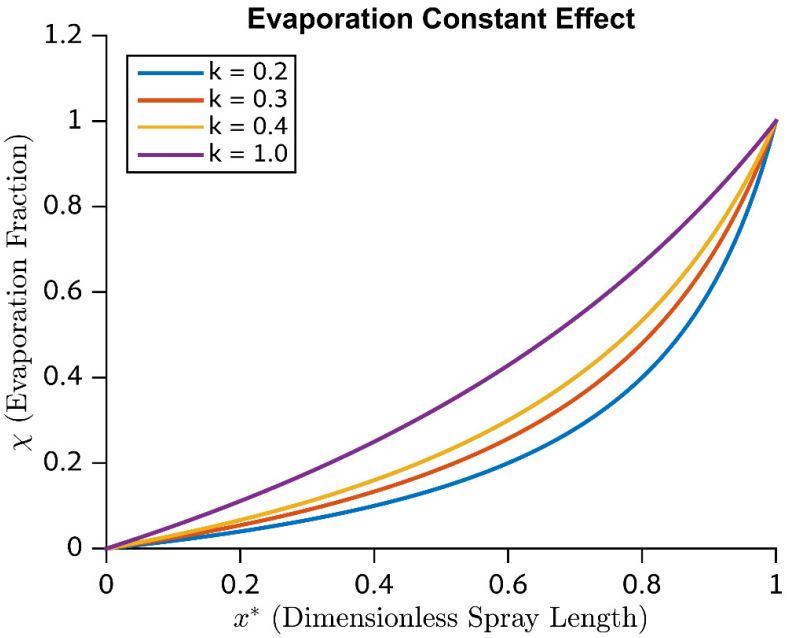

Figure 4.2 Effect of the evaporation constant on evaporation fraction

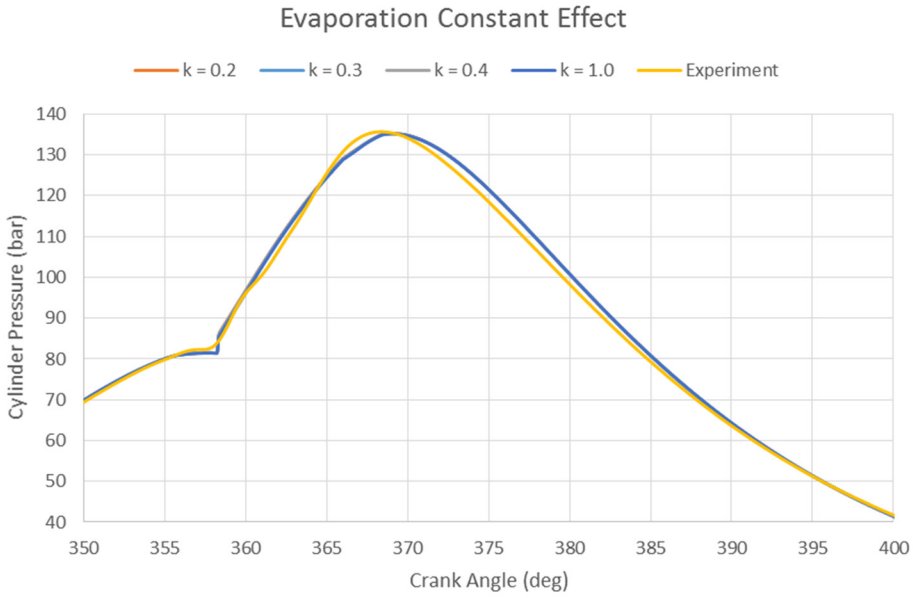

Figure 4.3 Effect of the evaporation constant on cylinder pressure

4.2.2 Diffusion Combustion Model Calibration

The diffusion flame onsets at the end of the auto-ignition period and exists until the end of combustion. Hence, calibration of the amount of fuel consumed by Zone 5 has a strong effect on the simulation results. The mixing frequency based on the turbulence model controls the mass of the "fuel" entrained from Zone 4 to the diffusion flame, as developed in Section 3.3.3.2

$$f_m = C_{diff} \frac{\sqrt{c_G \overline{S}_p^2 + c_k \frac{k}{\frac{3}{2} m}}}{\sqrt[3]{\phi \frac{V}{n_N}}} \tag{4.2}$$

Three coefficients C_{diff}, c_G, and c_k are the calibration coefficients of the mixing frequency determined using the engine operating points presented in Table 4.2 for the 15 L engine (Table 4.1). The three calibration coefficients have to be tuned simultaneously since it is not possible to single out the effect of individual terms. Therefore, literature values were used as a guide in this process and it should be noted that there may be other possible combinations of these coefficients resulting in similar results since the calibration was carried out manually.

Barba *et al.* (2000) reported c_G values to be changing from 1.8 to 3 for the three engines they tested and c_k from 0.1 to 0.4. On the other hand, Maiboom *et al.* (2009) determined calibration coefficients c_G of 0.5, c_k of 1 , and C_{diff} of 5 with mathematical optimization when targeting rate of heat release (**ROHR**).

In this research, the mixing frequency interacts with a "fuel" zone that is feeding only to the diffusion flame. On the other hand, Barba *et al.* (2000) and

Maiboom *et al.* (2009) controlled the interaction of the premixed and diffusion combustion with a single "fuel" zone.

There are two phases of the diffusion combustion: 1) when the injector is on, and 2) when the injector is off. The loss of continuous momentum supplied by the injector is expected to change the behavior of the diffusion flame which is surrounding the diesel jet. This momentum change will not affect the mean mixing velocity coefficients of c_G and c_k since the mean piston speed is constant for a given engine speed and the turbulent kinetic energy already considers the injector nozzle kinetic energy. On the other hand, C_{diff} will be affected from injector closing and will be used to compensate for the measurement error, turbulence model error and other simulation errors similar to the period when the injector is on. The calibration coefficients of the diffusion combustion model obtained using twelve engine operating conditions are presented in Table 4.4. Next, the effect of each calibration coefficient on the cylinder pressure will be presented for Case 7, 1539 rpm and 50% load engine operating point (Table 4.2).

Table 4.4 Calibration coefficients of the diffusion combustion model

c_G	1.8
c_k	0.1
C_{diff} (Injector on)	2.35
C_{diff} (Injector off)	1.85

The quasi-dimensional engine model was run for the mixing velocity coefficient c_G values of 1.0, 1.8 and 2.5. The cylinder pressures for each coefficient

are plotted against the test cell cylinder pressure as shown in Figure 4.4. Similar to the results of Barba *et al.* (2000), $c_G = 1.8$ matched cylinder pressure better.

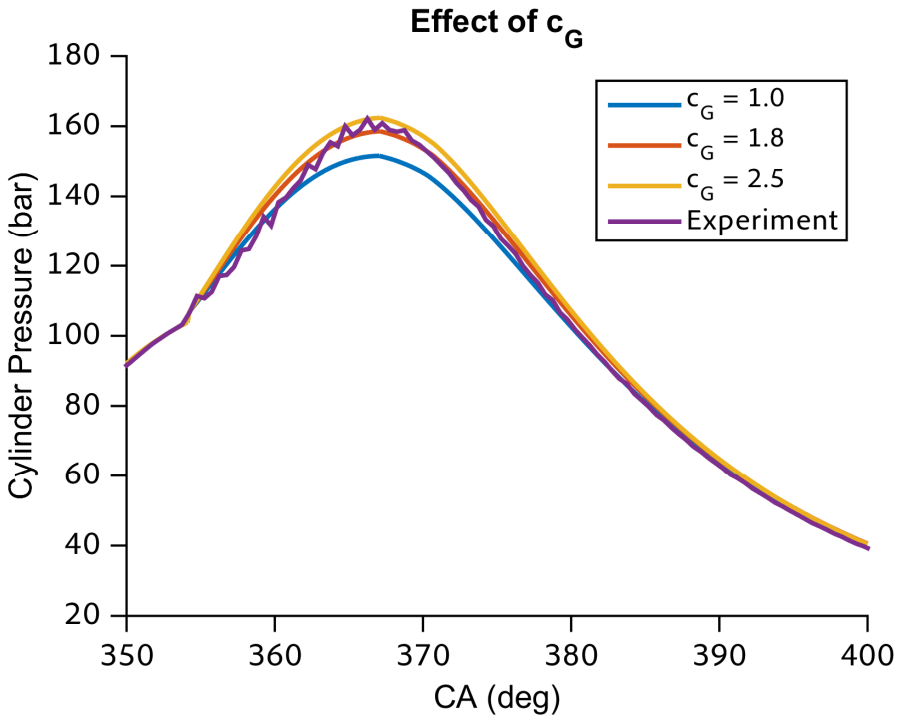

Figure 4.4 Effect of the calibration coefficient c_G on the cylinder pressure (Case 7)

On the other hand, the second mixing velocity coefficient c_k values of 0.05, 0.1 and 0.15 were tested with the engine model, but there was not a significant effect observed on the cylinder pressure (Figure 4.5).

Additionally, the quasi-dimensional engine model was run for c_k values of 0.4 (Barba *et al.*, 2000) and 1 (Maiboom *et al.*, 2009) and the mean error of a few key engine operating parameters were reported in Table 4.5. The mean error of each parameter was determined by dividing the difference between simulation and measurement to the measurement value:

$$\%error = \frac{simulation - measurement}{measurement} \times 100 \tag{4.3}$$

c_k of 0.1 gave better results for the engine torque, exhaust mass flow rate, and *nimep* (Net Indicated Mean Effective Pressure). However, by increasing the coefficient, the peak cylinder pressure approached the experimental value while the mean error in the remaining parameters increased. Therefore, the second mixing velocity coefficient c_k was found to be 0.1 in this study similar to Barba *et al.*'s work (2000).

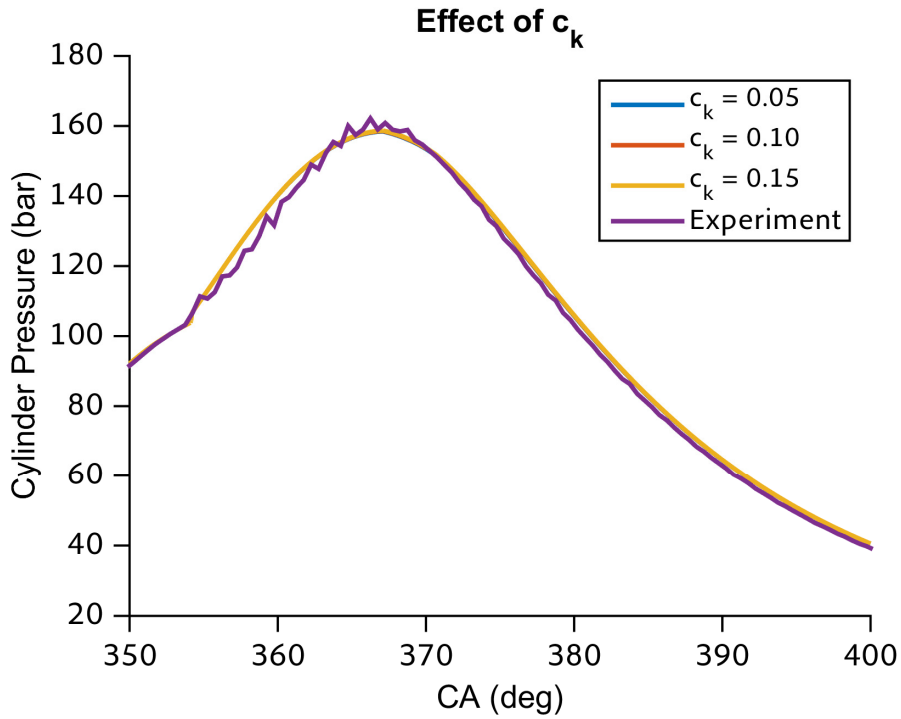

Figure 4.5 Effect of the calibration coefficient c_k on the cylinder pressure (Case 7)

Table 4.5 Mean error of the twelve cases for key engine parameters using various second mixing velocity coefficients, c_k

	$c_k = 0.1$	$c_k = 0.15$	$c_k = 0.4$	$c_k = 1$
Engine Torque	0.67%	0.74%	1.04%	1.36%
Exhaust Flow Rate	1.01%	1.03%	1.12%	1.27%
NIMEP	0.36%	0.43%	0.74%	1.12%
Peak Cylinder Pressure	-2.20%	-2.07%	-1.48%	-0.23%

The coefficient of C_{diff} was set to values of 1.5, 2.35, and 3 when the injector was operating. The cylinder pressure obtained using $C_{diff} = 2.35$ matched test cell cylinder pressure better than the other two values as shown in Figure 4.6.

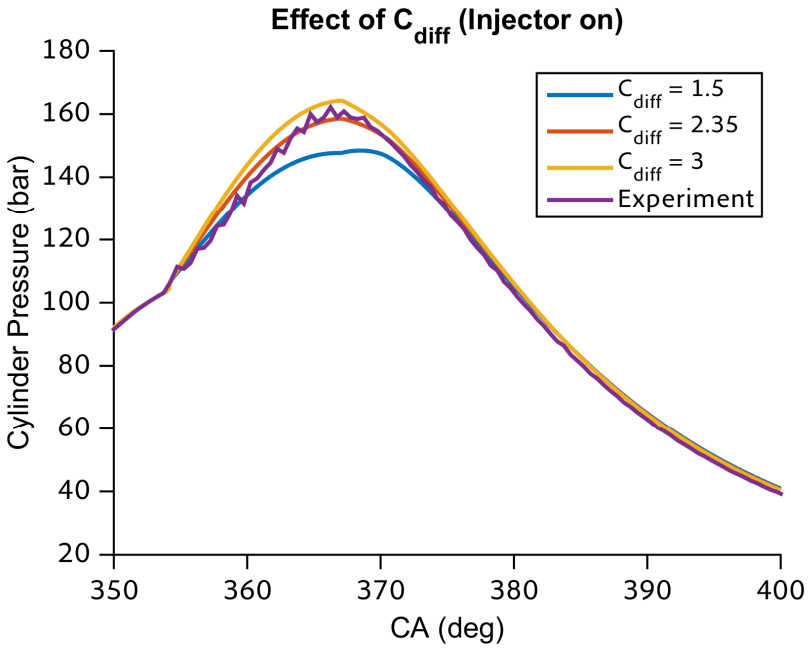

Figure 4.6 Effect of the calibration coefficient C_{diff} (Injector on) on the cylinder pressure (Case 7)

The final calibration constant C_{diff} (Injector off) was set to values of 1.5, 1.85, and 2.35 and obtained cylinder pressure was compared with test cell measurement as shown in Figure 4.7.

$C_{diff} = 1.5$ matched experimental cylinder pressure better than 1.85 and 2.35 values for the Case 7 operating point. However, C_{diff} of 1.5 and 1.85 performed better than 2.35 when twelve cases were considered (Table 4.6). The mean error for the *nimep* and the peak cylinder pressure (PCP) were better for $C_{diff} = 1.85$ than 1.5. However, the engine torque and the exhaust mass flow rate were estimated better with $C_{diff} = 1.5$ compared to 1.85. Hence, the calibration coefficient was selected to be $C_{diff} = 1.85$ when the injector is closed for the mixing frequency model since it is closer to the $C_{diff} = 2.35$ when the injector is open and performed overall slightly better than the 1.5 value.

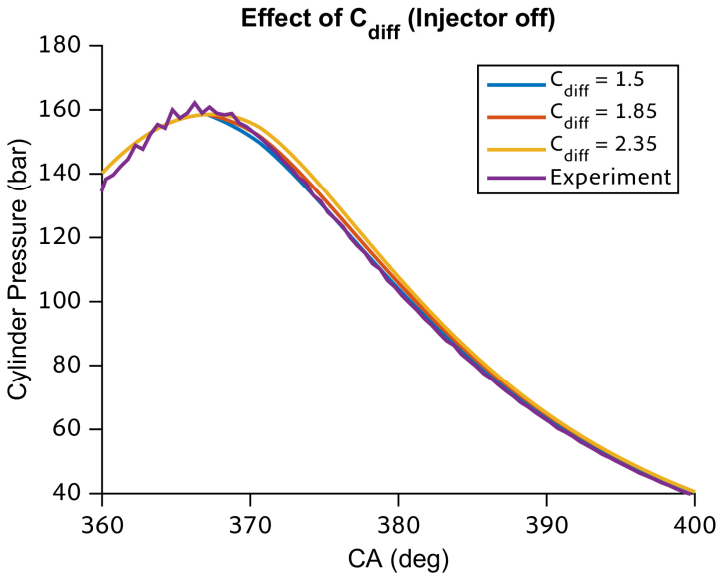

Figure 4.7 Effect of the calibration coefficient C_{diff} (Injector off) on the cylinder pressure (Case 7)

Table 4.6 Mean error of the twelve cases for key engine parameters using C_{diff} (Injector off) values of 1.5, 1.85 and 2.35

	$C_{diff} = 1.5$	$C_{diff} = 1.85$	$C_{diff} = 2.35$
Engine Torque	-0.34%	0.67%	1.32%
Exhaust Flow Rate	0.91%	1.01%	1.12%
NIMEP	-0.58%	0.36%	0.99%
Peak Cylinder Pressure	-2.47%	-2.20%	-1.66%

4.2.3 Friction Mean Effective Pressure Calibration

There are two common methods of measuring friction mean effective pressure (*fmep*) in internal combustion engines: 1) motoring test, and 2) firing test.

In a motoring experiment the engine is driven by a dynamometer without firing and the torque is measured. Motoring test can be carried out hot or cold, a preferred method would be turning off firing while the engine is operating steadily and measuring the motoring torque. This way one can capture the effect of the temperature of the oil and the cooling water. However, it is not possible to separate the pumping loop from friction and there are no bearing loads due to combustion.

On the other hand, the firing test is carried out when the engine is running normally at a steady operating point. The crank angle resolved cylinder pressure must be measured by a high speed data acquisition system along with accurate brake torque measurements. The *fmep* can be calculated from the difference between net indicated (*nimep*) and the brake mean effective pressures (*bmep*) as explained in Section 3.6. The *fmep* obtained with the firing test is prone to

measurement error in *nimep* and *bmep* i.e. *fmep* may be small compared to the other two pressures.

In this research *nimep* was calculated from crank angle resolved cylinder pressure, *bmep* was calculated from brake torque as given by Eqn. (3.148), and *fmep* was calculated using these two parameters. The experimental *fmep* obtained was fitted with a friction model that considers the peak cylinder pressure and the mean piston speed as expressed in Section 3.6 by the following relation (Matthews, 2007):

$$fmep = K_1 + K_2 P_{\max} + K_3\left(2SN\right) + K_4\left(2SN\right)^2 \tag{4.4}$$

The coefficients of the *fmep* relation were found to be $K_1 = 139.58kPa$, $K_2 = 0.005$, $K_3 = -3.39 \cdot 10^{-4}\, kPa/rpm \cdot mm$, and $K_4 = 2.56 \cdot 10^{-10}\, kPa/\left(rpm \cdot mm\right)^2$. The R^2 between the test cell *fmep* and the friction model fit was found to be 0.69. The *fmep* of the twelve engine operating points are plotted with respect to the peak cylinder pressure (Figure 4.8) and the engine speed (Figure 4.9) in order to show their effect and the quality of the friction model.

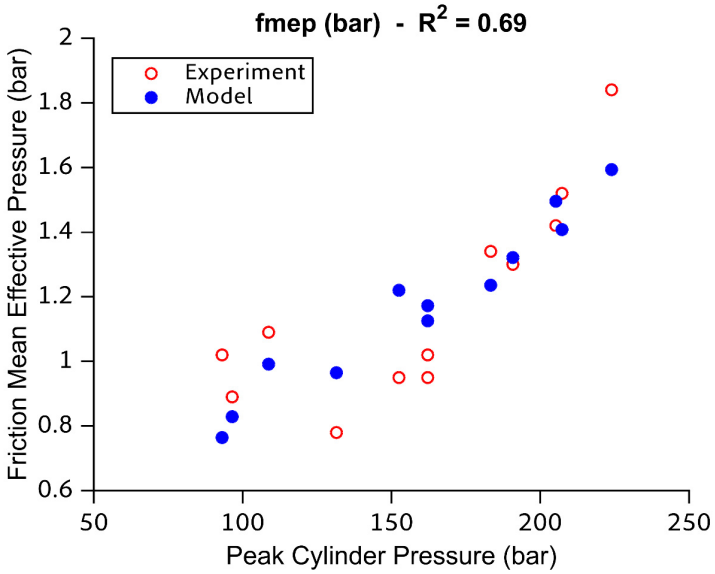

Figure 4.8 Friction mean effective pressure with respect to the peak cylinder pressures of twelve engine operating points

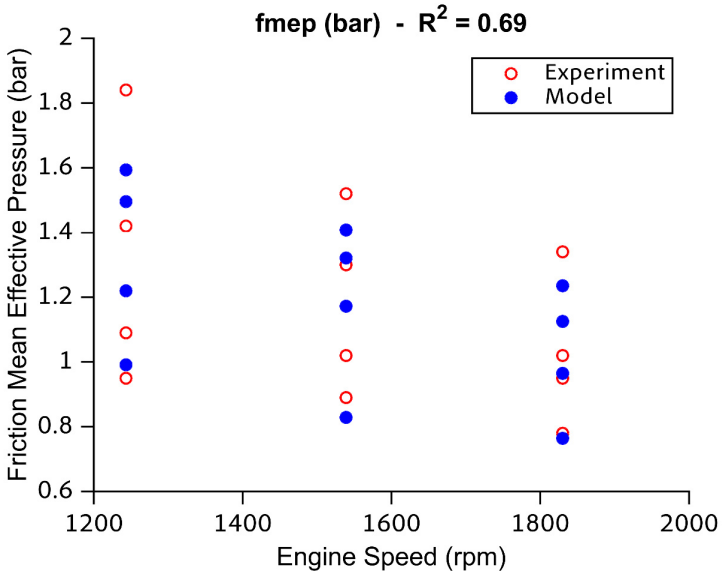

Figure 4.9 Friction mean effective pressure with respect to the engine speeds of twelve engine operating points

4.3 Engine Model Validation

The quasi-dimensional engine model results were compared with the test cell measurement for the Case 1 operating point (Table 4.2) and results of the other cases are listed in the Appendix section. Case 1 data were taken at 1243 rpm and 100% engine load.

The engine model runs iteratively until the changes in the cylinder bulk temperature and pressure at intake valve closure (IVC) are less than 0.1%. For two iterations of the quasi-dimensional engine model run for Case 1, the bulk cylinder temperature, and pressure are plotted in Figure 4.10.

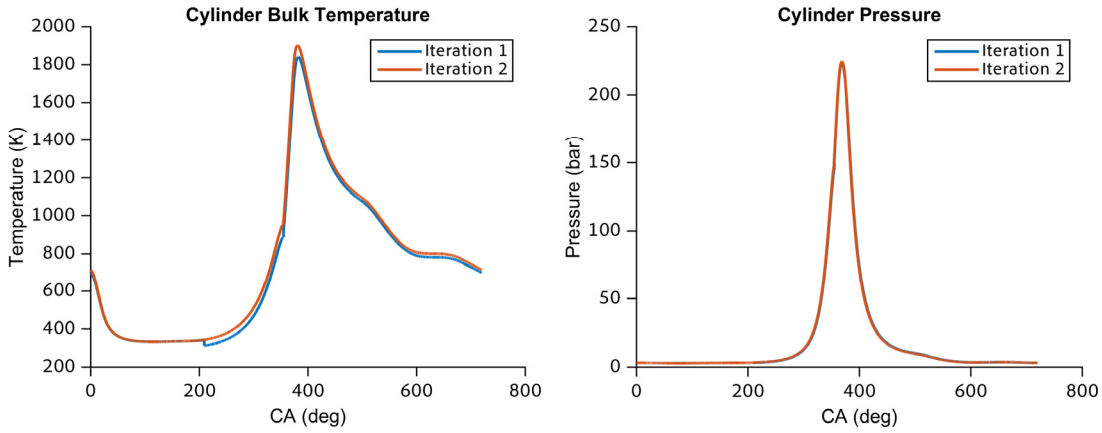

Figure 4.10 Engine model runs iteratively until the change in cylinder bulk temperature and pressure at intake valve closure (IVC) are less than 0.1% (Case 1)

The cylinder pressure is plotted in three different configurations in order to analyze the matching quality of the simulation results with experiment (Figure 4.11). The cylinder pressure with respect to crank angle plot shows that the simulation cylinder pressure follows the test cell measurement closely. In order to analyze pumping loop characteristics, cylinder pressure is plotted with respect

to the cylinder volume normalized by the maximum cylinder volume and shown on a logarithmic scale.

Simulated cylinder pressure does not match test cell measurement as closely as the closed cycle portion of the cycle in the pumping loop since low speed manifold pressures were used in this research. For better cylinder pressure estimates in the pumping loop, high speed crank angle resolved manifold pressures are a must. In the third configuration, cylinder pressure is plotted against cylinder volume. The simulated pressure follows test cell measurement closely in the compression and expansion strokes, while the peak cylinder pressure is matched.

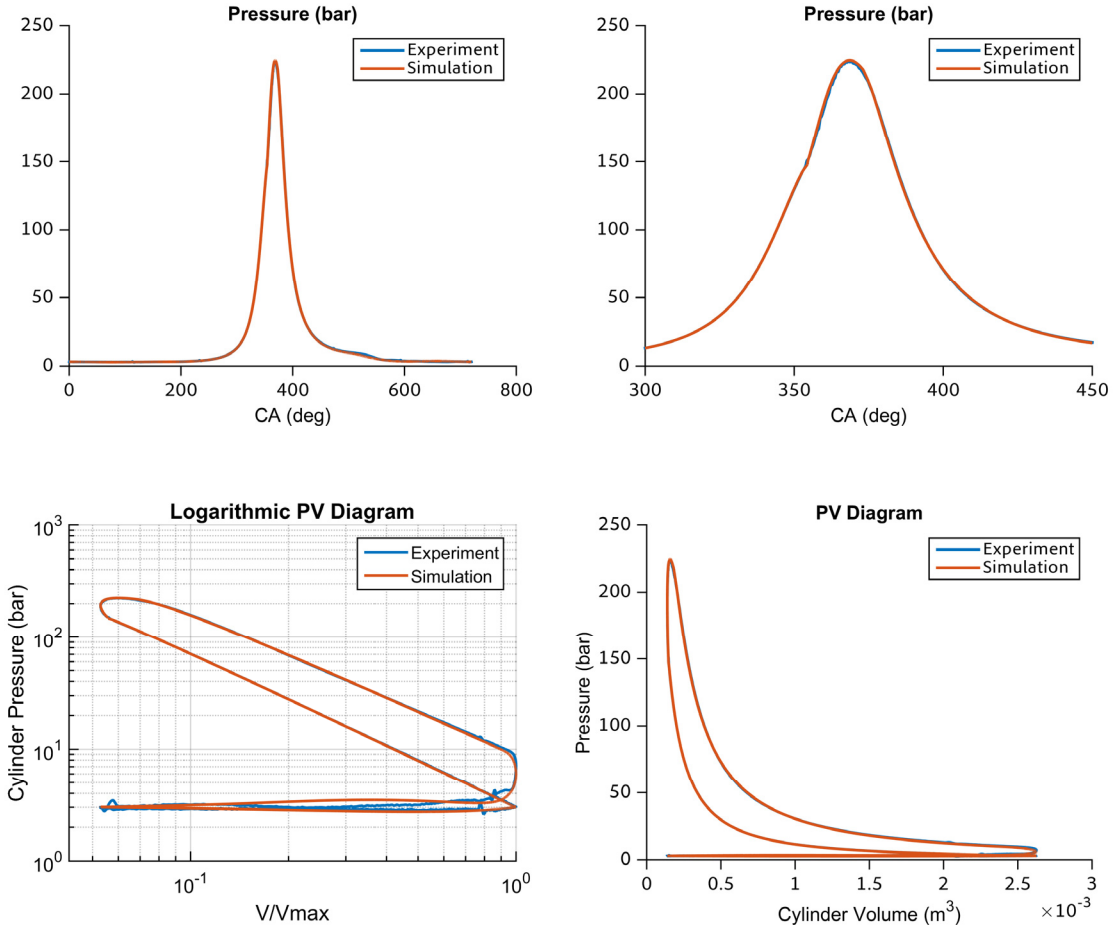

Figure 4.11 Cylinder pressure, logarithmic PV, PV, and AHRR diagrams for Case 1

The apparent heat release rate (AHRR) is one of the parameters commonly used to analyze simulation results as explained in Section 3.6. When a simple finite difference scheme is used to find the rate of change of pressure, the resulting AHRR curve becomes noisy. Hence, experimental data were smoothed using a moving average filter, a low pass filter with filter coefficients equal to the reciprocal of the span (MathWorks, 2016a). However, it was recognized that even a small miss-match between simulation and experiment cylinder pressures can result in a difference in AHRR, as shown in Figure 4.12 for Case 1.

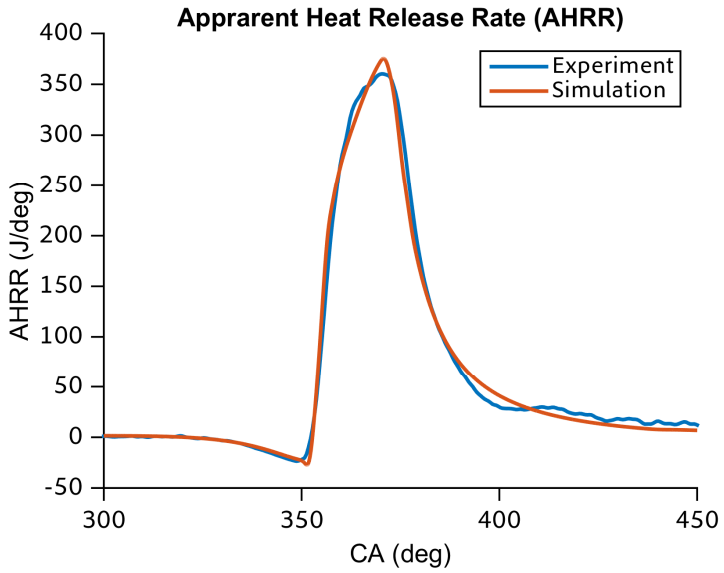

Figure 4.12 Comparison of simulation AHRR with test cell (Case 1)

The quasi-dimensional engine model was run with the twelve engine operating points considered (Table 4.2). The engine power, the engine torque, *nimep*, *bmep*, *fmep*, the exhaust mass flow rate, the peak cylinder pressure (PCP), and the location of PCP were identified to be a few key engine performance parameters used to validate the engine model.

The mean errors of the listed engine parameters were calculated using Eqn. (4.3) and are reported in Table 4.7 along with the standard deviation of mean error. The simulation results are plotted against the test cell measurements of the twelve engine operating points for the selected key engine parameters in Figure 4.13 and Figure 4.14.

The mean error for all of the parameters considered are within 3% while the standard deviation is within about 5% except *fmep* and the PCP location. The variation in *fmep* and PCP location are relatively higher due to their small values.

When the *nimep* and *bmep* plots of Figure 4.13 are compared, it can be concluded that the variation of *fmep* does not affect *bmep* strongly.

Table 4.7 The mean error and the standard deviation of mean error for the key engine parameters obtained for the twelve engine operating points

	Mean Error	**Standard Deviation of Mean Error**
Engine Power	0.67%	5.10%
Engine Torque	0.68%	5.09%
Exhaust Mass Flow Rate	1.01%	3.64%
NIMEP	0.36%	3.80%
BMEP	1.22%	5.12%
FMEP	-2.59%	15.38%
PCP	-2.20%	1.43%
PCP Location	-2.91%	10.78%

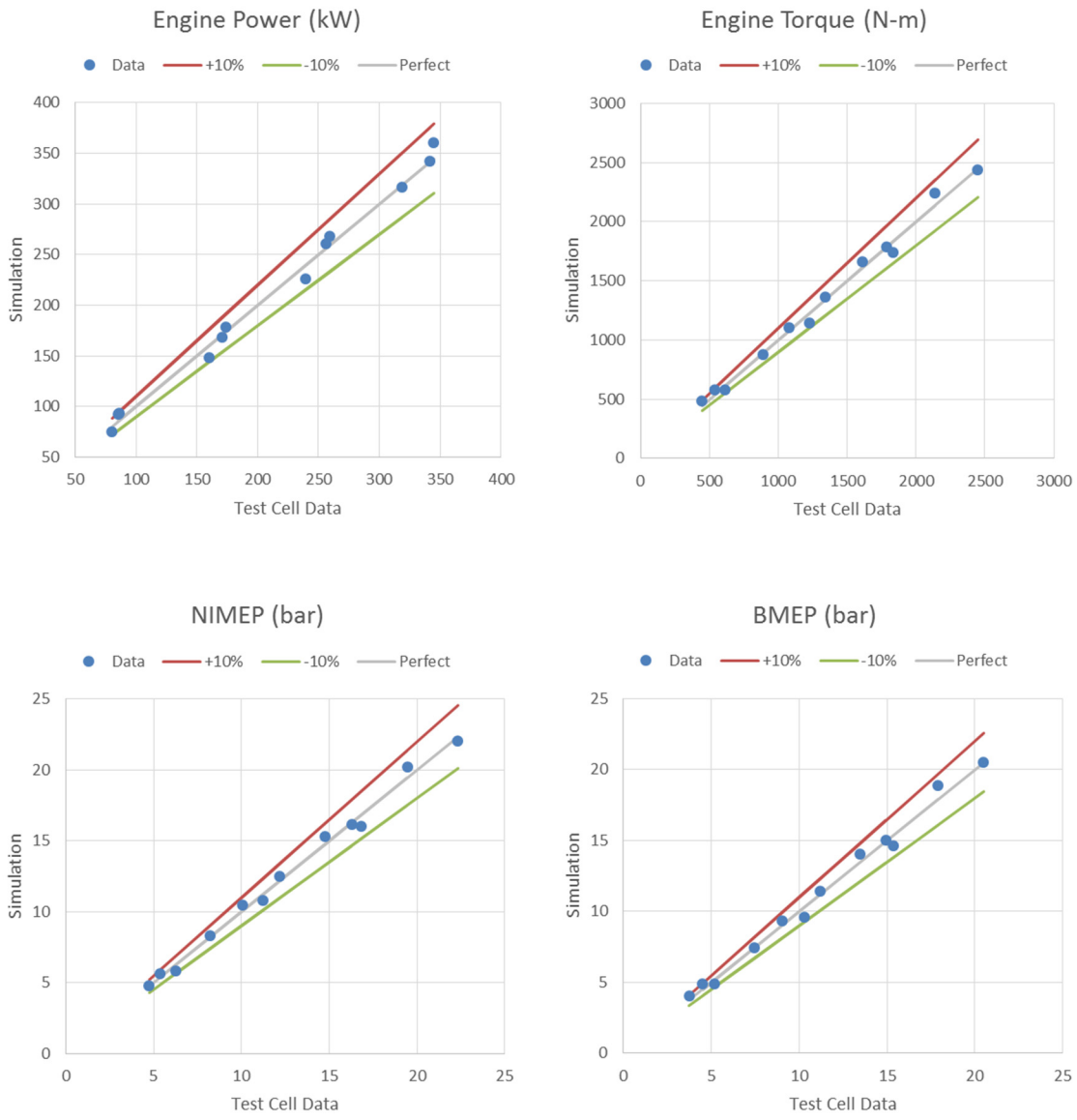

Figure 4.13 Comparison of simulation results with test cell measurements for engine power, engine brake torque, NIMEP, and BMEP. +10% (red line) and -10% (green line) deviation from the perfect simulation match (gray line) are shown.

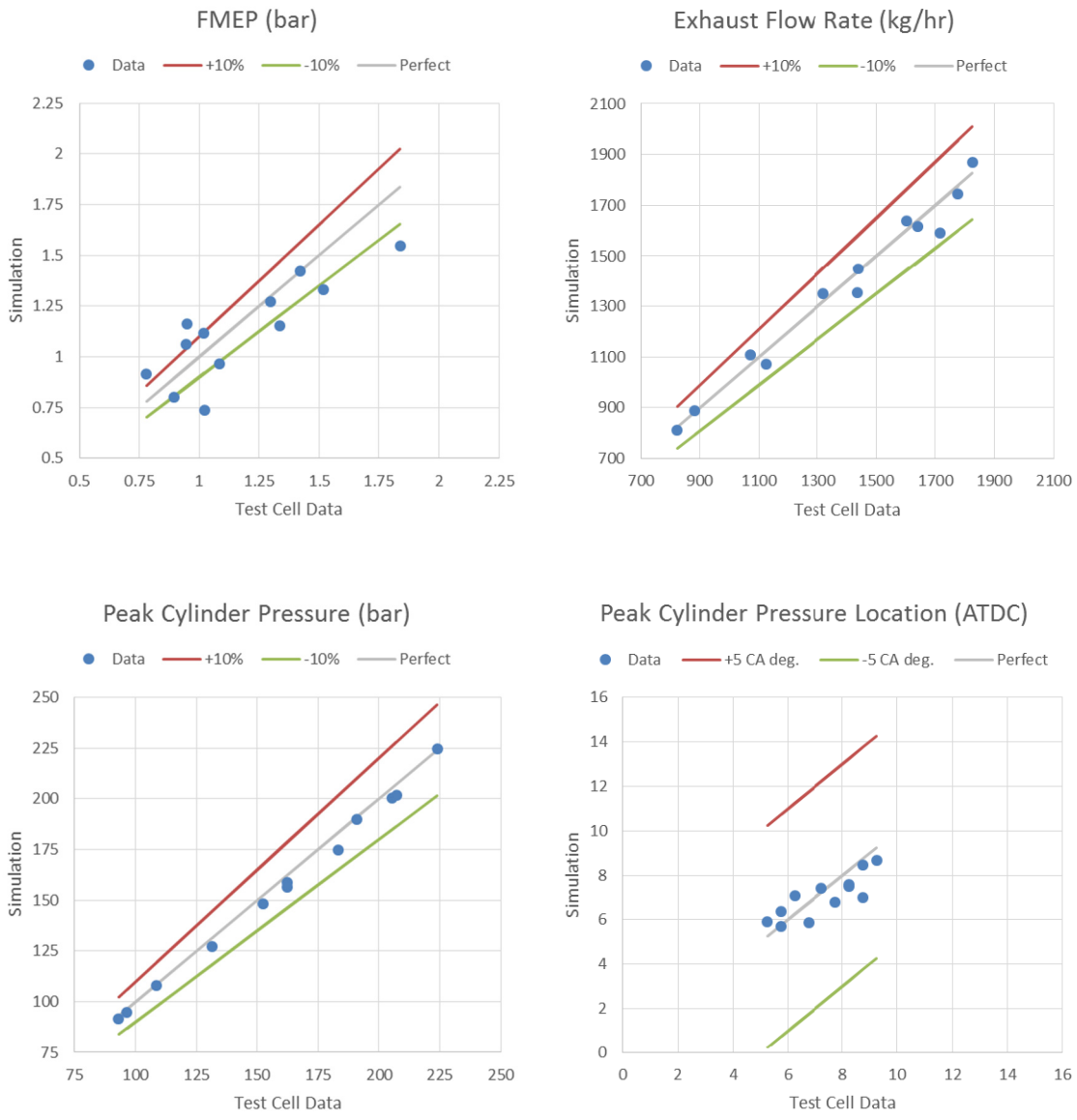

Figure 4.14 Comparison of simulation results with test cell measurements for FMEP, exhaust mass flow rate, peak cylinder pressure, and peak cylinder pressure location. +10% and +5 CA° (red line), and -10% and -5 CA° (green line) deviation from the perfect simulation match (gray line) are shown.

The fuel map of the 6 cylinder, 15 L turbocharged heavy-duty DI diesel engine was obtained using 12 engine operating points used for the calibration and the validation as shown in Figure 4.15. Generated fuel map can now be used with the University of Texas Fuel Economy model along with the coastdown coefficients and the drive cycles obtained by the author to estimate fuel consumption.

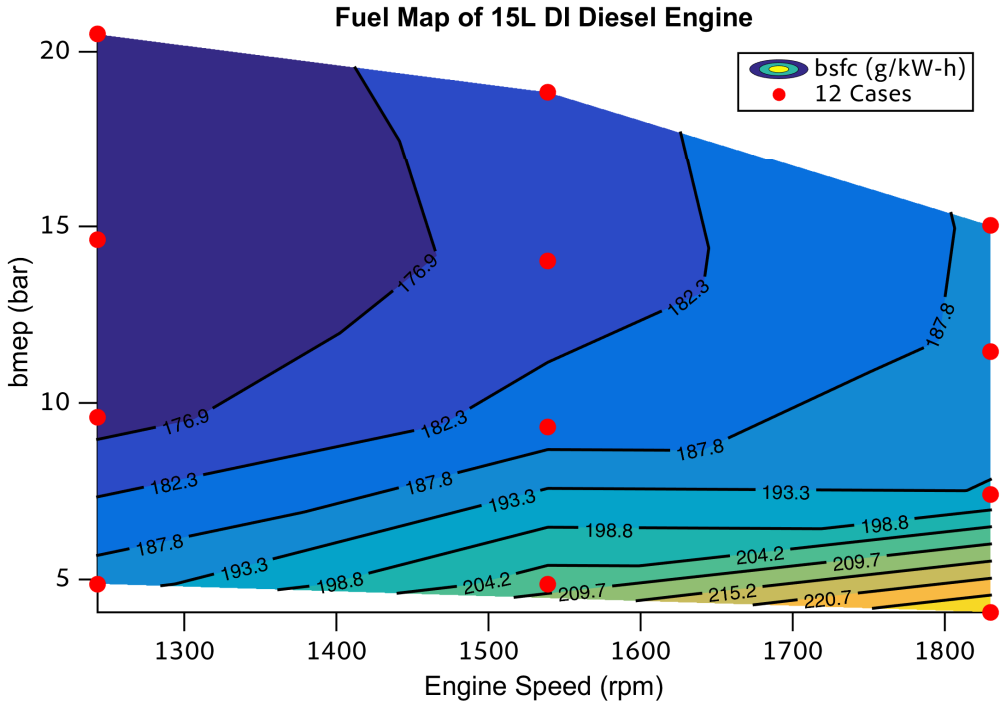

Figure 4.15 The fuel map generated using 12 engine operating points of the 6 cylinder, 15 L turbocharged heavy-duty DI diesel engine

4.4 Engine Model Zone Results

The behavior and the features of each zone described in the quasi-dimensional engine model will be presented in this section in detail. For this purpose Case 1 was selected, 100% load at 1243 rpm (Table 4.2).

The evolution of the cylinder contents with advance of the crankshaft is described using the thermodynamic processes. In addition to the four thermodynamic strokes, the combustion process is divided into the sub-events. After the compression stage, the combustion process starts with the injection of the spray. The period starting with injection up to the time at which the liquid length of Zone 1 is established is referred to as the developing spray (Zone 1). Similarly, the period during which Zone 2 is evolving is also referred to as the developing spray (Zone 2) until auto-ignition occurs. At the end of the ignition delay period the auto-ignition period starts. When the combustion consumes all of the available oxygen in Zone 2, the quasi-steady period starts. The quasi-steady period continues until the end of injection. The period during which the combustion is sustained without the injection of fuel is referred to as the EoI (End of Injection) period. In more advanced crank angles, the cylinder temperature drops due to the expansion of volume as the piston descends and the combustion can no longer be sustained. Then the cylinder is modeled as a single zone (Zone 0) and this period is referred to as the expansion until the exhaust valve opens (EVO).

The gas phase characteristics within the cylinder for Zone 0 are described by the zone governing equations. The cylinder pressure is found iteratively for each time step using the total internal energy, the density and the gaseous mixture composition of Zone 0. Using the ideal gas law, the bulk cylinder temperature is calculated from the cylinder pressure and the mass of cylinder gases. The major pressure and temperature increases occur during the quasi-steady period of the combustion period as shown in Figure 4.16 and Figure 4.17. The longest period of the combustion was the EoI period for the high load case considered. The ignition

delay takes just a few crank angles and with the auto-ignition there is a discontinuity due to the high rate of change of temperature in Zone 2. However, this high rate can be sustained for only a few time steps because of the relatively small mixture mass that has accumulated in Zone 2 during the ignition delay (Figure 4.19). Hence, auto-ignition creates a marginal increase in cylinder pressure.

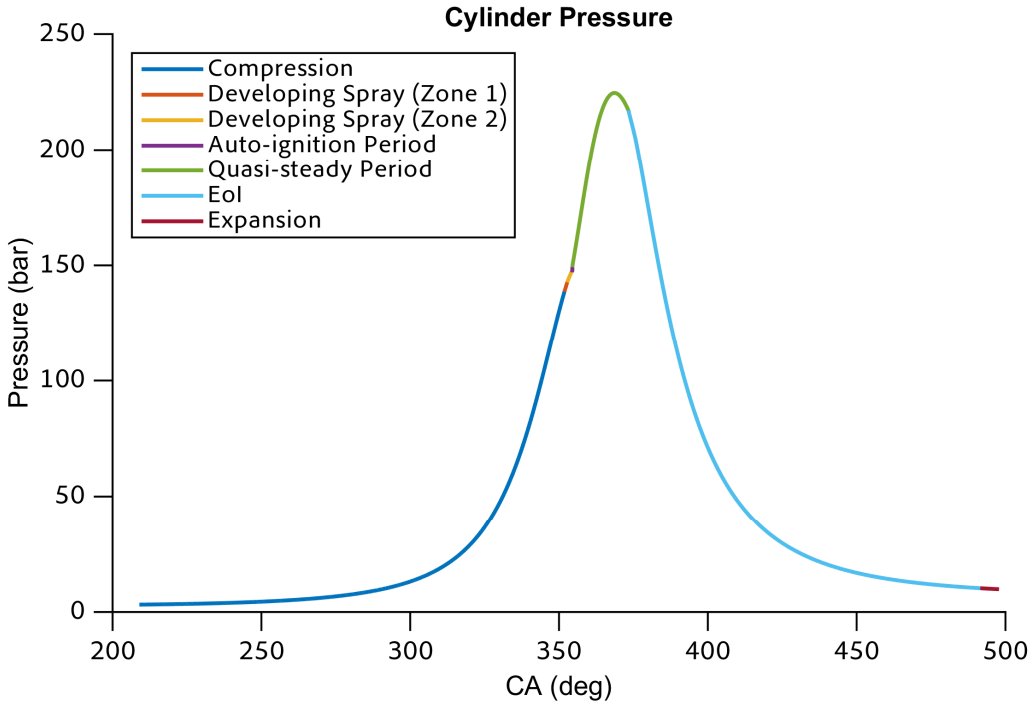

Figure 4.16 Variation of the cylinder pressure with thermodynamic processes (Case 1)

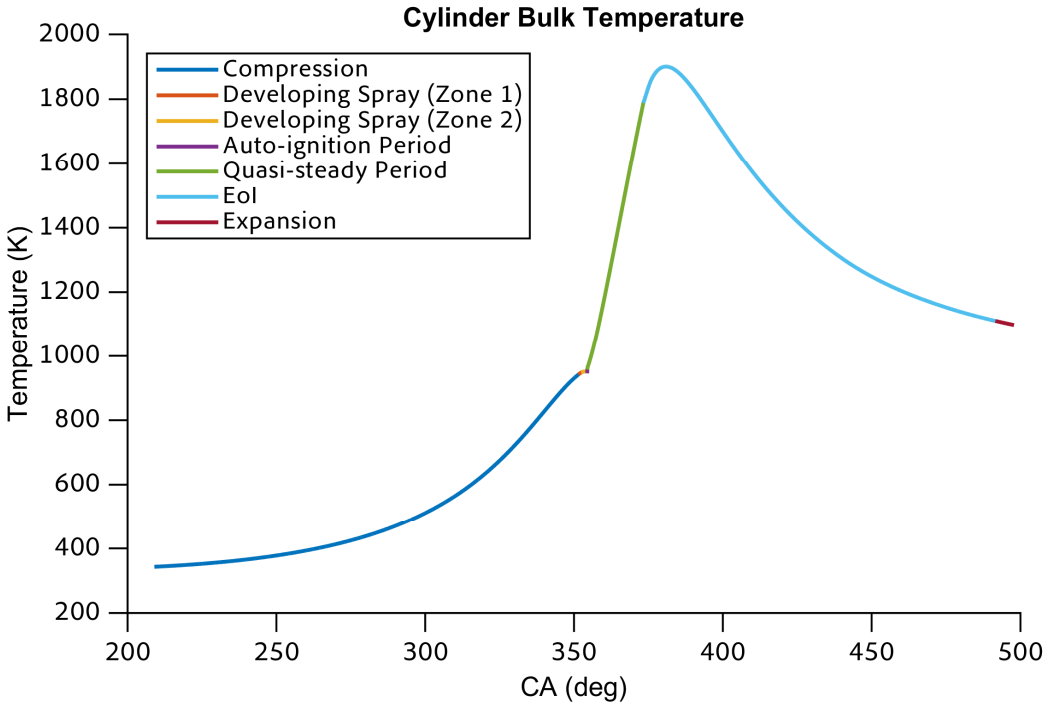

Figure 4.17 Variation of the bulk cylinder temperature with thermodynamic processes (Case 1)

The injected liquid fuel mixes with the entrained air from Zone 6 and forms Zone 1. Up to the liquid length, the average temperature of Zone 1 increases due to the entrainment of relatively higher temperature air as shown in Figure 4.18. The equivalence ratio of Zone 1 decreases gradually from fuel only to an equivalence ratio in the range of 3 to 4. The equivalence ratio of Zone 1 stays constant throughout the development of Zone 2 and the auto-ignition period as long as the rate of fuel injection stays constant. However, during the quasi-steady period the diffusion flame envelopes the spray and limits the air entrainment to Zone 1 and Zone 2', resulting in increasing equivalence ratio of Zone 1 as shown in Figure 4.18. At the EoI period, the diffusion flame covers all of the spray and

no more air entrainment is allowed; therefore, the equivalence ratio stays constant until all of the mixture in Zone 1 moves into Zone 2′.

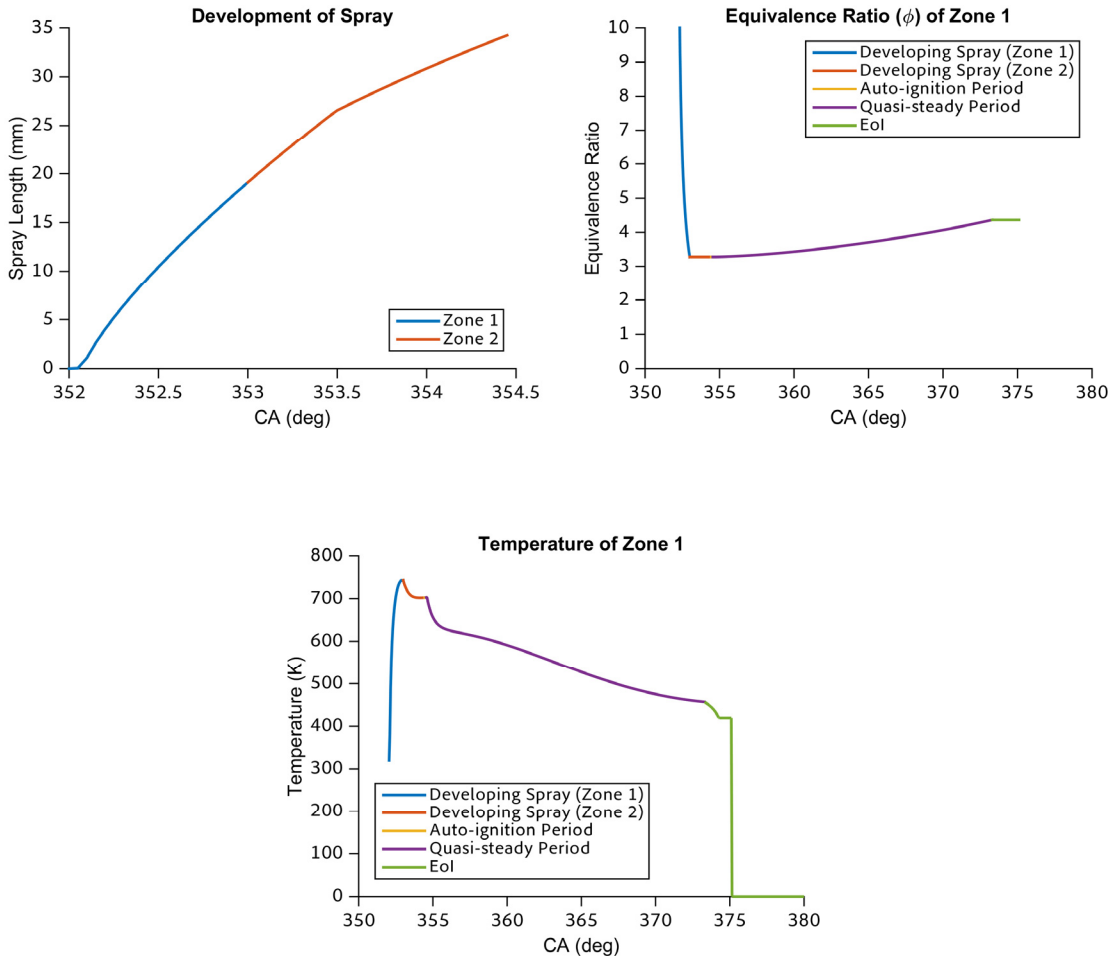

Figure 4.18 Variation of the development of spray, the equivalence ratio of Zone 1, the average temperature of Zone 1 with thermodynamic processes (Case 1)

The rate of air mass entrainment to Zone 1 decreases significantly during the quasi-steady period due to the smaller lift-off length as shown in Figure 4.21. The lift-off length is initially about 11 mm and the liquid length is about 19 mm. This sudden change in the available air entrainment surface area decreases the average temperature of Zone 1 rapidly while the lift-off length is decreasing

further. On the other hand, Zone 1 temperature decreases during the EoI period due to the evaporation of liquid-fuel. Once all of the available liquid fuel is evaporated, Zone 1 becomes isothermal. The sudden drop of Zone 1 temperature to zero occurs when Zone 1 does not exist anymore.

The fuel vapor and air mixture from the end of the liquid length penetrates further into Zone 6 and forms Zone 2. Air from Zone 6 continues to entrain into Zone 1 and Zone 2 until auto-ignition. The equivalence ratio of Zone 1 stays almost constant when the rate of injection is not changing significantly; hence, the equivalence ratio of Zone 2 decreases with the entrained air from Zone 6 as shown in Figure 4.19.

When the auto-ignition period ends, the rich combustion products of Zone 2 become Zone 4. Figure 4.19 shows that the average temperature of Zone 2 increases rapidly during the short period of auto-ignition.

In the quasi-steady period, the standing premixed flame of Zone 3 feeds Zone 4 and Zone 4 feeds the diffusion flame which is Zone 5. The mass of the rich combustion products in Zone 4 shows a parabolic behavior in this period (Figure 4.19). With the formation of the diffusion flame, the rate of air entrainment to Zone 1 and Zone 2′ (fuel vapor and air mixture formed beneath the liquid length during the auto-ignition period) will decrease due to shorter lift-off lengths therefore, the equivalence ratio of Zone 2′ will increase (Figure 4.20). The lift-off length is a strong function of Zone 6 temperature and density as expressed by Eqn. (3.59).

The rate of "fuel" consumption of Zone 5 is controlled by the mixing frequency and the amount of mass in Zone 4. The turbulent kinetic energy will increase due to the injection of fuel (Figure 4.22); hence, the mixing frequency will

increase. The parabolic shape of Zone 4 mass is a result of a balance between mixing frequency, Zone 4 mass, and lift-off length.

The fuel rich Zone 2′ mixture will feed into the standing premixed flame which is Zone 3. The equilibrium temperature of Zone 3 will decrease with the increased equivalence ratio of Zone 2′ (Figure 4.20).

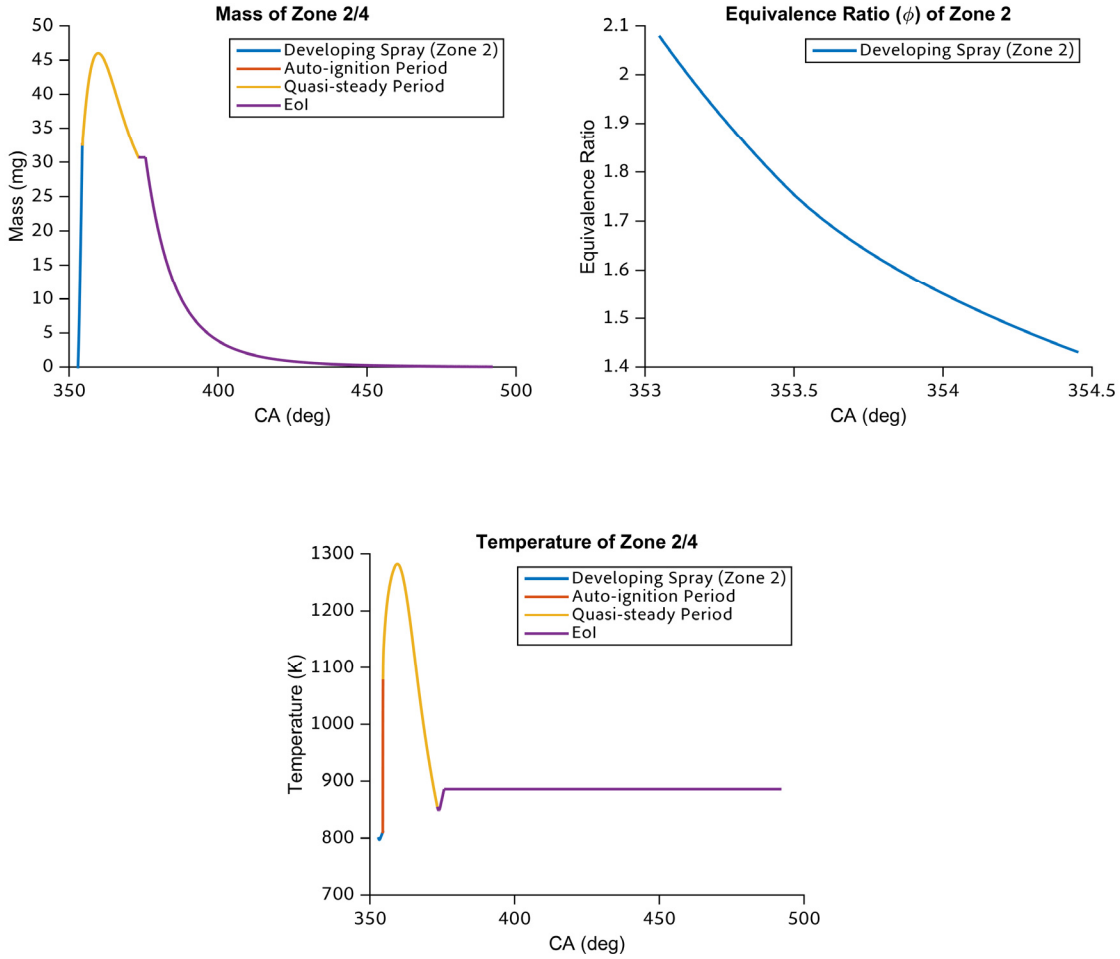

Figure 4.19 Variation of the mass, the equivalence ratio, and the average temperature for Zone 2 and later for Zone 4 with thermodynamic processes
(Case 1)

At the beginning of the quasi-steady period, the Zone 3 equilibrium temperature is relatively higher than the Zone 4 temperature and increases the average temperature of Zone 4 during this period. With the movement of the lift-off length towards the injector, the Zone 3 equilibrium temperature decreases significantly with entrainment of the highly rich Zone 2′ mixture; hence, it helps the Zone 4 temperature to decrease. However, the equivalence ratio of Zone 2′ decreases to about 5 in a short period of time after injector closing resulting in an increase of the Zone 3 equilibrium temperature. Straight lines of average temperature of Zone 2′ and the Zone 3 equilibrium temperature do not have a physical meaning in the late EoI period because, around 375° Zone 2′ is consumed fully and Zone 3 disappears simultaneously.

As described in Section 4.2.2, C_{diff} of the mixing frequency changes from 2.35 to 1.85 when the injector closes. This change of value in C_{diff} results in a discontinuity in mixing frequency as expected, similar to the sudden change of injector momentum as shown in Figure 4.21. However, the rate of decrease of diffusion flame equilibrium temperature is not comparable with the decrease of mixing frequency.

The mean flow kinetic energy increases with the kinetic energy of the fuel entering the cylinder which increases the turbulent kinetic energy simultaneously by the dissipation of mean flow kinetic energy as shown in Figure 4.22. When the injector is closed, the rate of change of mean flow kinetic energy is controlled by the production term and the blow-by mass past the piston rings as expressed by Eqn. (3.116) during the EoI period. A consequential decrease in the mixing frequency and the Zone 5 equilibrium temperature occur.

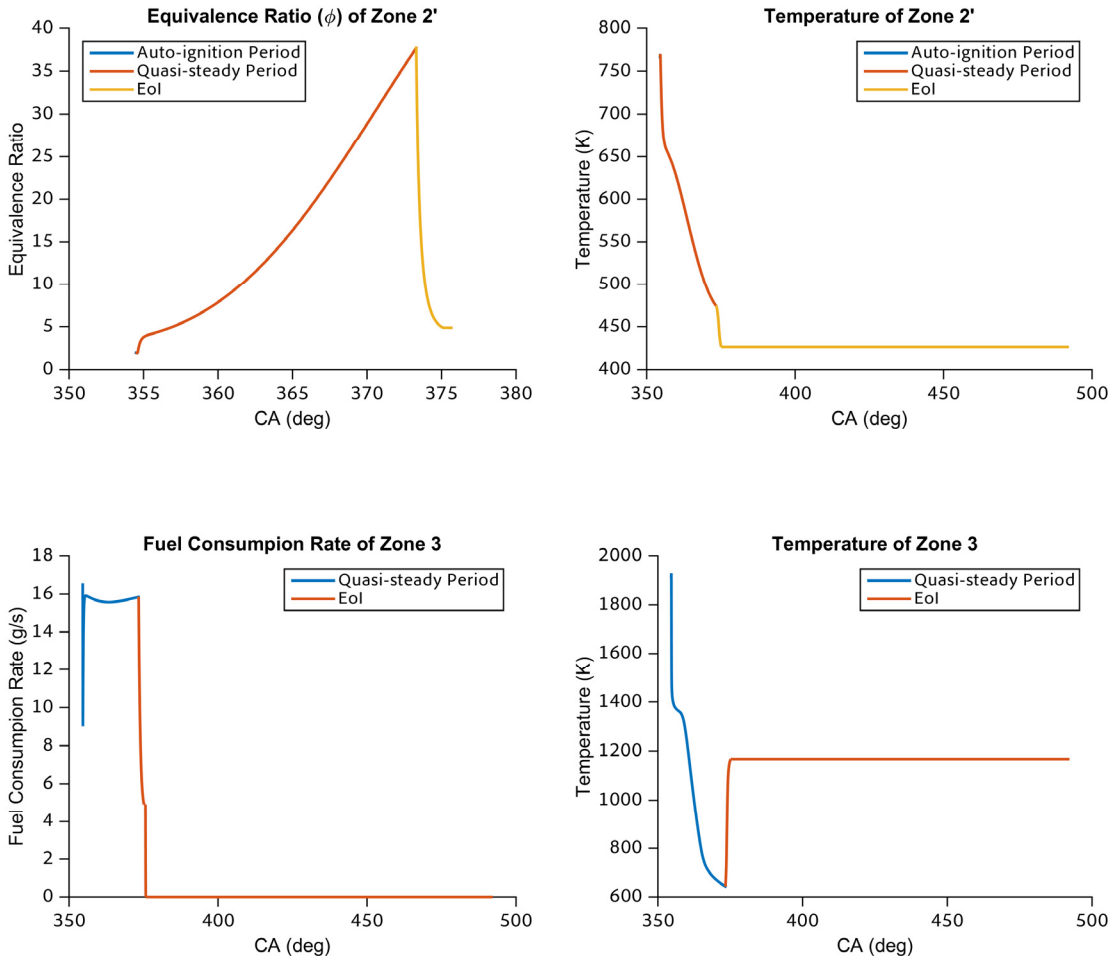

Figure 4.20 Variation of the equivalence ratio and average temperature for Zone 2′, and change in the "fuel" consumption rate and the equilibrium temperature of Zone 3 with thermodynamic processes (Case 1)

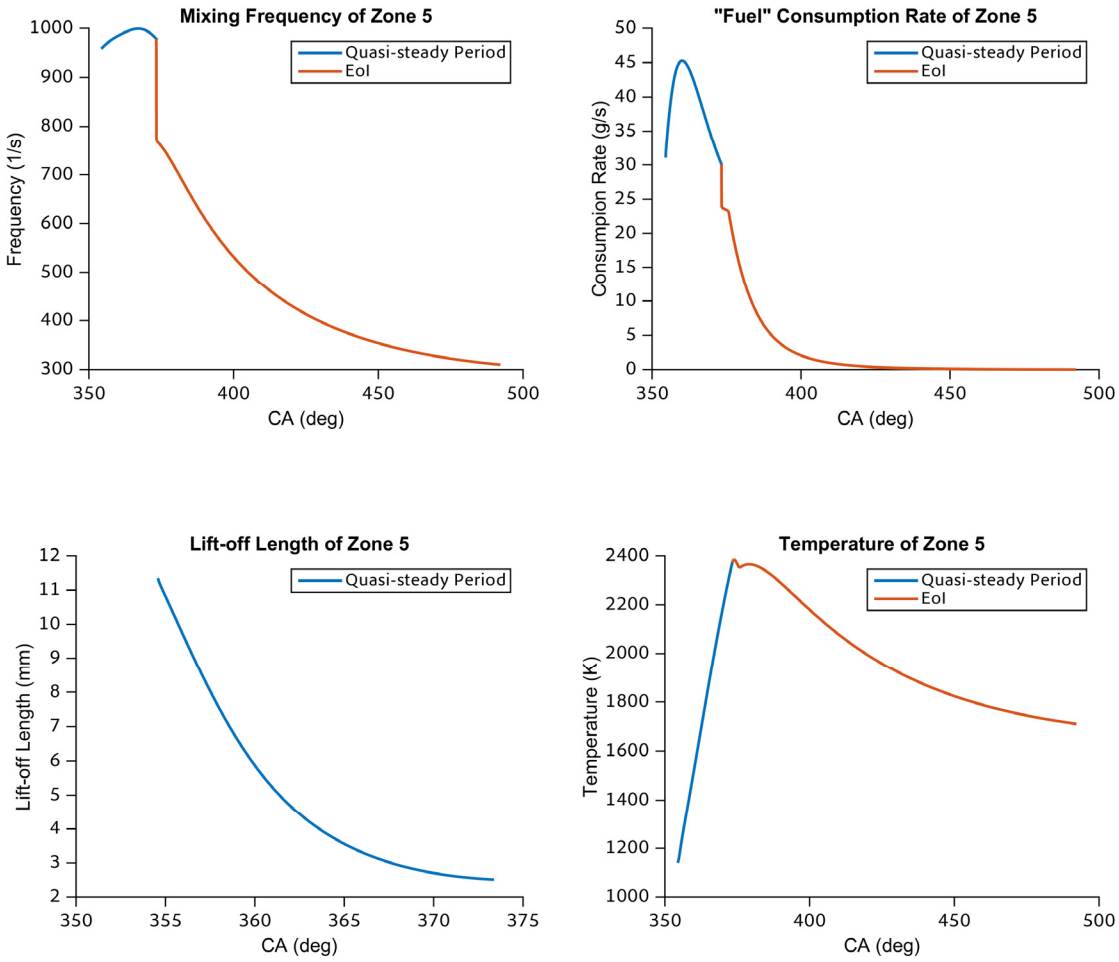

Figure 4.21 Variation of the mixing frequency, the "fuel" consumption rate, the lift-off length, and the equilibrium temperature of Zone 5 with thermodynamic processes (Case 1)

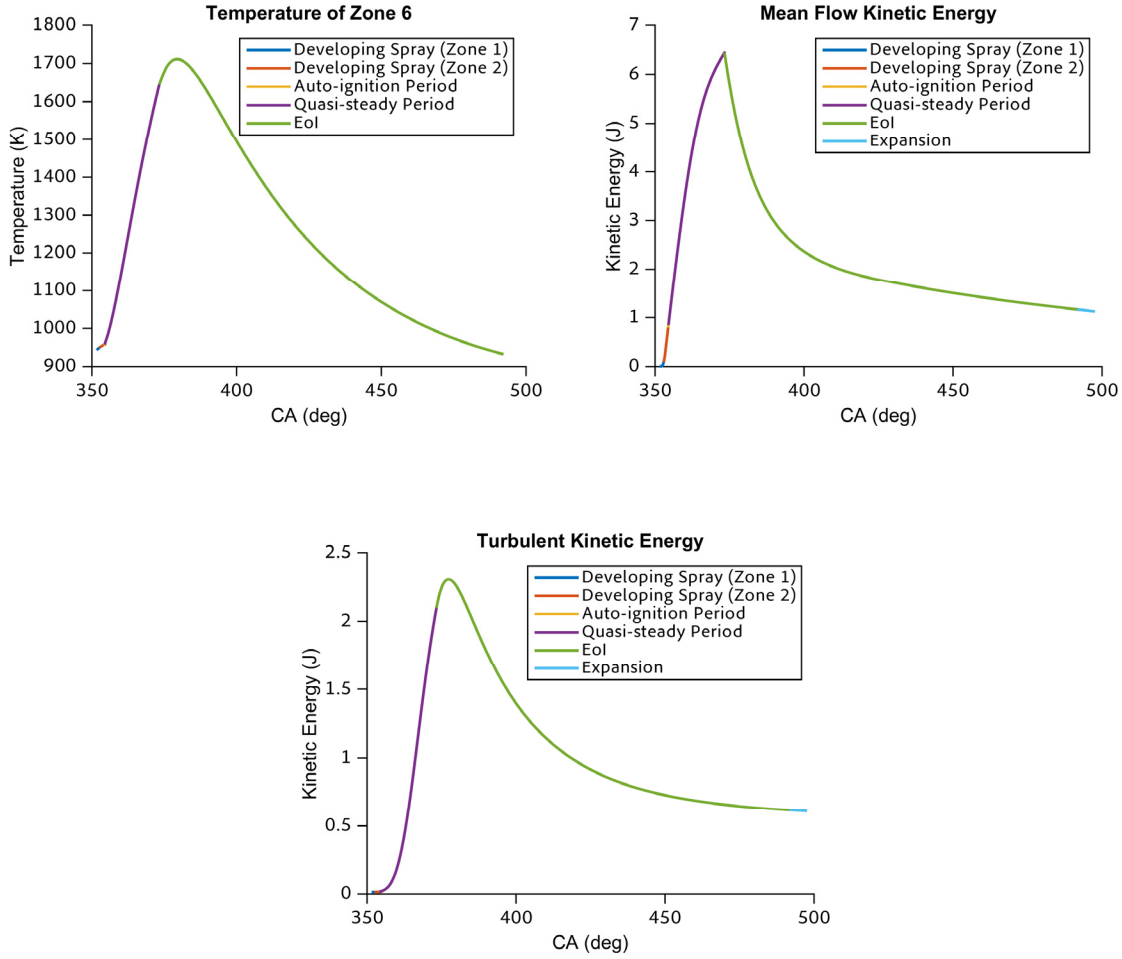

Figure 4.22 Variation of the average temperature of Zone 6, the mean flow kinetic energy and the turbulent kinetic energy with thermodynamic processes (Case 1)

The cylinder gas surrounding the spray throughout the evolution is Zone 6 which interacts with Zone 1, Zone 2, Zone 2', and Zone 5 depending upon the combustion stage as discussed in Sections 3.3.2 and 3.3.3. The combustion products of Zone 5 are assumed to diffuse only into Zone 6; hence, the average temperature of Zone 6 is highly dependent upon the Zone 5 equilibrium temperature as presented in Figure 4.21 and Figure 4.22.

4.5 Engine Model Sensitivity and Sources of Error

A sensitivity analysis of the quasi-steady engine model is made in this section between the input parameters and the key engine predictions considered during calibration. For brevity, only Case 1, 1243 rpm at 100% load (Table 4.2), is used to present the sensitivity of brake power, exhaust mass flow rate, *nimep*, *bmep*, *fmep*, PCP, and location of PCP. Table 4.8 presents the sensitivity of the output parameters to the deviation of input parameters from baseline values.

The compression ratio of every cylinder will not be the same due to the manufacturing tolerances of the parts. The PCP and the location of PCP are more sensitive to the variation in compression ratio than other parameters. Since *fmep* depends on PCP, it shows relatively higher sensitivity than other parameters considered.

The engine speed is one of the most accurate measurements taken from the engine since crank angle resolved data can give more information about the engine state. In order to understand the relative order of magnitude of change in output parameters, the engine speed was varied $\pm$50 rpm. Although the change in *bmep* is relatively small, the change in brake power is quite high due to the direct dependence on engine speed as Eqn. (3.148) expresses. Without changing manifold conditions, the engine was able to intake greater amounts of air when the engine speed is increased. With increased amounts of intake air, PCP dropped and shifted toward TDC.

The intake and the exhaust valve opening angles showed output variation of less than 0.5% most of the time when cam timings changed 3°. However, SOI

effects PCP and PCP location significantly. On the other hand, IVO, EVO, and SOI can be measured and actuated during engine operation very accurately.

The swirl ratio is used only in the initial estimate of the mean flow kinetic energy; therefore, it does not show any effect on output parameters.

The equivalence ratio is one of the key parameters that strongly affects power produced by the engine. In this case, a 5% increase in equivalence ratio results in a 5.32% increase in engine power. For actual engine operation, the amount of fuel injected every cycle is calculated and delivered precisely using the charge air mass flow rate measurement and electronic fuel pump system respectively.

The output parameters considered in this study did not show any significant sensitivity to the fuel temperature. However, emissions estimates that might be predicted using a future modification to the present engine model will be very sensitive to the variation of fuel temperature.

The injector rail pressure will affect the fuel flow rate into the cylinder. Depending upon the baseline EoI, PCP can increase or decrease since the equivalence ratio is fixed. However, PCP and location of PCP are more sensitive to the variation of rail pressure.

The results calculated based on a full cycle analysis are affected more by the intake port temperature and intake manifold pressure. On the other hand, the exhaust port temperature does not affect output parameters significantly because there is negligibly small back flow from the exhaust port into the cylinder during the gas exchange period. Moreover, there is not a turbocharger model attached to the engine model that can affect the air handling system. However, the variation

of exhaust manifold pressure will affect the exhaust mass flow rate; hence, the performance parameters.

The variation of cylinder surface temperatures and their respective areas show sensitivity of less than 0.4% in the output parameters considered.

Table 4.8 Percent change in key engine parameters when input parameters are varied

Input \ Output		Brake Power	Exhaust Mass Flow Rate	NIMEP	BMEP	FMEP	PCP	PCP Location
Compression Ratio	+ 0.3	-0.06%	-0.39%	0.03%	-0.06%	1.25%	1.72%	-1.73%
	- 0.3	0.04%	0.37%	-0.04%	0.04%	-1.15%	-1.59%	1.73%
Engine Speed	+ 50 rpm	4.50%	4.63%	0.26%	0.46%	-2.34%	-1.43%	-2.89%
	- 50 rpm	-4.48%	-4.66%	-0.26%	-0.48%	2.64%	1.71%	2.89%
IVO	+ 3°	-0.50%	-0.35%	-0.48%	-0.50%	-0.20%	-0.27%	0.00%
	- 3°	0.50%	0.24%	0.48%	0.50%	0.16%	0.23%	-0.58%
EVO	+ 3°	-0.40%	-0.32%	-0.38%	-0.40%	-0.04%	-0.06%	0.00%
	- 3°	0.36%	0.27%	0.34%	0.36%	0.03%	0.05%	0.00%
SOI	+ 1°	0.22%	0.50%	0.04%	0.22%	-2.46%	-3.39%	2.31%
	- 1°	-0.50%	-0.53%	-0.28%	-0.50%	2.60%	3.57%	-2.31%
Swirl Ratio	+ %5	0.00%	0.00%	0.00%	0.00%	0.00%	0.00%	0.00%
	- %5	0.00%	0.00%	0.00%	0.00%	0.00%	0.00%	0.00%
Equivalence Ratio	+ %5	5.32%	0.03%	4.94%	5.32%	-0.21%	-0.29%	-0.58%
	- %5	-5.26%	-0.01%	-4.87%	-5.26%	0.23%	0.31%	0.00%
Fuel Temperature	+ 5 K	-0.05%	0.00%	-0.04%	-0.05%	0.00%	0.00%	0.00%
	- 5 K	0.05%	0.00%	0.04%	0.05%	0.00%	0.00%	0.00%
Injector Rail Pressure	+ %5	-0.24%	-0.15%	-0.16%	-0.24%	0.92%	1.27%	1.73%
	- %5	0.39%	0.14%	0.31%	0.39%	-0.84%	-1.15%	-2.31%

Table 4.8 Percent change in key engine parameters when input parameters are varied (cont.)

Input \ Output		Brake Power	Exhaust Mass Flow Rate	NIMEP	BMEP	FMEP	PCP	PCP Location
Intake Port Temperature	+ 5 K	-2.03%	-1.44%	-1.91%	-2.03%	-0.25%	-0.34%	0.00%
	- 5 K	2.03%	1.47%	1.91%	2.03%	0.34%	0.47%	-0.58%
Exhaust Port Temperature	+ 50 K	-0.01%	-0.02%	-0.01%	-0.01%	-0.01%	-0.01%	0.00%
	- 50 K	0.01%	0.02%	0.01%	0.01%	0.01%	0.01%	0.00%
Intake Manifold Pressure	+ 0.1 bar	6.22%	7.10%	5.91%	6.22%	1.81%	2.49%	-2.31%
	- 0.1 bar	-5.10%	-5.20%	-4.86%	-5.10%	-1.67%	-2.30%	2.31%
Exhaust Manifold Pressure	+ 0.1 bar	-1.45%	-2.23%	-1.35%	-1.45%	-0.08%	-0.12%	0.00%
	- 0.1 bar	2.28%	4.04%	2.14%	2.28%	0.31%	0.42%	-0.58%
Cylinder Liner Temperature	+ 20 K	-0.41%	-0.31%	-0.38%	-0.41%	-0.03%	-0.04%	0.00%
	- 20 K	0.40%	0.31%	0.37%	0.40%	0.02%	0.03%	0.00%
Cylinder Head Temperature	+ 20 K	0.02%	-0.11%	0.02%	0.02%	0.01%	0.01%	0.00%
	- 20 K	0.24%	0.11%	0.23%	0.24%	-0.01%	-0.01%	0.00%
Piston Crown Temperature	+ 20 K	0.02%	-0.15%	0.02%	0.02%	0.01%	0.02%	0.00%
	- 20 K	0.24%	0.15%	0.22%	0.24%	-0.01%	-0.02%	0.00%
Cylinder Head to Bore Area Ratio	+ %5	-0.21%	0.01%	-0.20%	-0.21%	-0.04%	-0.06%	0.00%
	- %5	0.21%	-0.01%	0.20%	0.21%	0.04%	0.06%	0.00%
Piston Crown to Bore Area Ratio	+ %5	-0.27%	-0.04%	-0.26%	-0.27%	-0.05%	-0.07%	0.00%
	- %5	0.27%	0.04%	0.26%	0.27%	0.05%	0.07%	0.00%

In summary, for this case (1243 rpm, 100% load), the exhaust mass flow rate is most sensitive to uncertainty in the intake manifold pressure, followed by the engine speed and the exhaust manifold pressure, with a maximum variation of 7.10% for a variation of the intake manifold pressure by 10 kPa. The net indicated mean effective pressure is also most sensitive to uncertainty in the intake manifold pressure, in this case followed by the equivalence ratio and the exhaust manifold pressure, with a maximum variation of 5.91% for a variation of the intake manifold pressure by 10 kPa. The friction mean effective pressure is most sensitive to engine speed followed by SOI and intake manifold pressure with a maximum variation of 2.64% for a variation of 50 rpm (4%). The predicted brake mean effective pressure is a function of the predictions in both the net indicated mean effective pressure and the friction mean effective pressure. Thus, it is most sensitive to uncertainty in the intake manifold pressure followed by the equivalence ratio and the exhaust manifold pressure with a maximum variation of 6.22% for an uncertainty of 10 kPa in the intake manifold pressure. The predicted peak cylinder pressure is most sensitive to uncertainty in the crank angle of the start of injection followed by the intake manifold pressure and the compression ratio, with a maximum variation of 3.57% for an uncertainty of SOI of 1 CA°. The crank angle location of the peak cylinder pressure is most sensitive to the engine speed (+2.89% for a +4% change in rpm) followed by the intake manifold pressure (+2.31% for a +10 kPa change in intake manifold pressure), the rail pressure (advanced by 2.31% for a 5% decrease in rail pressure), and the SOI (again advanced by 2.31% for an uncertainty of SOI of 1 CA°).

The quasi-dimensional engine model was calibrated and validated using twelve engine operating points. All of the cases considered matched test cell

measurements accurately. Moreover, the behavior of the described zones was analyzed and shown to agree with the thermodynamic principles applied. With the confidence of the engine model, sensitivity analyses of the input parameters are reported for the key engine performance parameters.

The quasi-dimensional engine model relies on measurement data for both the simulation part and the validation part. Assumptions and sub-models are also the key ingredients of a precise model. All of these data sources and the assumptions can be sources of error for the simulation as depicted in Figure 4.23.

The governing equations for the combustion period depend upon accurate measurement of the fuel injection pressure or the fuel mass flow rate, SOI, the injector diameter, and the discharge coefficients of the nozzle.

The variation in the manufacturing tolerances of the piston, head, and connecting rod can result in compression ratio variations. For each of the cylinders, the compression ratio has to be measured and the measurement uncertainty should be reported.

In engine simulations, either a single cylinder model is run or a burn rate obtained from a single cylinder is applied to all of the cylinders. Therefore, the selection of a representative cylinder that is showing average behavior of all of the cylinders is necessary. For this purpose, high speed crank resolved cylinder pressure has to be logged from each cylinder. The cylinder pressure should be logged at least every 0.5° crank angle or better.

The measured cylinder pressure is AC coupled; i.e. capacitive coupling, meaning the DC signal component is filtered out and the remaining signal will have higher resolution. In other words, the shape of the signal and relative amplitude of the signal is known but the actual values of the signal are not known.

Once a pressure value is assigned to the signal at any given time, the entire signal can be quantified as the cylinder pressure signal. The anchoring or referencing of the signal is called pegging. There are two well-known pegging methods: 1) thermodynamic pegging, 2) pegging to a known pressure at a certain crank angle (e.g. BDC of compression or IVC). Further information can be found in the literature (Randolph, 1990; Brunt and Pond, 1997; Lee, Yoon and Sunwoo, 2008).

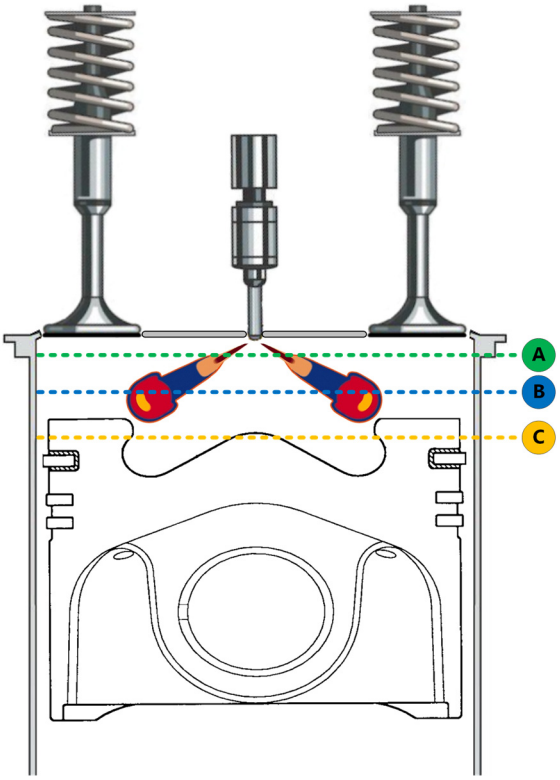

Figure 4.23 Quasi-dimensional engine model error sources. A, B, and C lines represent the swirl levels within the cylinder.

Another important error source related to the cylinder pressure measurement is the encoder error or the TDC shift. When we apply pegging to the obtained measurement signal, we obtain accurate cylinder pressures, but we

do not know the timing of this signal relative to the motion of the crankshaft. The peak cylinder pressure of the engine is set to a crank angle somewhere between 0.2-0.5° before TDC (BTDC) when the engine is motored, i.e. no firing, at medium speed. Further tuning can be achieved when the intake and exhaust manifold high speed crank angle resolved pressure data are available. Using the three pressures obtained for several engine operating points, the thermodynamic TDC shift relative to geometric TDC can be tuned to match with an engine model targeting emissions measurements or the combustion efficiency.

As shown in the present sensitivity analysis, model predictions can be affected slightly by the valve opening and closing angles. There are also the discharge coefficient and swirl levels associated with the valve lift. In this study, a generic discharge look-up table with respect to the valve lift had to be used due to unavailability of data. The author's main goal was to present a conceptual model that is based on experimental results and calibrate it with the available data set. The calibration coefficients may change with better data sets, but the concept will remain the same. In an ideal simulation, the discharge and the swirl coefficients have to be determined for both of the intake and exhaust valves in forward and reverse flow configurations using a flow bench.

In addition to all of these data-related error sources listed in this section, there are also model related error sources. The conceptual model developed in this study is based on experimental results from other researchers, and this conceptual model is presently described by a mathematical model that consists of a set of governing equations. These equations are discretized and solved numerically using a discretization scheme.

An example parameter as a source of error can be the swirl level formed due to the motion of the intake air within the cylinder. The swirl level changes inside the cylinder at each cross section as shown in Figure 4.23 (A, B, and C levels). Even when experimentally measuring a swirl level for an engine cylinder, we are not able to capture swirl variation within the cylinder. Hence, swirl is lumped into the terms for most of the governing equations; i.e. the heat transfer model and the turbulence model.

The time step used when solving the governing equations has an impact on the results as well. A first order forward finite difference scheme was implemented in the quasi-dimensional engine model. Figure 4.24 presents the change in *nimep* with varying time step. When the time step is decreased, the percent change in *nimep* gets smaller. Moreover, the execution time increases due to the smaller time step; for example, the model execution time is 32.5 minutes when a time step of 0.01 CA° is used. A time step of 0.05 CA° was used in this study due to its reasonable execution time and accuracy. Figure 4.24 presents the variation of engine model execution time for the engine operating points considered.

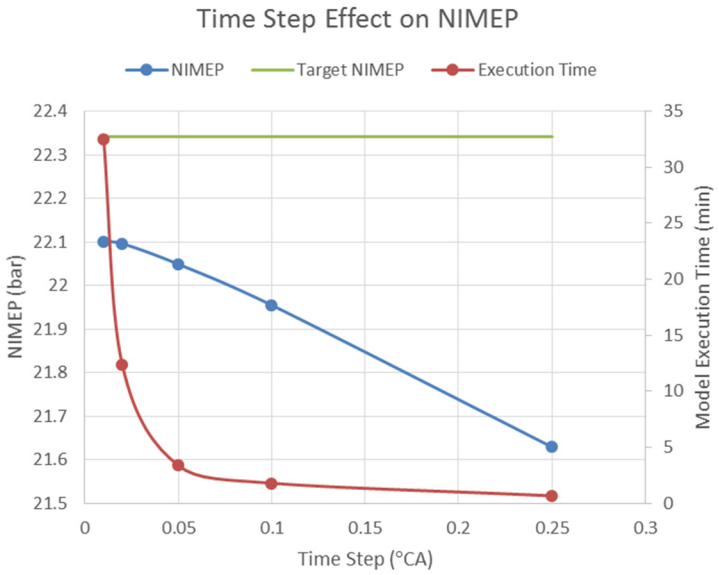

Figure 4.24 Effect of the quasi-dimensional engine model time step on the NIMEP and the model execution time

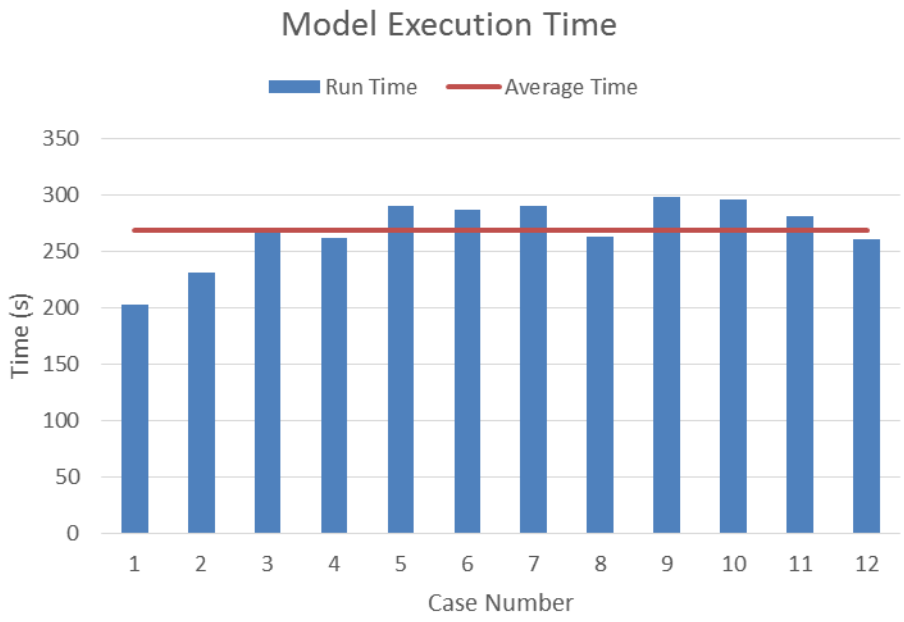

Figure 4.25 The execution time of the quasi-dimensional engine model for each operating point considered

Chapter 5

Conclusions and Recommendations

The University of Texas Fuel Economy Model was able to predict the fuel consumption of light-duty and heavy-duty vehicles operated in Texas. The model is capable of simulating a variety of vehicles, payloads, and traffic conditions. The vehicle model relies on drive cycles representative of real-world driving conditions and the coastdown coefficients for calculating total resistive force when the vehicle is travelling at a desired speed input according to the drive cycle.

The Environmental Protection Agency (EPA) publishes the coastdown coefficients for every light-duty vehicle sold in the US. However, there are no coastdown coefficients published by the EPA for heavy-duty vehicles. One objective of the present research was focused on obtaining coastdown coefficients for the representative heavy-duty vehicles on Texas roads.

Long stretches of level roadway is needed in order to conduct the coastdown experiments for heavy-duty vehicles. For a Class 8 truck loaded to 80,000 lb_m, about 11 km (7 mile) of road is needed to perform the experiments. However, it is very difficult to find such a long flat roadway. Therefore, a method for obtaining coastdown coefficients from data taken on a road of variable grade was developed.

The road load force for the 2008 Ford F150 calculated using the obtained coastdown coefficients using the present method is compared with the road load force calculated via the EPA's coastdown coefficients. Both of the road load forces are in good agreement. Therefore, the present method for removing the grade

effect from the coastdown tests provided confidence. Coastdown coefficients for the Class 7, Class 8 flatbed trailer, and the Class 8 box van trailer with wide-single low rolling resistance tires and aerodynamic devices are derived in this research for the three weight configurations considered: empty, "cubed-out", and weighted-out.

The grade of the road, the engine size, the traffic conditions, and the load of the vehicle are the important parameters that need to be addressed for the heavy-duty vehicle simulations. Therefore, the drive cycles used in a vehicle model should be representative of actual in-use driving conditions of the vehicle. In order to capture real driving conditions, 54 drive cycles with three different Class 8 trucks, three weight configurations, three traffic congestion levels, and two drivers were collected on a 43 km (27 mile) section of Interstate 35 through downtown Austin, Texas. The drive cycles obtained in this research include road grade and vehicle speed data with time.

The coastdown coefficients and the drive cycles obtained in this study were incorporated into the University of Texas Fuel Economy Model to estimate the fuel consumption of heavy-duty vehicles operating on Texas roads. The UT Fuel Economy Model predictions were in excellent agreement with the measured fuel economy for the cases considered. The vehicle model was able to follow the drive cycles very closely even in the presence of the maximum uphill grade of 5.5% and the minimum of -5.9%. The distance covered by the truck predicted by the UT Fuel Economy Model was short by only 85 meters for the 9:30 AM drive cycle while it was short by about 110 meters for the (essentially free-flow) 11:00 AM drive cycle. Compared to the total drive cycle length of 43.3 km (26.9 miles), the error in the distance is about 0.20 and 0.26%, respectively, for each simulation.

The final objective of this research was to develop a quasi-dimensional direct-injection diesel engine model that can be used to generate a fuel map to be used within the UT Fuel Economy Model rather than relying on the experimental fuel consumption maps. A full thermodynamic cycle simulation is necessary in order to capture the initial conditions at the intake valve closure (IVC) and predict the brake specific fuel consumption (*bsfc*). The compression, expansion, and gas exchange stages are modeled via zero-dimensional single zone calculations. On the other hand, the combustion stage is modeled based on in-cylinder images available in the literature and simulated using six different zones within the combustion chamber.

Sandia Livermore National Laboratory researchers obtained various images describing diesel spray evolution, spray mixing, auto-ignition, premixed combustion, diffusion combustion, soot formation, OH formation, and NOx formation via in-cylinder imaging technologies. Dec (1997) developed a conceptual model describing the evolution of diesel spray starting with the injection of fuel up to the quasi-steady state by using available images in the literature. The evolution of the diesel spray after the injector closing was left undescribed in this conceptual model because there was no clear in-cylinder image available during this period. In this study, a conceptual spray evolution after end of injection (EoI) was proposed and calibrated to capture diesel combustion evolution from the start of injection (SOI) up to the end of combustion (EoC).

In the present model, the combustion chamber is divided into six zones based on the conceptual model developed by Dec. The conservation of mass, the conservation of energy and the conservation of species equations were presented for each zone. The auto-ignition period (Zone 2) was modeled using a one-step

global reaction with unburned mass fraction dependence. On the other hand, the "fuel" entrainment rate to the diffusion flame (Zone 5) from the products of premixed combustion (Zone 4) is determined by a mixing frequency model which is determined by the turbulence model. The $k-\varepsilon$ turbulence model based on a zero dimensional energy cascade is implemented in this study due to its simple nature and computationally fast solution. The initial condition of the mean flow kinetic energy at IVC is estimated using rotational inertia of the cylinder contents whereas the turbulent kinetic energy is estimated by the total mass in the cylinder at IVC, the volumetric efficiency and the engine speed.

The quasi-dimensional engine model was calibrated using 12 available engine operating points from experimental data acquired from a 6 cylinder, 15 L turbocharged heavy-duty DI diesel engine by Southwest Research Institute (SwRI).

The evaporation model was calibrated using another set of data taken from a 12.9 L heavy-duty diesel engine because evaporation of the fuel does not emphasize its effect on the cylinder pressure during the ignition delay period for the modern high rail pressure equipped diesel engines. However, it was shown that the cylinder pressure is not sensitive to the evaporation calibration constant (k).

The diffusion combustion model was calibrated using the three calibration coefficients of the mixing frequency with the 12 engine operating points of the 15 L engine. The loss of the injector momentum was expected to result in a discontinuity in the model; hence, the diffusion combustion calibration coefficients were calibrated during the injection and post-injection periods. However, the

mean mixing velocity coefficients c_G and c_k were believed to be unaffected by this injector momentum change since the mean piston speed is constant for a given engine speed and the turbulent kinetic energy already considers injector nozzle kinetic energy. Therefore, only C_{diff} was re-calibrated for the diffusion combustion during the EoI period. Similar to the results of Barba *et al.* (2000), with $c_G = 1.8$ and $c_k = 0.1$ the quasi-dimensional engine model matched experimental cylinder pressure. C_{diff} was found to be 2.35 when the injector is open and 1.85 when the injector is closed for the mixing frequency model.

In this study, *fmep* (friction mean effective pressure) was derived using the high speed crank angle resolved cylinder pressure data (*nimep*, net indicated mean effective pressure) and the *bmep* (brake mean effective pressure) from brake torque. The four coefficients of the *fmep* relation were found using regression.

The calibrated quasi-dimensional engine model was validated using the 12 engine operating points used during calibration. The mean error of the engine power, the engine torque, *nimep*, *bmep*, *fmep*, the exhaust mass flow rate, the peak cylinder pressure (PCP), and the location of PCP were within 3% while the standard deviation was within about 5% except *fmep* and the PCP location. The standard deviation of *fmep* and PCP location are relatively higher than the other performance parameters considered due to their small values.

After gaining confidence in the quasi-dimensional engine model prediction capabilities by validating for the twelve engine operating points, the model was used to show features of the sub-models for each thermodynamic zone described in the model description. This leads to a better understanding of the evolution of the diesel spray and the effect of zonal parameters on the global parameters like

the cylinder bulk temperature and the cylinder pressure. Next, a sensitivity analysis of the quasi-dimensional engine model was presented in order to examine the effects of measurement uncertainty. It was found that the compression ratio, the engine speed, the SOI, the equivalence ratio, the injector rail pressure, the intake port temperature, the intake manifold pressure, and the exhaust manifold pressure are a few input parameters to which outputs are sensitive. However, the model predictions are most sensitive to only three of these measurement uncertainties: the intake manifold pressure, the engine speed, and the crank angle at the start of injection. Nevertheless, the predictions of the present model are quite accurate, as noted above.

Based upon the results of this research study, recommendations for future study include the simulation of the intake and exhaust volumes in addition to the simulation of sub-systems (i.e. the charge air cooler, the EGR cooler, and the EGR system) in order to increase the accuracy of the quasi-dimensional engine model. The developed conceptual combustion model can be used to optimize the performance of an engine or can be used for the selection of sub-systems during the development period. To this end, the state of the cylinder at IVC should be estimated accurately. Therefore, the turbocharger should be modeled along with the air handling systems. However, it is difficult to have generic engine sub-systems and a turbocharger that works with the air handling system because, sub-systems and the turbocharger are specific to a particular engine.

The commercially available diesel engine cycle simulation software can be used to implement the quasi-dimensional conceptual combustion model into a well-calibrated diesel engine model. The development of such a model requires access to the detailed technical drawings of the air handling systems and bench

testing of these systems in order to determine the discharge coefficients, the swirl, and the pressure drop. There are various types of turbochargers including WG (waste gated), VG (variable geometry), FG (fixed geometry), symmetric twin entry, and asymmetric twin entry. The efficiency maps of these turbochargers should be acquired and the modeling of the turbocharger can change depending upon the conditions under which the turbo maps are generated. The heat loss to the bearings and the cooling systems should be modeled as well, and the twin entry types can introduce extra complexity.

The cold start in diesel engines can result in various problems i.e. difficulty to start-up, hesitation, white smoke, and noise. The present quasi-dimensional DI diesel engine model can be used to capture the effect of cold start on noise.

The cylinder liner, the cylinder head, the piston wall temperatures and the manifold temperatures will be decreased from their baseline conditions (Case 1) for the three conditions described in the following table:

Table 5.1 Cold start and baseline conditions for the Case 1 engine operating point (A100)

	Fuel Temp. (K)	IMT (K)	EMT (K)	Liner Temp. (K)	Head Temp. (K)	Piston Temp. (K)
Baseline	320	312	600	400	372	523
Cold A	273	273	273	273	273	273
Cold B	265	265	265	265	265	265
Cold C	255	255	255	255	255	255

The noise level of the internal combustion engine is a consequence of pressure waves of varying characteristics i.e. exhaust noise, induction noise, combustion noise etc. (Soroka and Chien, 1969). However, in diesel engines the vast majority of the engine noise is due to the combustion. Russell and Haworth

(1985) showed that the maximum rate of heat release rate correlates well with the engine noise. Under colder conditions the quasi-steady engine model shows that the peak apparent heat release rate (AHRR) is much higher than the baseline; hence, under cold start conditions the engine noise is expected to be higher than the baseline. However, the peak AHRR values are close to each other for the three cases considered. Investigation of the auto-ignition period will help understand the noise due to combustion in Zone 2.

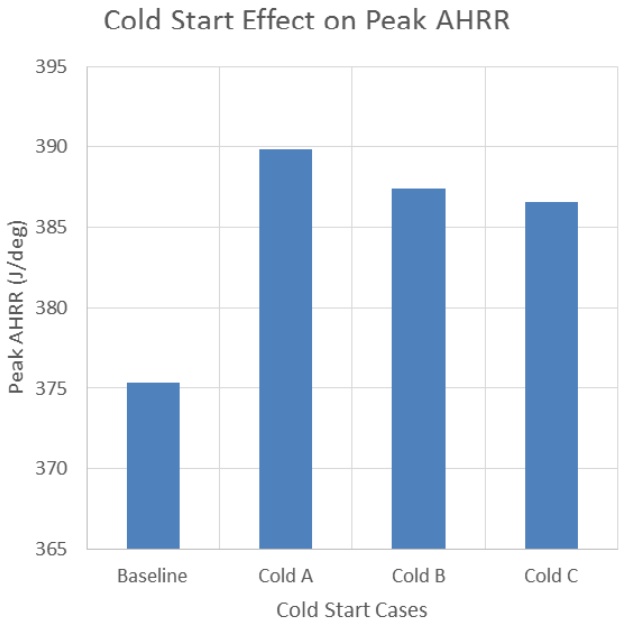

Figure 5.1 Cold start effect on the peak apparent heat release rate (AHRR)

The auto-ignition of the premixed fuel-vapor air mixture (Zone 2) becomes more difficult with colder conditions and the ignition delay model used in the quasi-steady DI diesel engine model is capable of capturing the cold start effect as shown in Figure 5.2.

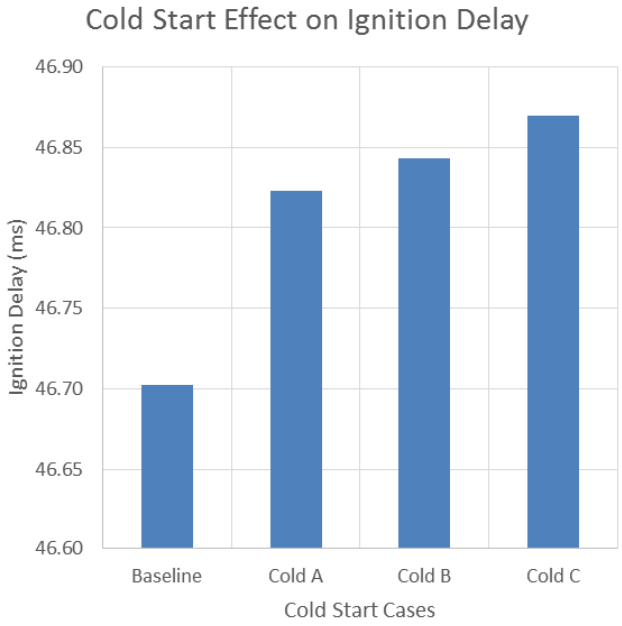

Figure 5.2 Cold start effect on the ignition delay

With increasing ignition delay period, Zone 2 accumulates more mass under colder conditions as shown in Figure 5.3. Hence, the auto-ignition and the diffusion flame has access to the higher amount of "fuel" which results in the higher rate of heat release.

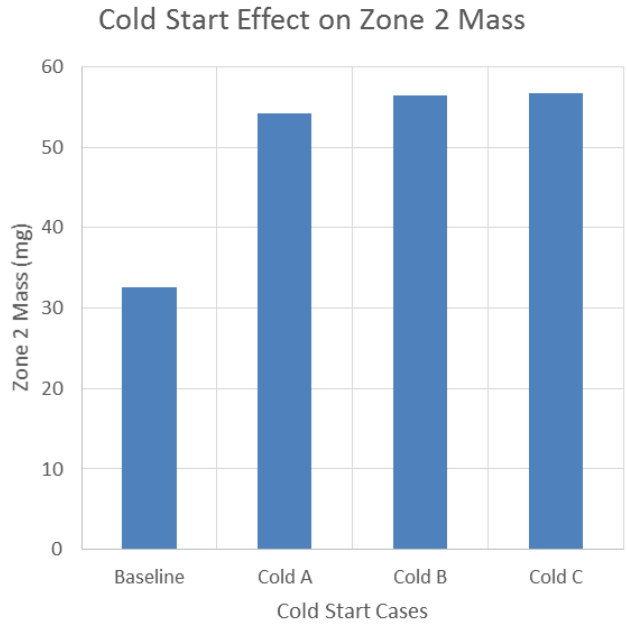

Figure 5.3 Cold start effect on the total mass of Zone 2

The injector rail pressure stays constant during cold start cases; therefore, the rate of liquid-fuel mass injection does not change significantly. Under colder operating conditions, the formation of the diffusion flame is delayed due to the delayed ignition time and longer combustion duration for Zone 2. Hence, the equivalence ratio of Zone 2' is leaner under colder conditions as shown in Figure 5.4, which produces higher equilibrium temperatures for Zone 3 as shown in Figure 5.5. The quasi-dimensional DI diesel engine model is capable of tracking species within each zone. However, the combustion products of Zone 2, Zone 3, and Zone 5 are determined using the equilibrium calculations. The soot estimation of the quasi-dimensional DI diesel engine model for the cold start conditions are shown in Figure 5.8. Higher soot emissions were expected with colder ambient conditions; however, model predicts a decrease in soot emission. With a soot model it would be possible to estimate the effect of cold start on the initial soot

formation using chemical kinetics in Zone 3. Moreover, experimental emissions measurements is needed for the validation of results which was not available during this research study.

With more complete combustion in Zone 3, the equilibrium temperature of Zone 5 will decrease as shown in Figure 5.6 and with a NOx model it would be possible to estimate the cold start effect on the NOx formation in the diffusion flame. The quasi-dimensional DI diesel engine model predicts a decrease in NOx with colder ambient conditions as expected as shown in Figure 5.9. Nevertheless, combustion products were estimated using chemical equilibrium instead of a model that is utilizing chemical kinetics and test cell emissions measurement was not available during this study. The reduced reaction mechanism with 29 species and 52 reactions (Patel, Kong and Reitz, 2004) is replaced with an n-heptane-n-butanol-PAH mechanism developed by Wang *et al.* (2013), 76 species and 349 reactions, for the estimation of soot and NOx emissions in the quasi-dimensional DI diesel engine model.

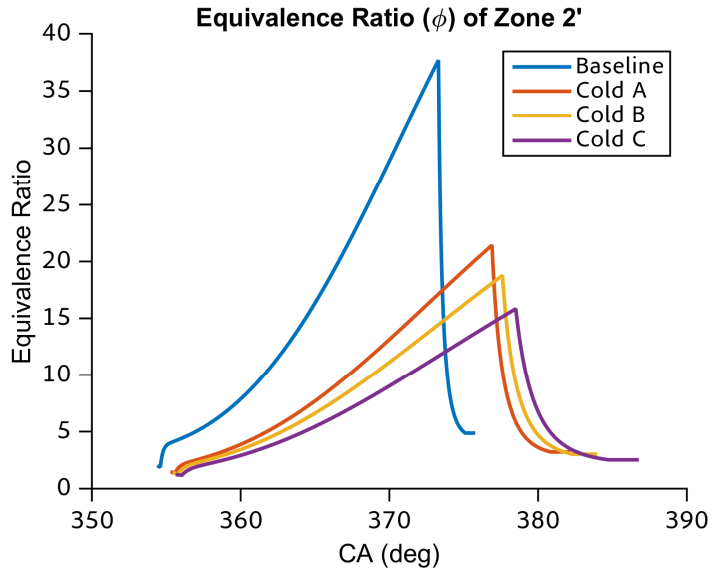

Figure 5.4 Cold start effect on the equivalence ratio of Zone 2′

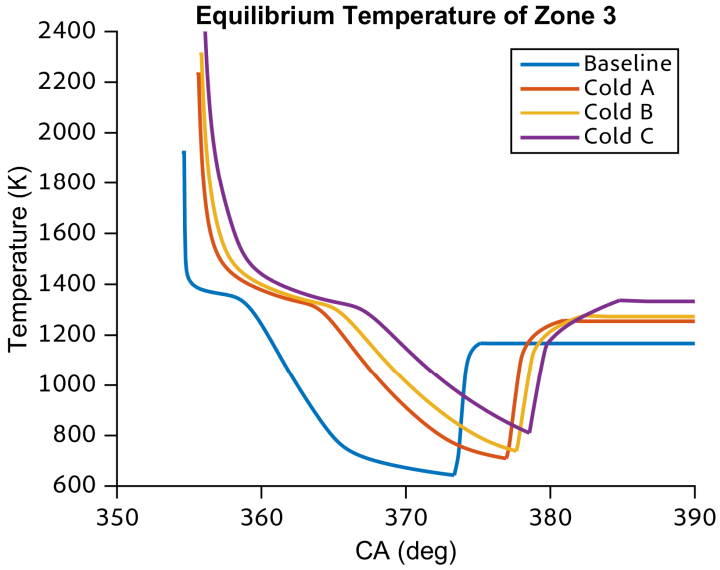

Figure 5.5 Cold start effect on the equilibrium temperature of Zone 3

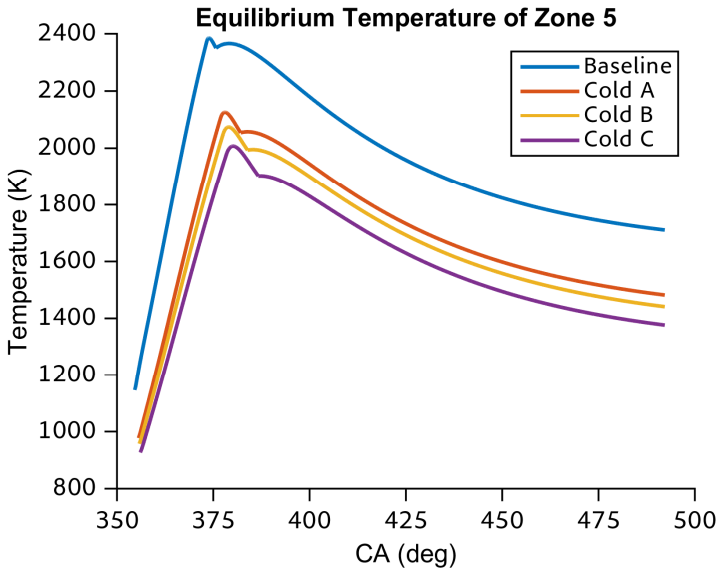

Figure 5.6 Cold start effect on the equilibrium temperature of Zone 5

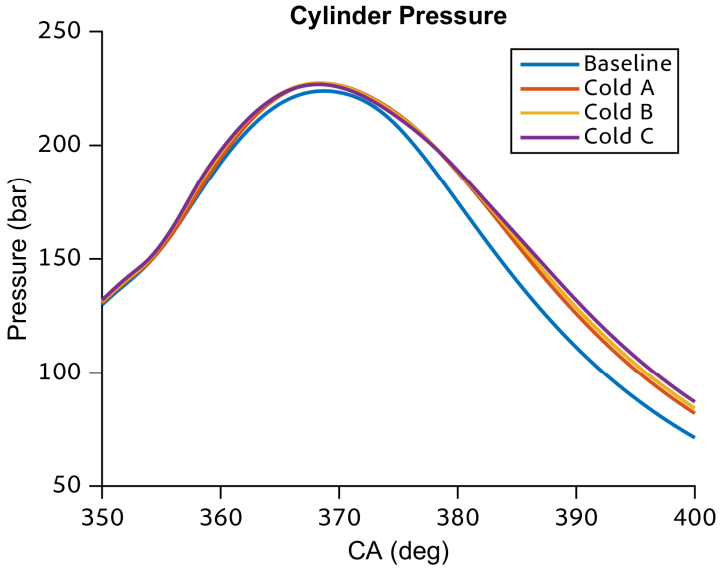

Figure 5.7 Cold start effect on the cylinder pressure

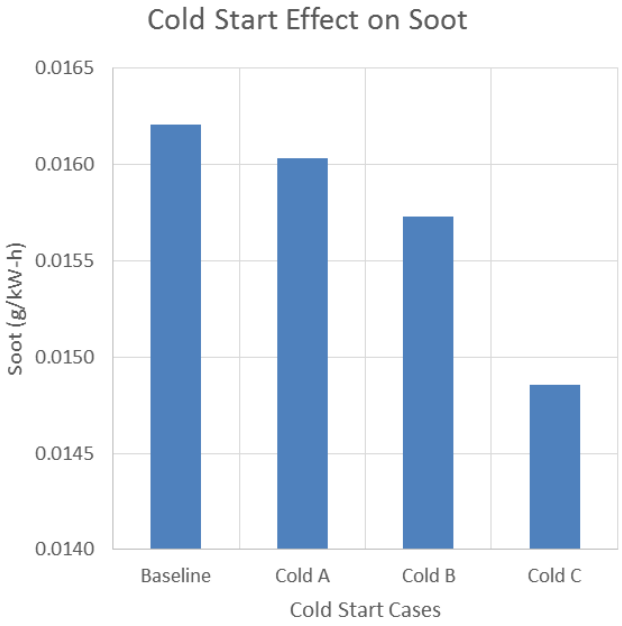

Figure 5.8 Quasi-dimensional DI diesel engine model soot estimation for cold start conditions

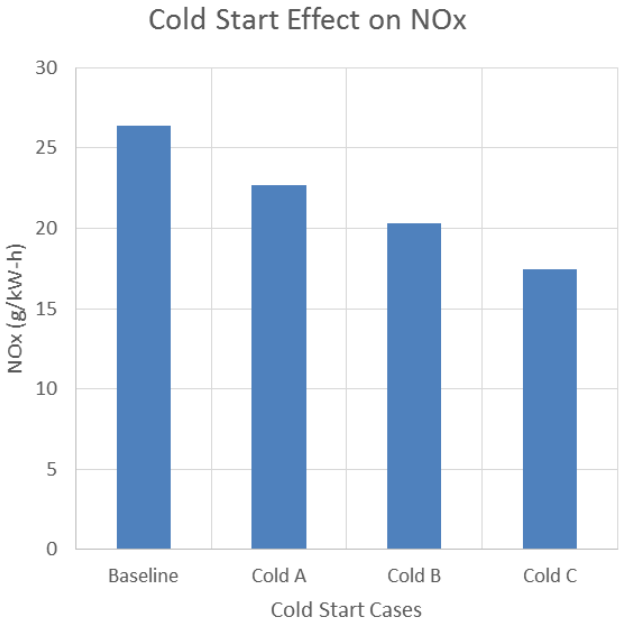

Figure 5.9 Quasi-dimensional DI diesel engine model NOx estimation for cold start conditions

The quasi-steady model is capable of capturing the effect of injection pressure on the soot production due to the interaction of the diffusion flame, Zone 5, and Zone 1 and Zone 2′. The lift-off length controls the portion of the diffusion flame that is interacting with Zone 1 and Zone 2′. With higher injector rail pressure, the diffusion flame is pushed away from the injector nozzle; hence, the lift off length increases as shown in Figure 5.10. The high rail pressure is 200 bar more than the baseline rail pressure and the low rail pressure is 200 bar less than the baseline rail pressure.

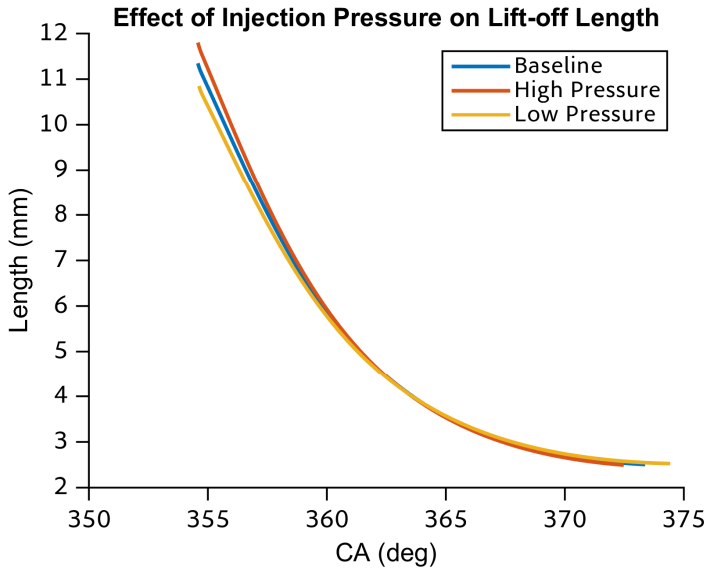

Figure 5.10 Injection pressure effect on the lift-off length

The diesel combustion can be assumed to be lean complete combustion in air and the brake specific carbon dioxide ($bsCO_2$) can be estimated from the brake specific fuel consumption using the following global reaction and the relation between *bsfc* and $bsCO_2$:

$$C_xH_yO_z + \frac{\left(x+\frac{y}{4}-\frac{z}{2}\right)}{\phi}O_2 + 3.764\frac{\left(x+\frac{y}{4}-\frac{z}{2}\right)}{\phi}N_2 \longrightarrow$$
$$xCO_2 + \frac{y}{2}H_2O + 3.764\frac{\left(x+\frac{y}{4}-\frac{z}{2}\right)}{\phi}N_2 + \left(\frac{1}{\phi}-1\right)\left(x+\frac{y}{4}-\frac{z}{2}\right)O_2 \quad (5.1)$$

$$bsCO_2\left[\frac{g_{CO_2}}{kW-h}\right] = bsfc\left[\frac{g_{fuel}}{kW-h}\right]\cdot x\left[\frac{moles_{CO_2}}{mole_{fuel}}\right]\cdot\frac{MW_{CO_2}}{MW_{fuel}}\left[\frac{g_{CO_2}}{mole_{CO_2}}\frac{mole_{fuel}}{g_{fuel}}\right] \quad (5.2)$$

where, *MW* is the molecular weight of corresponding species. Quasi-dimensional DI diesel engine model *bsCO₂* is compared with the *bsCO₂* calculated using test cell *bsfc* and n-Heptane as fuel as shown in Figure 5.11.

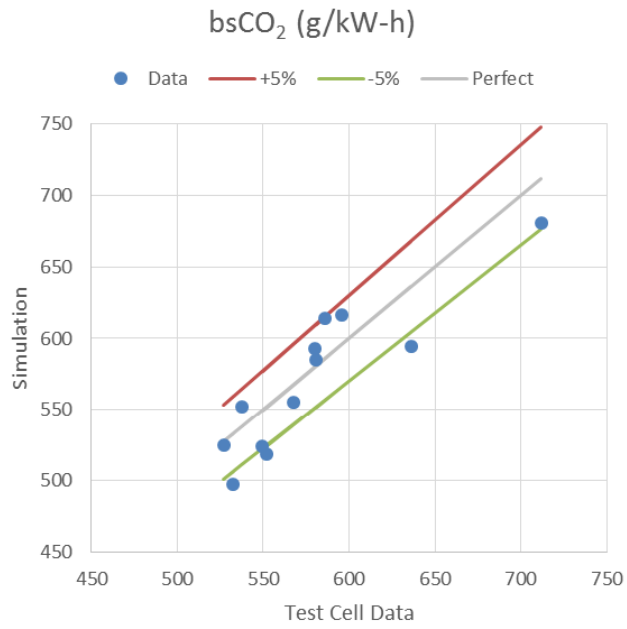

Figure 5.11 Brake specific carbon dioxide estimation by assuming fuel as n-Heptane (nC_7H_{16})

The effect of different piston shapes can be modeled by adding a piston wall zone to the quasi-steady DI diesel engine model. The piston wall zone should interact with Zone 5 and Zone 6. This new zone requires the surface area of the spray and the interference area between the spray and the piston surface. The effect of the swirl on the surface area of the spray and the interference area should be modeled; hence, the effect of the piston shape on the emissions can be estimated.

The surface temperatures of the head, the liner, and the piston were assumed to be constant using the literature values in this research. A cylinder wall temperature solver can be added to the model in order to determine the wall temperatures of head, liner, and piston. Therefore, the effects of the piston coatings on the diesel engine performance and the diesel engine out emissions can be estimated with a piston wall zone. The quasi-dimensional DI diesel engine model would be ideal to study the effect of thermal properties and thickness of coatings.

Appendix

Case 1: 1243 rpm, 100% load

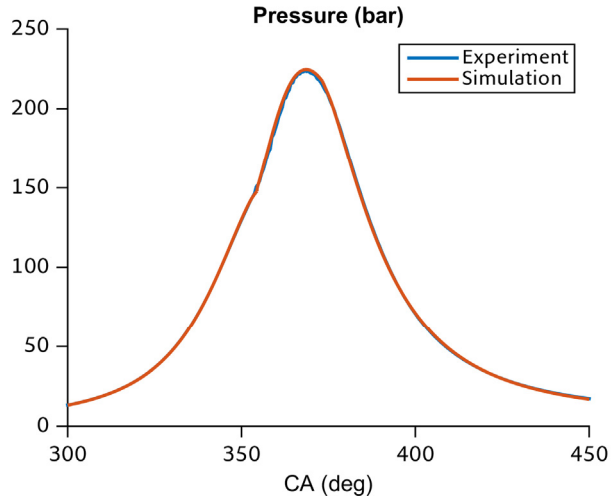

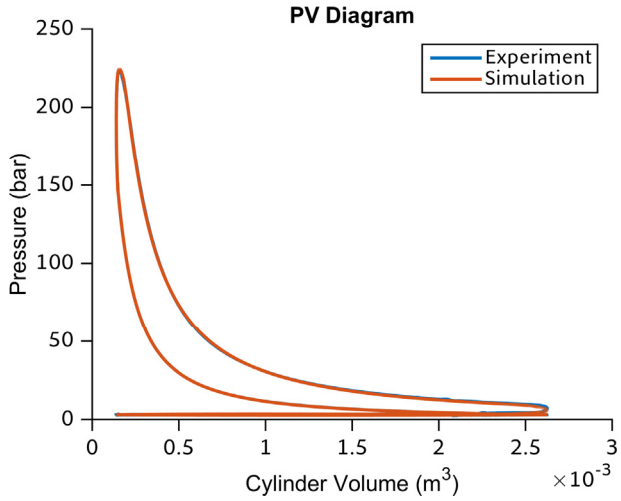

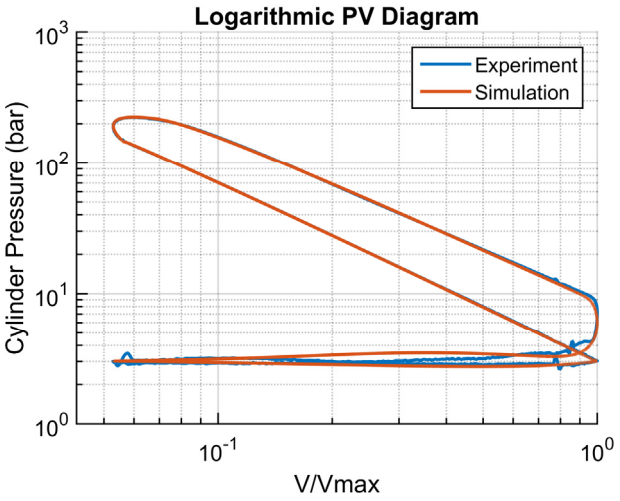

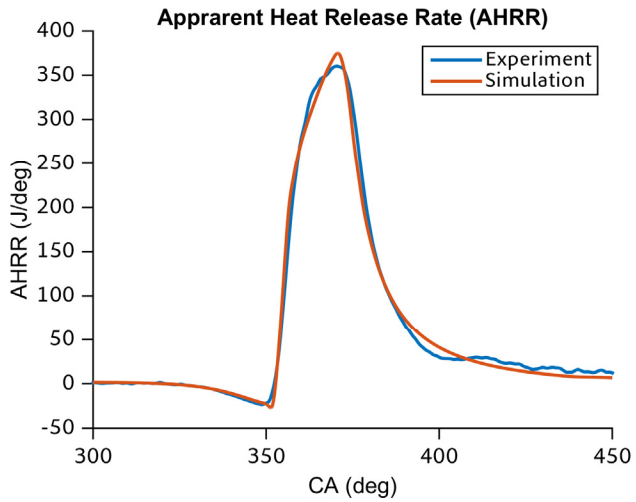

Case 2: 1243 rpm, 75% load

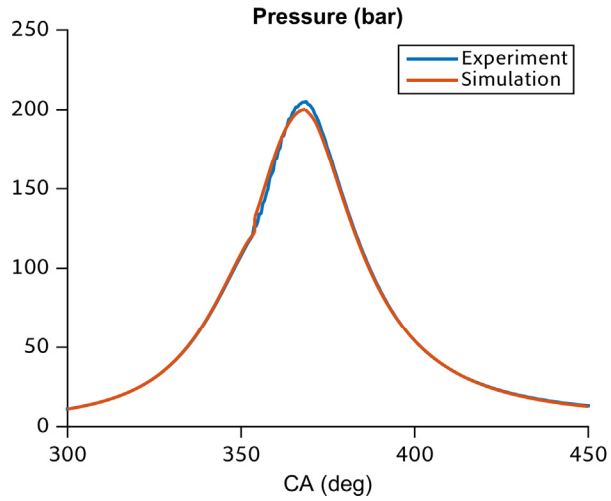

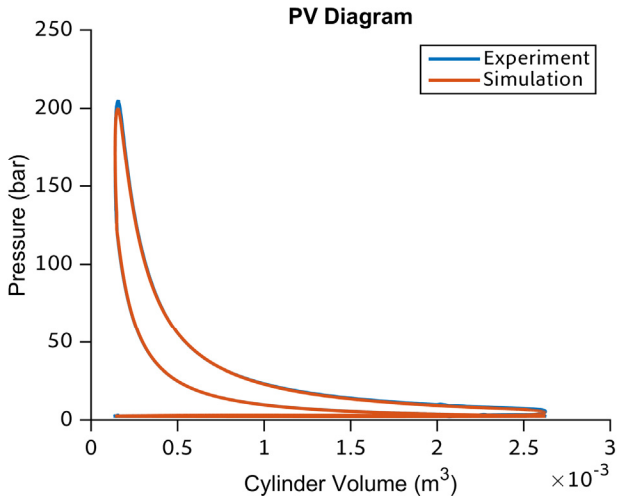

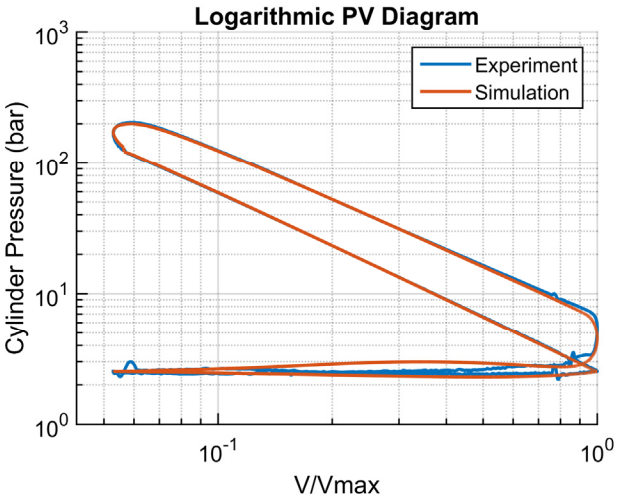

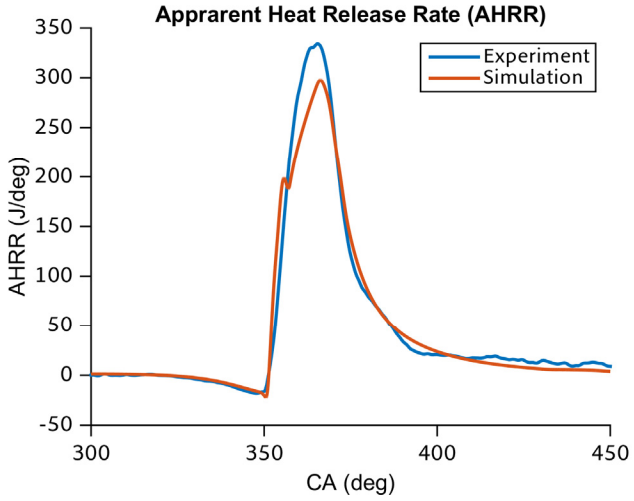

Case 3: 1243 rpm, 50% load

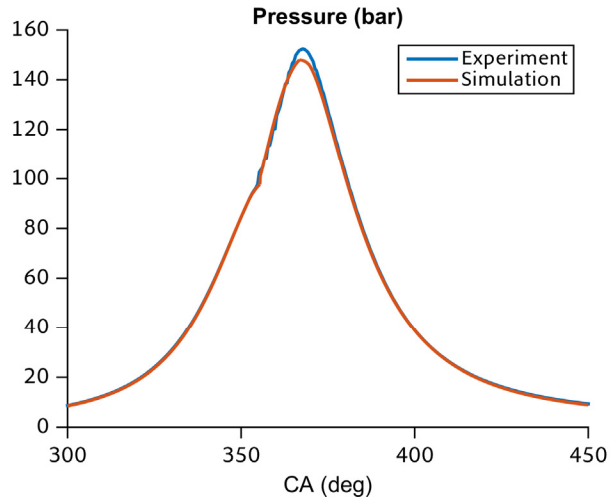

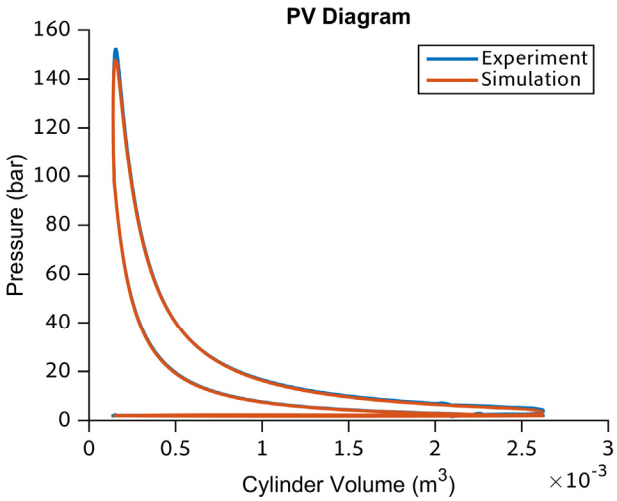

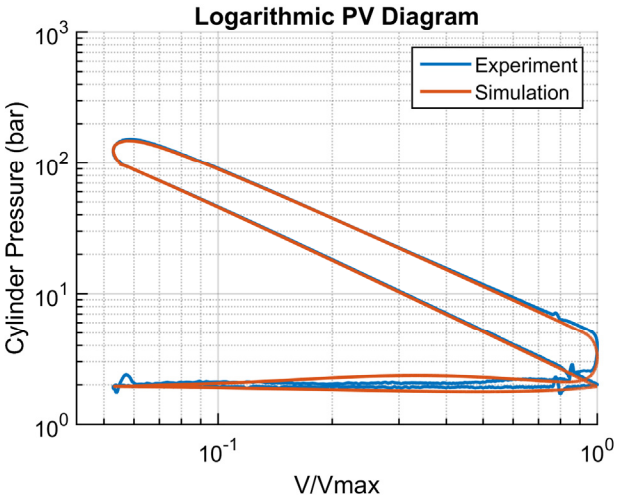

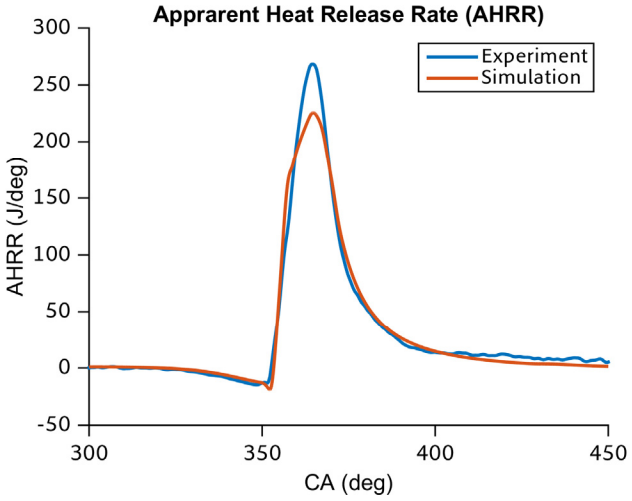

Case 4: 1243 rpm, 25% load

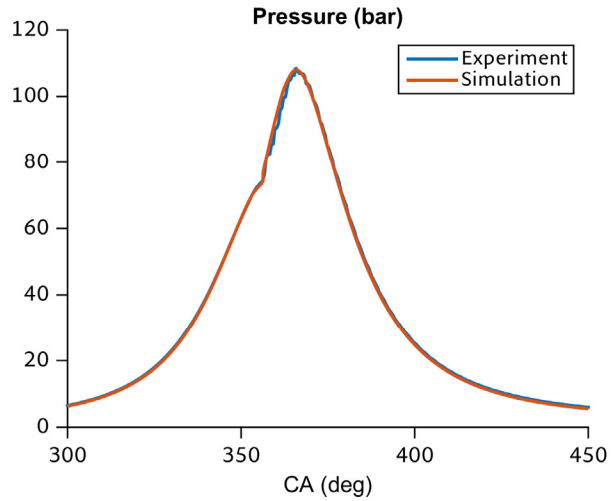

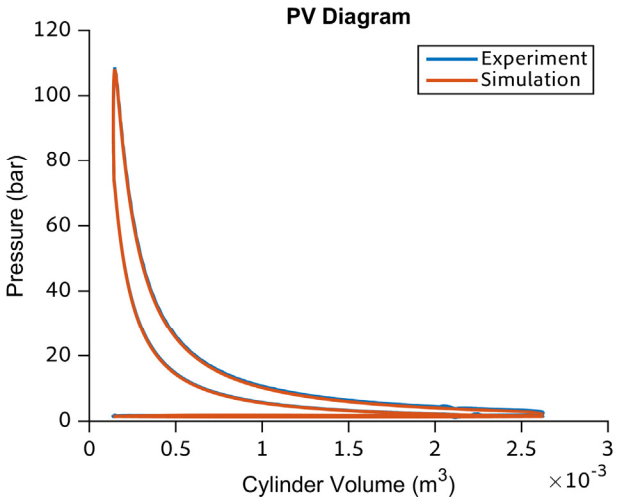

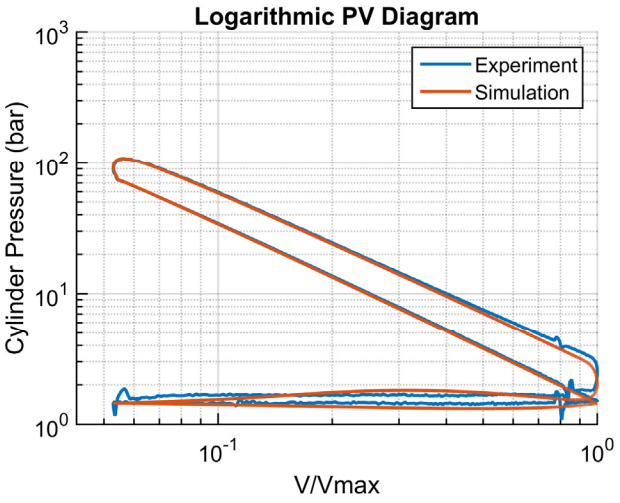

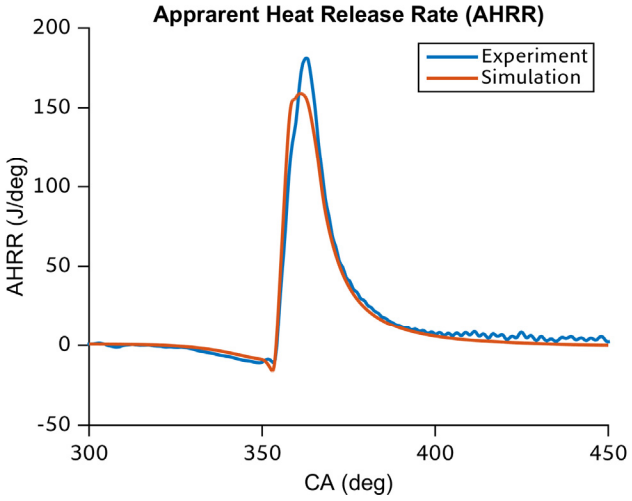

Case 5: 1539 rpm, 100% load

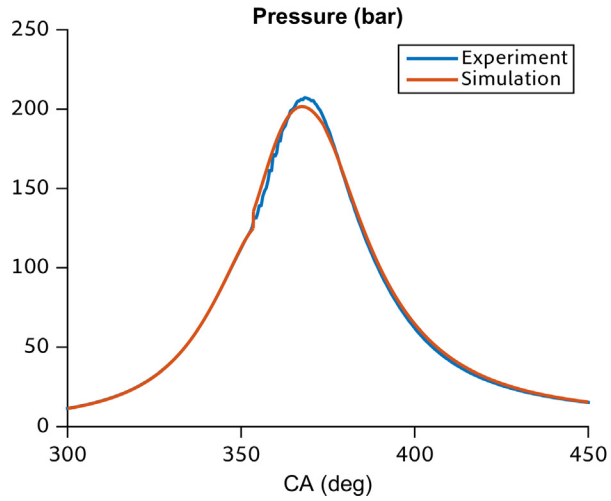

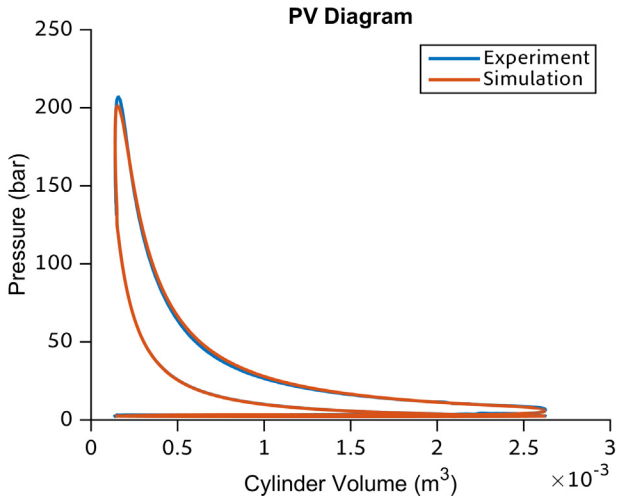

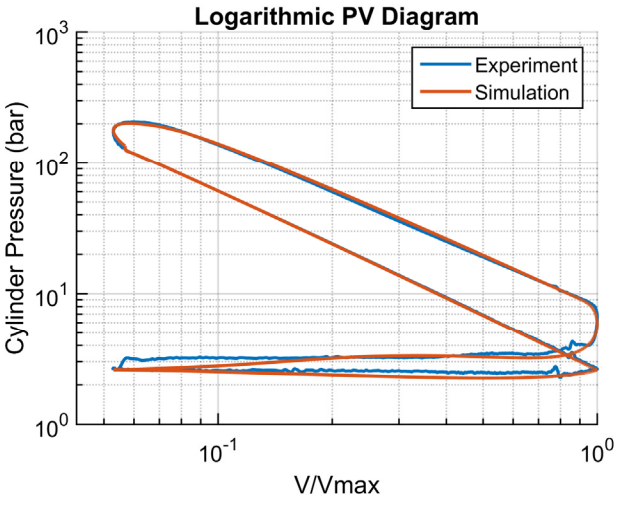

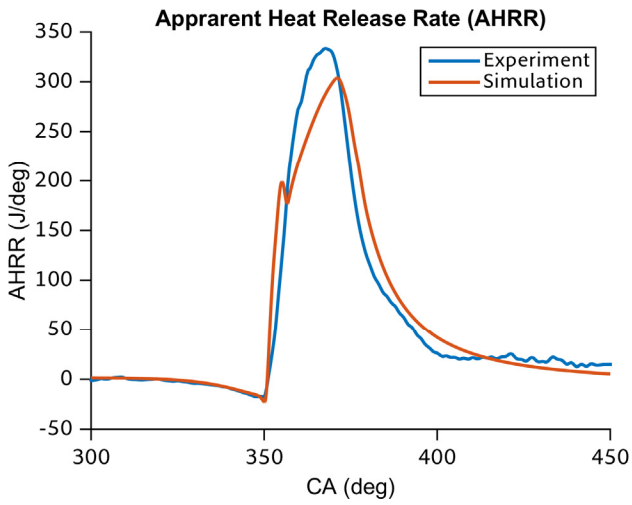

Case 6: 1539 rpm, 75% load

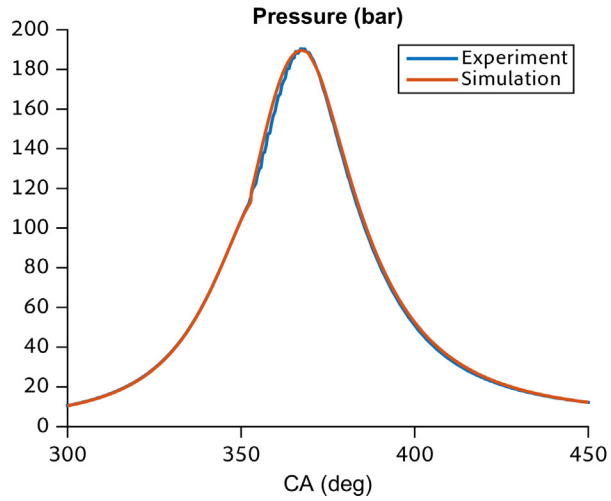

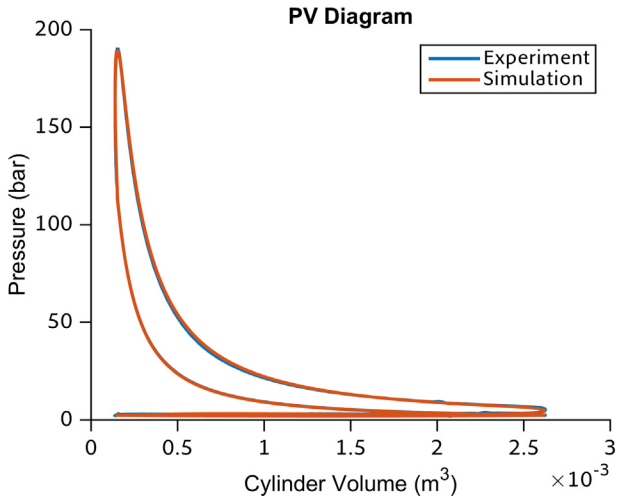

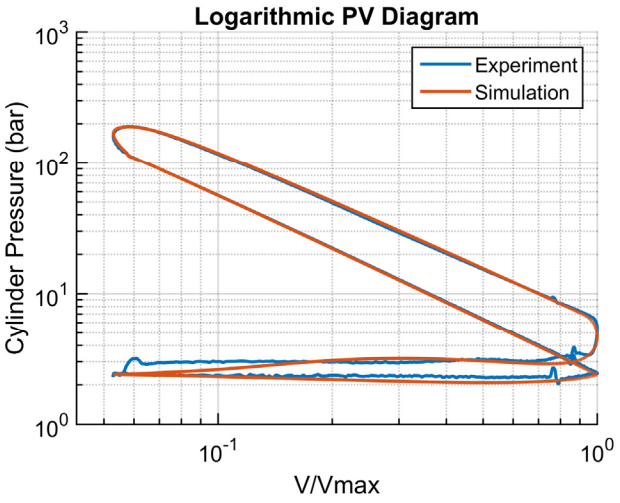

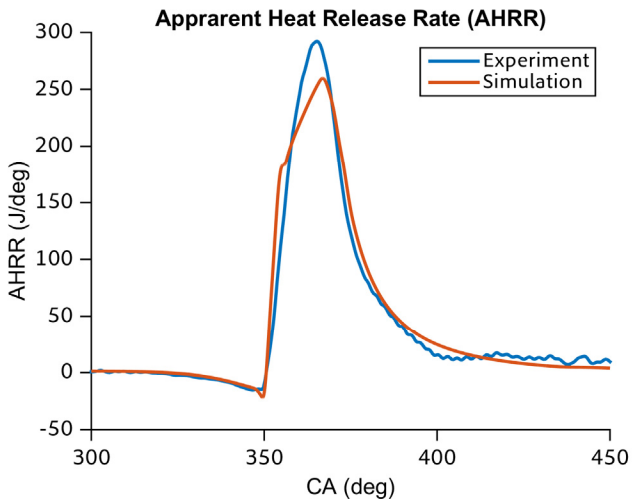

Case 7: 1539 rpm, 50% load

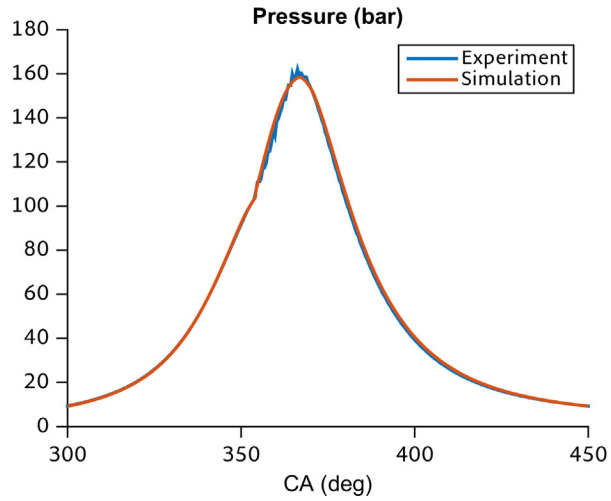

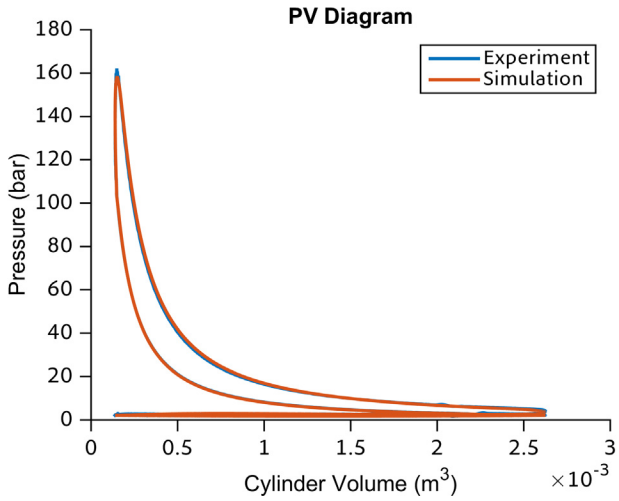

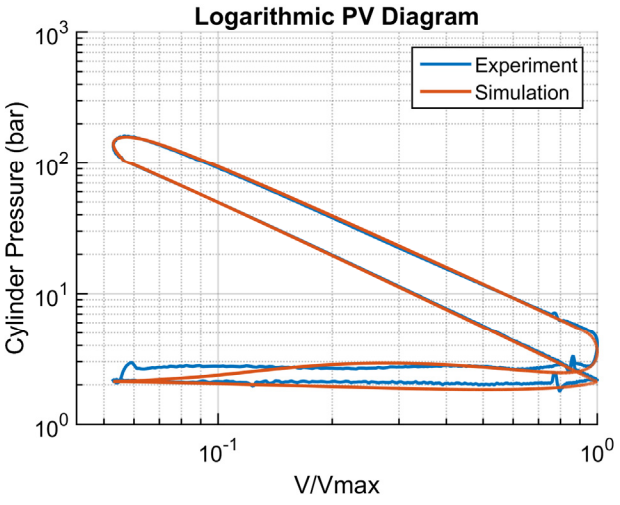

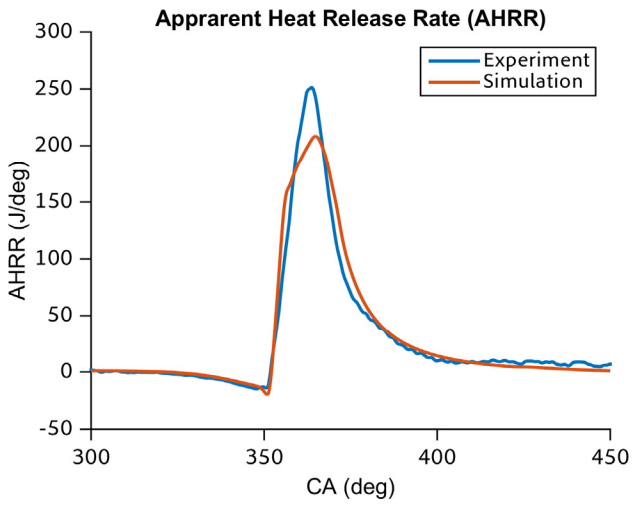

Case 8: 1539 rpm, 25% load

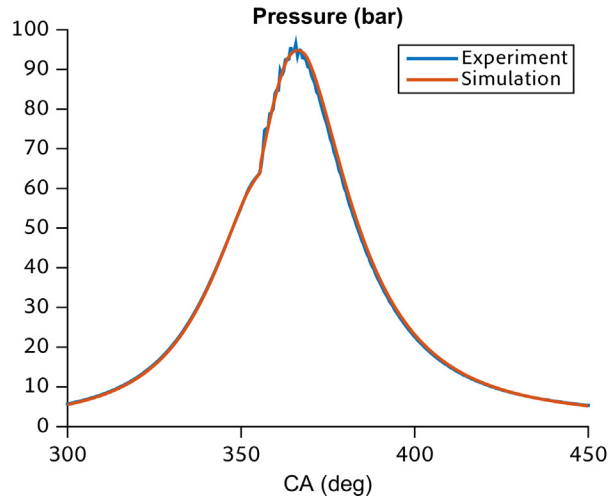

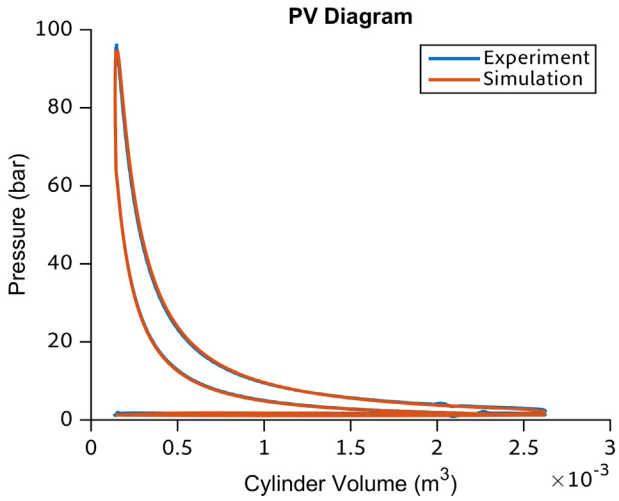

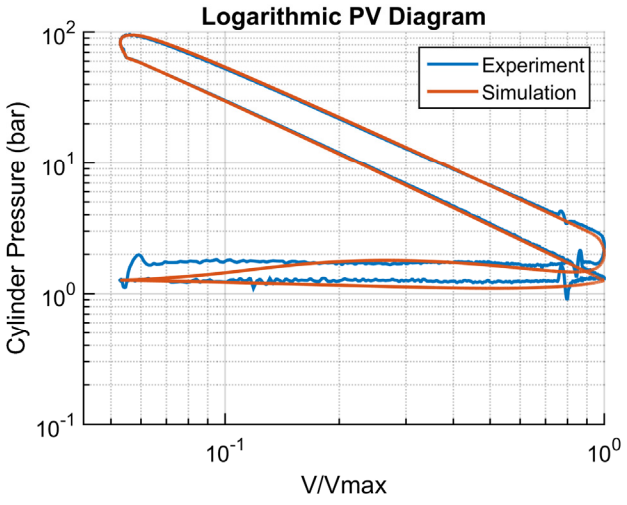

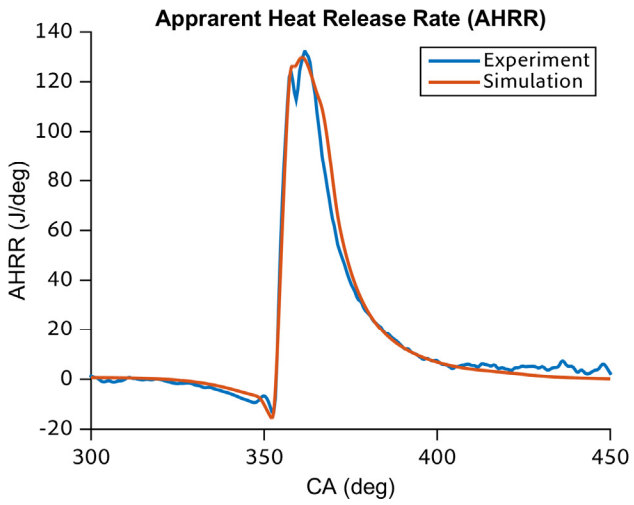

Case 9: 1830 rpm, 100% load

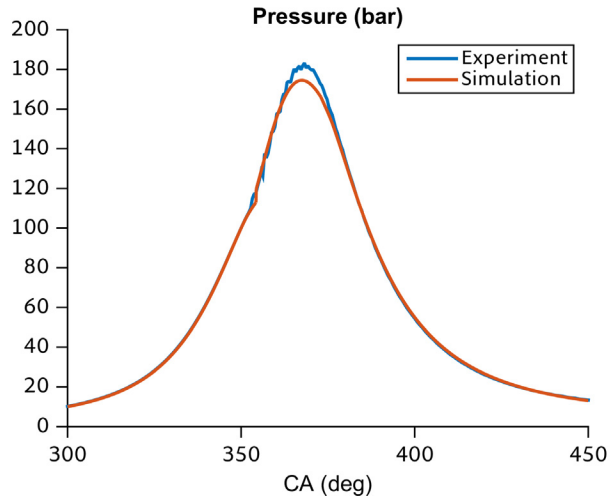

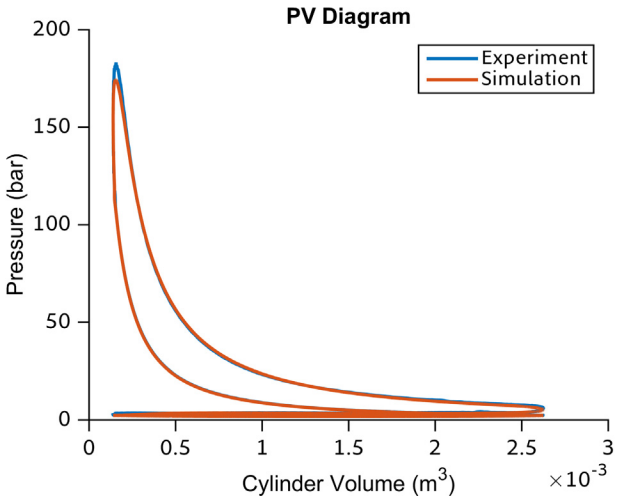

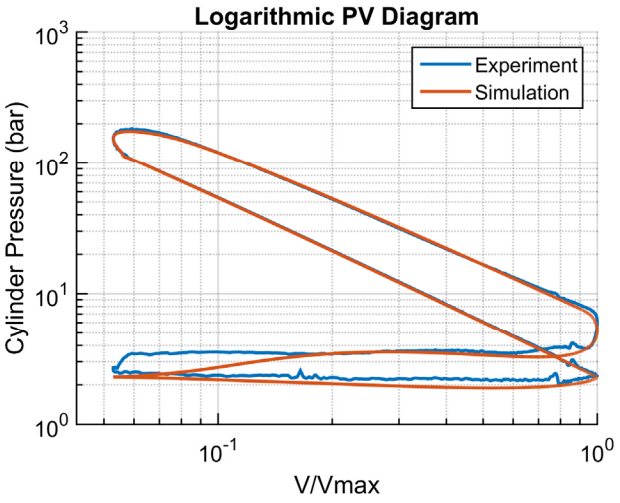

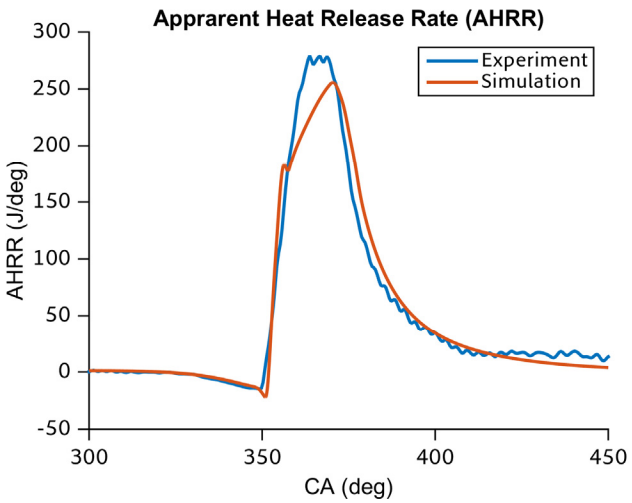

Case 10: 1830 rpm, 75% load

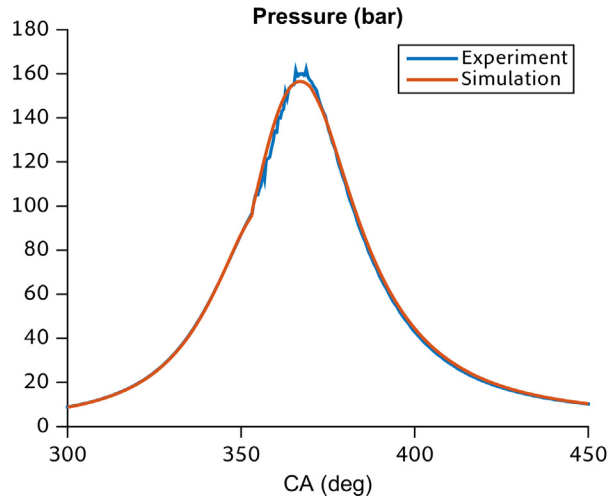

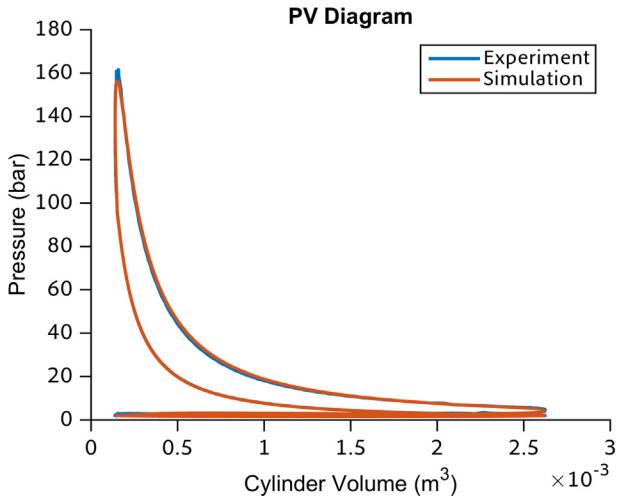

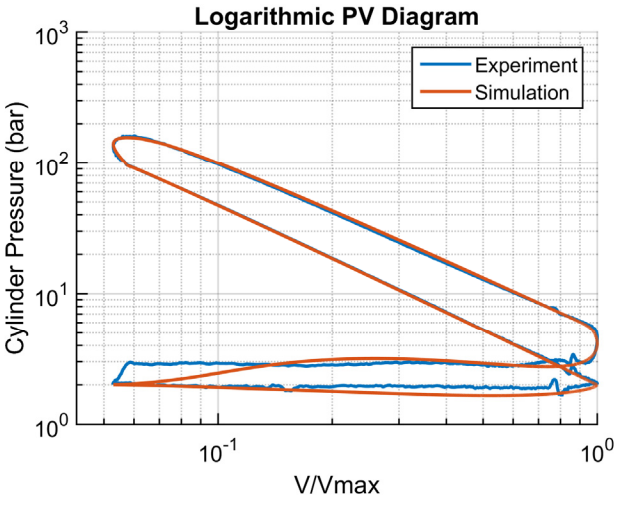

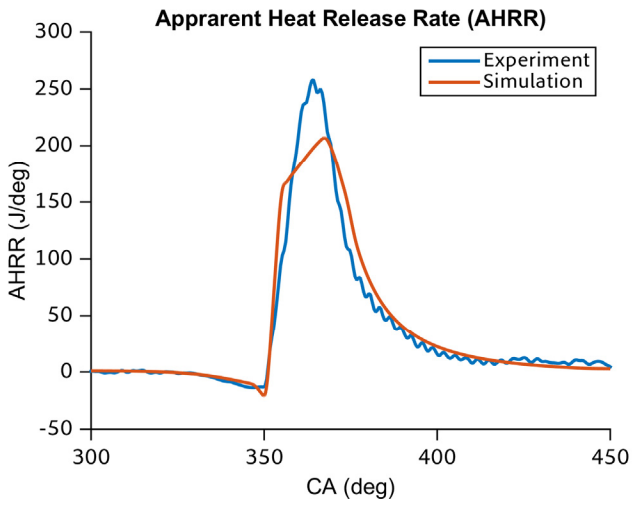

Case 11: 1830 rpm, 50% load

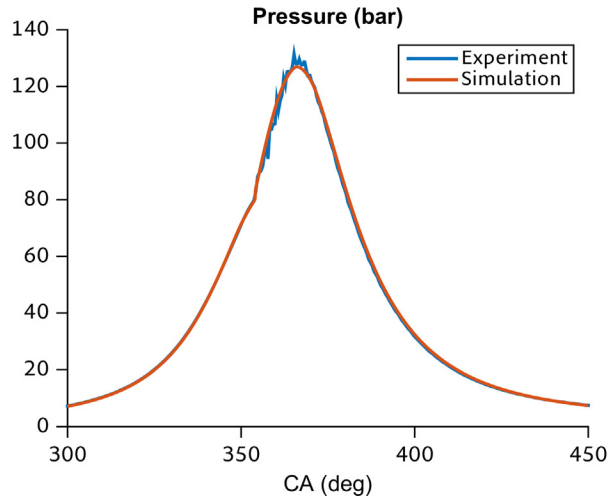

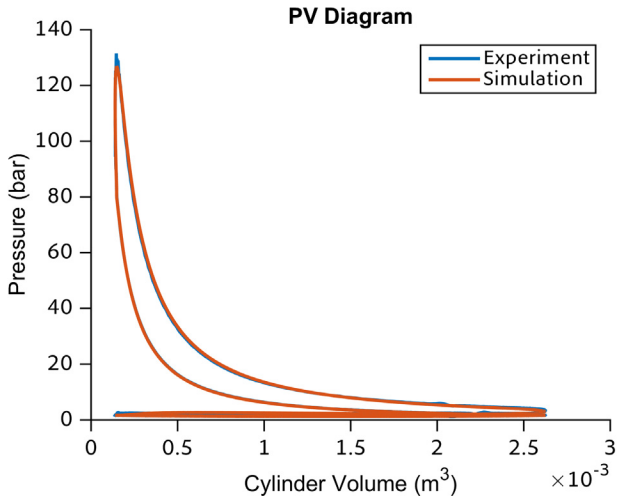

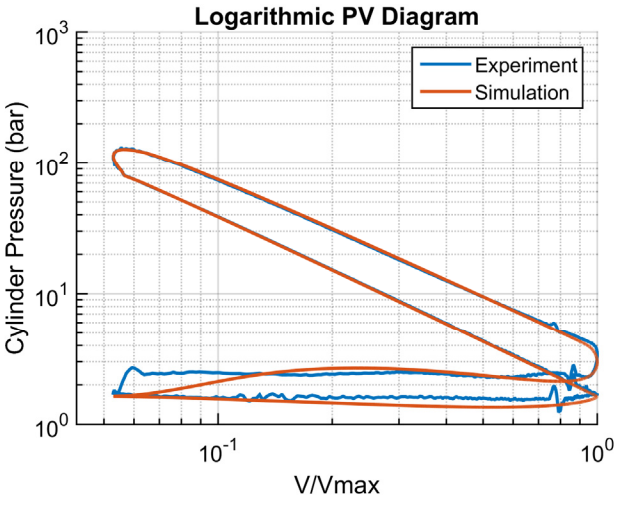

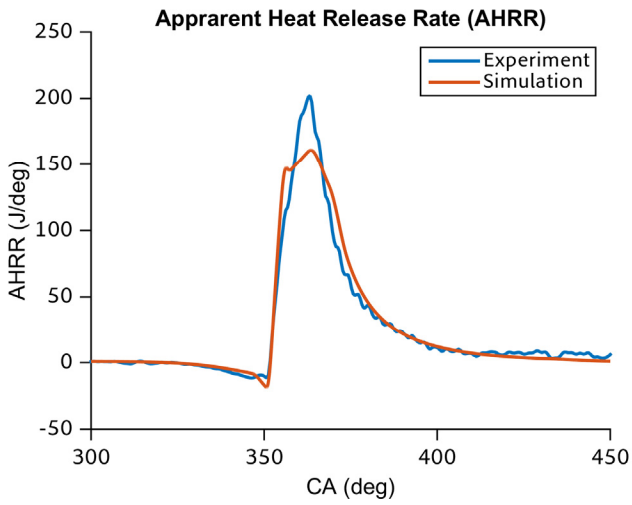

Case 12: 1830 rpm, 25% load

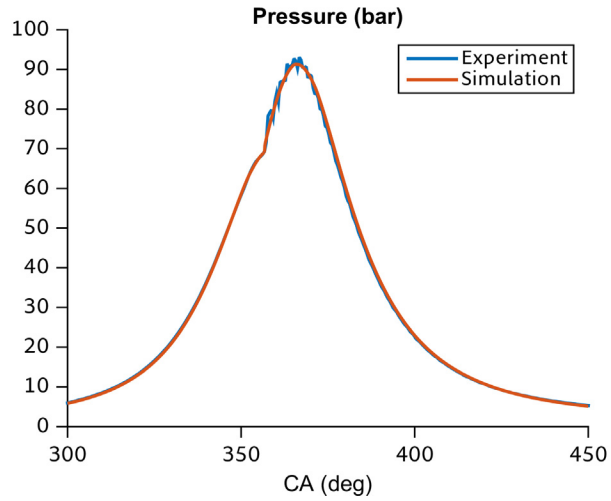

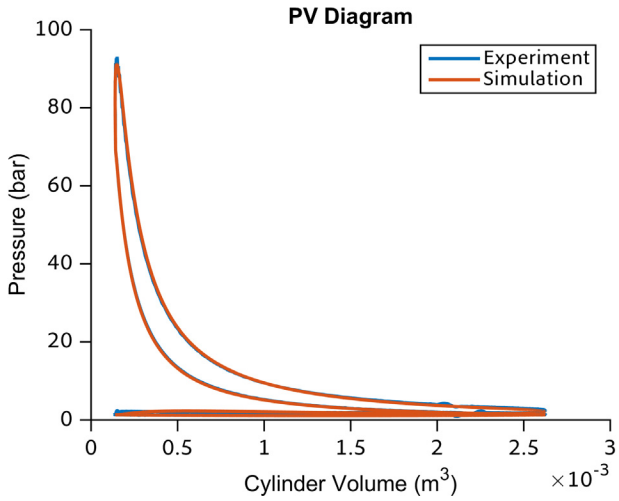

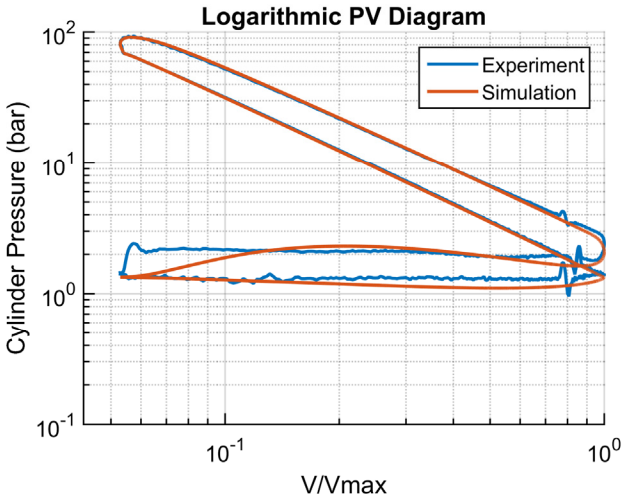

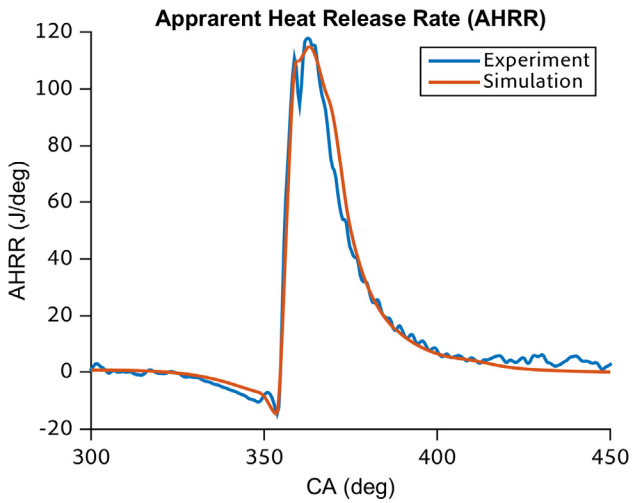

References

Agnew, W. G. (1985) 'Room at the piston top contributions of combustion science to engine design', *Symposium (International) on Combustion*, 20(1), pp. 1–17. doi: 10.1016/S0082-0784(85)80482-3.

Annand, W. J. D. (1963) 'Heat transfer in the cylinders of reciprocating internal combustion engines', *ARCHIVE: Proceedings of the Institution of Mechanical Engineers 1847-1982 (vols 1-196)*, 177(1963), pp. 973–996. doi: 10.1243/PIME_PROC_1963_177_069_02.

Antx (2012) *Messenger*. Available at: http://www.antx.com/Products/Messenger/index.htm (Accessed: 1 June 2012).

Asay, R. J. (2003) *A Five-Zone Model for Direct Injection Diesel Combustion*. Master's Thesis. Brigham Young University.

Assanis, D. N., Ekchian, J. E., Frank, R. M. and Heywood, J. B. (1985) *A Computer Simulation of the Turbocharged Turbocompounded Diesel Engine System: A Description of the Thermodynamic and Heat Transfer Models*. NASA CR-174971.

Assanis, D. N., Filipi, Z. S., Fiveland, S. B. and Syrimis, M. (2003) 'A Predictive Ignition Delay Correlation Under Steady-State and Transient Operation of a Direct Injection Diesel Engine', *Journal of Engineering for Gas Turbines and Power*, 125(2), p. 450. doi: 10.1115/1.1563238.

Ates, M. (2009) *Fuel Economy Modeling of Light-Duty and Heavy-Duty Vehicles, and Coastdown Study*. Master's Thesis. The University of Texas at Austin.

Ates, M. and Matthews, R. D. (2012) *Coastdown Coefficient Analysis of Heavy-Duty Vehicles and Application to the Examination of the Effects of Grade and Other Parameters on Fuel Consumption*. SAE Technical Paper 2012-01-2051. doi: 10.4271/2012-01-2051.

Austen, A. E. W. and Lyn, W. T. (1962) *Some Steps Toward Calculating Diesel Engine Behavior*, *SAE Technical Paper 620550*. SAE Technical Paper 620550. doi: 10.4271/620550.

Barba, C., Burkhardt, C., Boulouchos, K. and Bargende, M. (2000) *A Phenomenological Combustion Model for Heat Release Rate Prediction in High-Speed DI Diesel Engines with Common Rail Injection*. SAE Technical Paper 2000-01-2933. doi: 10.4271/2000-01-2933.

Boulouchos, K. and Eberle, M. K. (1991) *Engine Thermodynamics Today - Challenges and Possible Solutions*. MTZ 52, No. 11.

Brunt, M. F. J. and Pond, C. R. (1997) *Evaluation of techniques for absolute cylinder pressure correction*. SAE Technical Paper 970036. doi: 10.4271/970036.

Chen, S. K. and Flynn, P. F. (1965) *Development of a Single Cylinder Compression Ignition Research Engine*. SAE Technical Paper 650733. doi: 10.4271/650733.

Chiu, W. S., Shahed, S. M. and Lyn, W. T. (1976) *A Transient Spray Mixing Model for Diesel Combustion*. SAE Technical Paper 760128. doi: 10.4271/760128.

Dec, J. E. (1997) *A Conceptual Model of DI Diesel Combustion Based on Laser-Sheet Imaging*. SAE Technical Paper 970873. doi: 10.4271/970873.

DG Technologies (2012) *DPA 4 Plus*. Available at: http://www.dgtech.com/product/dpa4plus/flier/dpa4plus_Flyer_2012.pdf (Accessed: 1 June 2012).

EPA (2012) *Annual Certification Test Results & Data*, *U.S. Environmental Protection Agency*. Available at: http://www.epa.gov/otaq/crttst.htm (Accessed: 15 December 2013).

Espey, C. and Dec, J. E. (1995) *The Effect of TDC Temperature and Density on the Liquid-Phase Fuel Penetration in a D. I. Diesel Engine*. SAE Technical Paper 952456. doi: 10.4271/952456.

Espey, C., Dec, J. E., Litzinger, T. A. and Santavicca, D. A. (1997) 'Planar laser rayleigh scattering for quantitative vapor-fuel imaging in a diesel jet', *Combustion and Flame*, 109(1-2), pp. 65–86. doi: 10.1016/S0010-2180(96)00126-5.

Faeth, G. G. M. (1977) 'Current status of droplet and liquid combustion', *Progress in Energy and Combustion Science*, 3(4), pp. 191–224. doi: 10.1016/0360-1285(77)90012-0.

Federal Register (2011) 'Greenhouse Gas Emissions Standards and Fuel Efficiency Standards for Medium- and Heavy-Duty Engines and Vehicles; Final Rule', *Environmental Protection Agency*, 76(179).

Federal Register (2014) 'Control of Air Pollution From Motor Vehicles: Tier 3 Motor Vehicle Emission and Fuel Standars; Final Rule', *Environmental Protection Agency*, 79(81), pp. 1–474.

Flynn, P. F., Durrett, R. P., Hunter, G. L., zur Loye, A. O., Akinyemi, O. C., Dec, J. E. and Westbrook, C. K. (1999) *Diesel Combustion: An Integrated View Combining Laser Diagnostics, Chemical Kinetics, And Empirical Validation*. SAE Technical Paper 1999-01-0509. doi: 10.4271/1999-01-0509.

Goodwin, D., Malaya, N., Moffat, H. and Speth, R. (2014) 'Cantera: An Object-oriented Software Toolkit for Chemical Kinetics, Thermodynamics, and Transport Processes'.

Grasso, F. and Bracco, F. V. (1983) 'Computed and measured turbulence in axisymmetric reciprocating engines', *AIAA Journal*, 21(4), pp. 601–607. doi: 10.2514/3.8119.

Hackett, J. E., Williams, J. E., Baker, J. B. and Wallis, S. B. (1987) *On the Influence of Ground Movement and Wheel Rotation in Tests on Modern Car Shapes*, *SAE Technical Paper*. SAE Technical Paper 870245. SAE International. doi: 10.4271/870245.

Haenni Scales (2012) *Wheel Load Scale WL 101*. Available at: http://www.haenni-scales.ch/e/produkte/pdf/W1_110_E.pdf (Accessed: 1 June 2012).

Heywood, J. B. (1988) *Internal Combustion Engine Fundamentals*. McGraw-Hill.

Higgins, B., Siebers, D. L. and Aradi, A. (2000) *Diesel-Spray Ignition and Premixed-Burn Behavior*. SAE Technical Paper 2000-01-0940. doi: 10.4271/2000-01-0940.

Hiroyasu, H. and Arai, M. (1990) *Structures of Fuel Sprays in Diesel Engines*. SAE Technical Paper 900475. doi: 10.4271/900475.

Hiroyasu, H., Arai, M. and Tabata, M. (1989) *Empirical Equations for the Sauter Mean Diameter of a Diesel Spray*. SAE Technical Paper 890464. doi: 10.4271/890464.

Hiroyasu, H. and Kadota, T. (1976) *Models for Combustion and Formation of Nitric Oxide and Soot in Direct Injection Diesel Engines*. SAE Technical Paper 760129. doi: 10.4271/760129.

Hohenberg, G. F. (1979) *Advanced Approaches for Heat Transfer Calculations*. SAE Technical Paper 790825. doi: 10.4271/790825.

Honeywell (2012) *Honeywell TE923W Professional Weather Station with Remote Control*. Available at: http://www.honeywellcentral.com/ssi/pdf/honeywell/TE923W.pdf (Accessed: 1 June 2012).

Im, Y. and Huh, K. (2000) 'Phenomenological combustion modeling of a direct injection diesel engine with in-cylinder flow effects', *KSME International Journal*, 14(5), pp. 569–581. doi: 10.1007/BF03185660.

International Programme on Chemical Safety (1996) *Environmental Health Criteria 171: Diesel Fuel and Exhaust Emissions*, *World Health Organization*. Geneva.

Jung, D. and Assanis, D. N. (2001) *Multi-Zone DI Diesel Spray Combustion Model for Cycle Simulation Studies of Engine Performance and Emissions*. SAE Technical Paper 2001-01-1246. doi: 10.4271/2001-01-1246.

Kelly, K. J. (2002) 'Modeling Tools for Predicting the Impact of Rolling Resistance on Energy Usage and Fuel Efficiency for Realistic Driving Cycles', in *International Tire Exhibition and Conference*, pp. 1–8.

Krieger, R. B. and Borman, G. L. (1966) *The computation of apparent heat release for internal combustion engines*. ASME Paper 66-WA/DPG4. ASME.

Kuo, K. K. (2005) *Principles of Combustion*. 2nd edn. Hoboken, New Jersey: John Wiley & Sons, Inc.

Lee, K., Yoon, M. and Sunwoo, M. (2008) 'A study on pegging methods for noisy cylinder pressure signal', *Control Engineering Practice*, 16(8), pp. 922–929. doi: 10.1016/j.conengprac.2007.10.007.

Livengood, J. C. and Wu, P. C. (1955) 'Correlation of autoignition phenomena in internal combustion engines and rapid compression machines', *Symposium (International) on Combustion*, 5(1), pp. 347–356. doi: 10.1016/S0082-0784(55)80047-1.

Maiboom, A., Tauzia, X., Shah, S. R. and Hétet, J.-F. (2009) 'New Phenomenological Six-Zone Combustion Model for Direct-Injection Diesel Engines', *Energy & Fuels*, 23(2), pp. 690–703. doi: 10.1021/ef800735d.

MathWorks (2012) *Solve nonlinear curve-fitting (data-fitting) problems in least-squares sense: lsqcurvefit*. Available at: http://www.mathworks.com/help/toolbox/optim/ug/lsqcurvefit.html (Accessed: 1 June 2012).

MathWorks (2016a) *Curve Fitting Toolbox Documentation: smooth*. Available at: http://www.mathworks.com/help/curvefit/smooth.html (Accessed: 31 January 2016).

MathWorks (2016b) *MathWorks: Company Overview*, *MathWorks*. Available at: http://www.mathworks.com/company/factsheet.pdf (Accessed: 12 February 2016).

Matthews, R. D. (2007) *Internal Combustion Engines and Automotive Engineering*. 2007th edn. Draft copy of a textbook to be published by SAE International Spring 2012 - ME374C/ME 382R Course. Austin.

Matthews, R. D., Seedah, D., Ates, M., Kim, K. J., Anderson, G., Vaughn, J., Dardalis, D., Hao, L. and Harrison, R. (2011) *Estimating Texas Motor Vehicle Operating Costs: Final Report*, *The University of Texas at Austin*. Austin.

Miles, P. C. (2000) *The Influence of Swirl on HSDI Diesel Combustion at Moderate Speed and Load*. SAE Technical Paper 2000-01-1829. doi: 10.4271/2000-01-1829.

Moon, S., Matsumoto, Y., Nishida, K. and Gao, J. (2010) 'Gas entrainment characteristics of diesel spray injected by a group-hole nozzle', *Fuel*. Elsevier Ltd, 89(11), pp. 3287–3299. doi: 10.1016/j.fuel.2010.05.011.

Naber, J. D. and Siebers, D. L. (1996) *Effects of Gas Density and Vaporization on Penetration and Dispersion of Diesel Sprays*. SAE Technical Paper 960034. doi: 10.4271/960034.

Nam, E. K. and Giannelli, R. (2005) *Fuel Consumption Modeling of Conventional and Advanced Technology Vehicles in the Physical Emission Rate Estimator (PERE)*, *Environmental Protection Agency*. EPA420-P-05-001.

Namazian, M. and Heywood, J. B. (1982) *Flow in the Piston-Cylinder-Ring Crevices of a Spark-Ignition Engine: Effect on Hydrocarbon Emissions, Efficiency and Power*. SAE Technical Paper 820088. doi: 10.4271/820088.

Nishida, K. and Hiroyasu, H. (1989) *Simplified Three-Dimensional Modeling of Mixture Formation and Combustion in a D.I. Diesel Engine*. SAE Technical Paper 890269. doi: 10.4271/890269.

Patel, A., Kong, S. and Reitz, R. D. (2004) *Development and Validation of a Reduced Reaction Mechanism for HCCI Engine Simulations*. SAE Technical Paper 2004-01-0558. doi: 10.4271/2004-01-0558.

Perini, F. and Mattarelli, E. (2011) 'Development and calibration of an enhanced quasi-dimensional combustion model for HSDI diesel engines', *International Journal of Engine Research*, 12(4), pp. 311–335. doi: 10.1177/1468087411401285.

Petrushov, V. A. (1997) *Coast Down Method in Time-Distance Variables*. SAE Technical Paper 970408. doi: 10.4271/970408.

Petrushov, V. A. (1998) 'Improvement in vehicle aerodynamic drag and rolling resistance determination from coast-down tests', *Proceedings of the Institution of Mechanical Engineers, Part D: Journal of Automobile Engineering*, 212, pp. 369–380. doi: 10.1243/0954407981526037.

Petrushov, V. A. (2009) *Coast Down Method in Time and Distance Variables for Tire Rolling Resistance Determination*, *SAE Technical Paper*. SAE Technical Paper 2009-01-0072. doi: 10.4271/2009-01-0072.

Pickett, L. M., Siebers, D. L. and Idicheria, C. A. (2005) *Relationship Between Ignition Processes and the Lift-Off Length of Diesel Fuel Jets*. SAE Technical Paper 2005-01-3843. doi: 10.4271/2005-01-3843.

Powell, N. H. and Sarner, S. F. (1959) *The Use of Element Potentials in Analysis of Chemical Equilibrium*. Report R59/FPD.

Randolph, A. (1990) *Methods of processing cylinder-pressure transducer signals to maximize data accuracy*. SAE Technical Paper 900170. doi: 10.4271/900170.

Roberts, C. E. and Matthews, R. D. (1996) *Development and Application of an Improved Ring Pack Model for Hydrocarbon Emissions Studies*. SAE Technical Paper 961966. doi: 10.4271/961966.

Russell, M. F. and Haworth, R. (1985) *Combustion Noise from High Speed Direct Injection Diesel Engines*. SAE Technical Paper 850973.

SAE (1996) *Road Load Measurement and Dynamometer Simulation Using Coastdown Techniques*. SAE Surface Vehicle Recommended Practice SAE J1263.

SAE (2008a) *Road Load Measurement Using Onboard Anemometry and Coastdown Techniques*. SAE Surface Vehicle Recommended Practice SAE J2263.

SAE (2008b) *Stepwise Coastdown Methodology for Measuring Tire Rolling Resistance*. SAE Recommended Practice SAE J2452.

Setchkin, N. P. (1954) 'Self-Ignition Temperatures of Combustible Liquids', *Journal of Research of the National Bureau of Standards*, 53(1).

Seykens, X. L. J. (2009) *Development and validation of a phenomenological diesel engine combustion model*. PhD Dissertation. Eindhoven University of Technology.

Siebers, D. and Higgins, B. (2001) *Flame Lift-Off on Direct-Injection Diesel Sprays Under Quiescent Conditions*. SAE Technical Paper 2001-01-0530. doi: 10.4271/2001-01-0530.

Siebers, D., Higgins, B. and Pickett, L. (2002) *Flame Lift-Off on Direct-Injection Diesel Fuel Jets: Oxygen Concentration Effects*. SAE Technical Paper 2002-01-0890. doi: 10.4271/2002-01-0890.

Siebers, D. L. (1998) *Liquid-Phase Fuel Penetration in Diesel Sprays*. SAE Technical Paper 980809. doi: 10.4271/980809.

Siebers, D. L. (1999) *Scaling Liquid-Phase Fuel Penetration in Diesel Sprays Based on Mixing-Limited Vaporization*. SAE Technical Paper 1999-01-0528. doi: 10.4271/1999-01-0528.

Siebers, D. L. (2009) 'Recent Developments on Diesel Fuel Jets Under Quiescent Conditions', in Arcoumanis, C. and Kamimoto, T. (eds) *Flow and Combustion in Reciprocating Engines*. Berlin, Heidelberg: Springer Berlin Heidelberg, pp. 257–316. doi: 10.1007/978-3-540-68901-0.

Smith, W. R. and Missen, R. W. (1982) *Chemical reaction equilibrium analysis: Theory and algorithms*. New York: Wiley.

Soroka, W. and Chien, C. (1969) *Automotive Piston-Engine Noise and Its Reduction-a Literature Survey, SAE International*. SAE Technical Paper 690452. doi: 10.4271/690452.

USGlobalSat (2012) *DG-100 GPS Data Logger*. Available at: http://usglobalsat.com/store/download/25/dg100_ds_ug.pdf (Accessed: 1 June 2012).

Wang, H., Deneys Reitz, R., Yao, M., Yang, B., Jiao, Q. and Qiu, L. (2013) 'Development of an n-heptane-n-butanol-PAH mechanism and its application for combustion and soot prediction', *Combustion and Flame*. The Combustion Institute., 160(3), pp. 504–519. doi: 10.1016/j.combustflame.2012.11.017.

Watson, N. and Janota, M. S. (1982) *Turbocharging the Internal Combustion Engine*. John Wiley & Sons.

Watson, N., Pilley, A. D. and Marzouk, M. (1980) *A Combustion Correlation for Diesel Engine Simulation*. SAE Technical Paper 800029. doi: 10.4271/800029.

Welter, D., Ates, M., Loftus-Otway, L., Matthews, R. D. and Harrison, R. (2009)

Estimating Texas Motor Vehicle Operating Costs, *The University of Texas at Austin*. Austin.

Westbrook, C. K. and Dryer, F. L. (1984) 'Chemical kinetic modeling of hydrocarbon combustion', *Progress in Energy and Combustion Science*, pp. 1–57. doi: 10.1016/0360-1285(84)90118-7.

Whitehouse, N. D. and Sareen, B. K. (1974) *Prediction of Heat Release in a Quiescent Chamber Diesel Engine Allowing for Fuel/Air Mixing*. SAE Technical Paper 740084. doi: 10.4271/740084.

Wikipedia (2012) *Automobile Manufacturers Association*. Available at: http://en.wikipedia.org/wiki/Automobile_Manufacturers_Association (Accessed: 1 June 2012).

Woschni, G. (1967) *A Universally Applicable Equation for the Instantaneous Heat Transfer Coefficient in the Internal Combustion Engine*. SAE Technical Paper 670931. doi: 10.4271/670931.

Xue, X. and Caton, J. A. (2012) 'Detailed multi-zone thermodynamic simulation for direct-injection diesel engine combustion', *International Journal of Engine Research*, 13(4), pp. 340–356. doi: 10.1177/1468087411435206.

Yasin, T. P. (1978) *The Analytical Basis of Automobile Coastdown Testing*. SAE Technical Paper 780334. doi: 10.4271/780334.

Zhou, P., Zhou, S. and Clelland, D. (2006) 'A modified quasi-dimensional multi-zone combustion model for direct injection diesels', *International Journal of Engine Research*, 7(4), pp. 335–345. doi: 10.1243/14680874JER02604.